UNIVERSITY OF CALIFORNIA, SAN DIEGO

Search for Non-Standard Model Signatures in the WZ/ZZ Final State at CDF Run II

A dissertation submitted in partial satisfaction of the
requirements for the degree
Doctor of Philosophy

in

Physics

by

Matthew Norman

Committee in charge:

Professor Frank Würthwein, Chair
Professor Francine Berman
Professor James Branson
Professor Kenneth Intriligator
Professor Keith Marzullo

2009

The dissertation of Matthew Norman is approved, and it is acceptable in quality and form for publication on microfilm:

_____

_____

_____

_____

_____

Chair

University of California, San Diego

2009

EPIGRAPH

We collide Leprechaun and Leprechaun
to make Unicorn.
—Rami Vanguri, UCSD

What's all this then?
—Unattributed to protect the guilty

TABLE OF CONTENTS

LIST OF FIGURES

LIST OF TABLES

ACKNOWLEDGEMENTS

In the completion of this thesis I must acknowledge the assistance of the CDF Detector collaboration, as well as that of the Fermi National Accelerator Laboratory, and the funding of the Department of Energy. The material herein is being considered for publication on behalf of the CDF Run II collaboration.

I will also thank Frank for not firing me when he probably should have, for reasons that I still don't understand, despite frequent and comprehensive evidence that I do not, in fact, do work. I will thank Mark, Elliot, and Shih-Chieh for having done all the hard work before I even arrived at the experiment, and will hope that they all go on to actual careers in the field. Rami needs no thanks, he is clearly going far with or without them, but I'll give them out anyway.

On a more personal level, I should also thank certain unnamed parties for pointing out early on that working for CMS as a graduate student was a stupid idea, and thus saving me several years of unnecessary complication. There are a number of others to whom personal thanks is required, even though it has no place in a professional document, friends and family alike. And a number of other people who will never read this thesis, or in all probability ever know my name, for reminding me that being a graduate student was only my day job, and that in the end, what happened there did not really matter.

VITA

2003	B. S. in Applied Physics , California Institute of Technology
2005	M. S. in Physics, University of California, San Diego
2009	Ph. D. in Physics, University of California, San Diego

ABSTRACT OF THE DISSERTATION

Search for Non-Standard Model Signatures in the WZ/ZZ Final State at CDF Run II

by

Matthew Norman
Doctor of Philosophy in Physics

University of California San Diego, 2009

Professor Frank Würthwein, Chair

This thesis discusses a search for non-Standard Model physics in heavy diboson production in the dilepton-dijet final state, using 1.9 fb^{-1} of data from the CDF Run II detector. New limits are set on the anomalous coupling parameters for ZZ and WZ production based on limiting the production cross-section at high $\hat{s}$. Additionally limits are set on the direct decay of new physics to ZZ and WZ diboson pairs. The nature and parameters of the CDF Run II detector are discussed, as are the influences that it has on the methods of our analysis.

Chapter 1

Preface

There has been spirited philosophical debate for centuries about which question is the primary question of human existence, if indeed there is such a thing. There have spirited arguments for "Who?", as in "Who are we?", and "Why?", as in "Why are we here?". I would like to submit another possibility, "What?", specifically "What happens if I do this?"

For many centuries, science, and the entire frontier of human knowledge, was defined by that question. The answer was essentially binary. Either it killed you (1), or you survived (0). Hence an early scientist's experimental results could be seen as a chain of binary numbers, inevitably looking something like this: 0000001.

This method of doing science was somewhat wasteful, especially since, while zeroes were easy to pass along, the act of a one tended to remove certain methods of passing on direct information. This eventually changed with the invention of the early prototype to the modern graduate student. With the assistance of a proto-grad student, the early scientist could begin recording larger amounts of data of the form 000100000010001, where the ones simply meant that he had to go and get another grad student.

Eventually, science got around to using the number two. Not only did this allow for the investigator to get two graduate students, increasing the research work even when the green berry did turn out to be fatal, but it allowed for the recording of a new result; "Result inconclusive. Further experimentation required." Originally this was probably related to results like "Subject died after eating the red berry.

Death was caused by panther leaping out of the jungle and biting off his head. Uncertain as to whether this constitutes a 1 or a 0."

If ancient science was a series of ones and zeroes, then modern particle physics has only one number, the two. A type two result now means broadly "We measured something. Our measurement is better then those measurements that have come before, and will probably be worse then those measurements that come after. We have confirmed previous results, but cannot either confirm an entirely new hypothesis or discard an old one". Confirming something, without the possibility of doubt, or disproving something is very rare, and ones and zeroes almost never appear. We live in an age where the progress of science cannot be seen as a continual story of rousing successes and dismal failures, but as a slow trudge toward something that we hope will be extraordinary.

This thesis is a complete type two result. It should not make you feel exhulted that we have broken through some barrier and glimpsed an entirely new piece of physics. Nor should it make you despair at the folly of particle physics. If after reading this thesis you are overcome by a sense of despair, futility, and a sudden desire to run for public office, you should seek help from a qualified mental health care professional. This thesis marks another step on the road from here to there, toward an inevitable one or zero at the end of the road. It is science of perhaps the least glamorous, but most necessary kind.

No graduate students were eaten by panthers during the creation of this thesis.

Chapter 2

A Brief History of Particle Physics

2.1 Introduction

Everything in the universe is made up of particles.

This is either a very profound, or a very unprofound statement. I will leave debates to that end as a matter of interest for philosophers, but profundity is not a good measure of the truth. And this is a very true statement. Everything is made up of particles, and thus the study of particles is the study of everything.

Particle physics is one of the main cornerstones of modern physics, at the small end of a scale that runs from particle physics to Cosmology; the study of the very small, tiny building blocks that make up normal matter. It describes the universe, not in broad terms, but in precise mathematical equations in a world where the chaos inherent in the system is enough to break down any attempt to predict all but the most basic of basic behavior.

It is traditional to open one's discussion of the Standard Model of Particle Physics with a clumsy, inept, and inexact analogy. And who am I to flaunt tradition?

2.2 An Analogy

Imagine the city of Chicago. Let us sweep it clean of the people, the street people, the young party-goers, the nine-to-fivers, the restaurant workers, and the busy businessmen in their dark coats hurrying back and forth around the streets. Let us brush the trash from the sidewalks, the cars from the streets, and the birds from the sky and dump them all in Lake Michigan to annoy the fish. Now we have a city that is totally empty, resembling an architectural model more than a living, breathing city.

What is the city of Chicago made out of? From above, the city is made of buildings. If you can imagine the city to be anything (and by that I do mean absolutely anything), then the buildings are the molecules. Many buildings are unique, like the downtown skyscrapers, where others, like the tract housing that dominates much of Chicago's suburbs, are basically identical.

If you take a particular building and look at it, you will find that the building itself is made out of rooms. Some buildings have thousands, some only have a few. Some only have one. There are a great many types of rooms, but most of them act the same. They tend to have four sides, four corners at right angles, and a door. A cubicle in the Hancock Tower may look different from the observation deck of the Sears Tower, but in terms of shape they can be very close. And an office in the Sears Tower probably looks much the same as any other office anywhere. These are our atoms, the building blocks of chemistry. Like rooms, atoms generally behave in very similar ways, but like the difference between the master bedroom and the boiler room, small changes in their behavior leads to radically different functionality.

Every room, however, seems composed of three components. There is a floor, a ceiling, and walls. From a functional perspective, these three components are almost always identical. A ceiling keeps the rain off your head (and people above from falling on top of you), a floor is something to stand on, and walls keep you from having to watch your next-door neighbor all day. It is only the arrangement of these three components that makes a room, and ultimately a building, unique.

These would be our sub-atomic particles, the electron, the proton, and the

neutron. All atoms, as we are taught in high school, are made out of these three particles. It is only the number and amount of them that makes one atom any different from another. The number of protons determines the chemical properties of the atom, the number of neutrons determines its stability, and the number of electrons determines its ionic state. If you take Carbon-12, the building block of life, and add two neutrons and two protons, you get Oxygen-16, the fuel that humans run on. It is a very simple, very elegant system.

This is where the casual observer of building plans and exteriors tends to stop, walls, floors, and ceilings. After all, this is all that is visible to the untrained eye when looking at the blueprints. And this is where the casual student of the sciences stops, at electrons, neutrons, and protons, the simplest possible building blocks of matter that contribute to everyday life.

But for both the professional builder and the professional physicist, there is another layer underneath that is the subject of much examination. There are walls made out of glass, or wood, or drywall, floors reinforced by steel girders or wooden studs. Even though, at a distance, everything looks the same, they are in reality very different.

The same applies to subatomic particles. The electrons is what we call a "fundamental" particle: we have not yet been able to break it down into constitutents. Neutrons and protons, which make up well over 99% the mass in an atom, are what we call "composite", which you can probably guess means they are actually composed of smaller particles. Protons and neutrons are composed of fundamental particles we call quarks. There are six known types of quarks, although matter as we most often experience it is only made up of two, the up and down quarks. Protons consist of two up quarks and a down quark, neutrons of two down quarks and an up quark. These quarks are held together with even more particles, called gluons (a not-very-clever reference to their glue-like properties in keeping the proton together). Electrons are, as far as we know, indivisible, but the atom is held together by other forces that have so far not entered into the equation, photons, which carry the electromagnetic attraction that keeps electrons buzzing around the nucleus, mesons, whose exchange keeps the nucleus itself together, and a dozen

other particles.

In essence, this is breaking down the world into its constituent parts, steel girders, wooden floorboards, drywall, wooden studs, and glass sheets. Given enough of these basic supplies you could build almost any room, almost any building, and even a full-scale replica of the city of Chicago. But you could also build Tokyo, or London, or New York out of the same supplies. Use more wood and less steel and you could build the suburban centers of Naperville, Illinois, or the outskirts of Hong Kong, or anything all the way down to a few houses in Rio.

The subatomic particle "zoo" that makes up what we understand of the universe can also be used in the same way. Arrange particle in one way and you get iron, another and you get oxygen. You can make a pile of gold or a stocking full of coal. But they are all made out of the same set of particles.

2.3 The Analogy Breaks Down

At some point though, any analogy will break down and we have finally reached the point where we must regretfully wave goodbye to the city of Chicago.

There are two rules that I think we must now invoke. One is what I call the rust rule. The other is the one I call the rule of invisibility. Both of these make particle physics a great deal harder to study than the architecture of a single building already built.

2.3.1 The Rust Rule, or, Things Fall Apart

As you may remember from basic chemistry, the heavier an atom is past a certain point (iron), the more likely it is to fall apart. Uranium, which is notorious for decaying in a relatively explosive fashion, is famous for this, unlike its lighter cousins. For different reasons entirely, this same rule holds for subatomic particles. Even worse, due to their nature, many particles tend not to stick around in observable form.

For instance, take the up and down quarks. Out of the six flavors of quarks these are the lightest, and in some ways the most stable. However, nobody has ever

seen one quark in isolation. Due to the laws of Quantum Chromodynamics (QCD, discussed later), quarks can not exist as singular objects. They must either form two quark states (mesons), or three quark states (baryons). Thinking about the universe like it has a pile of up quarks that it assembles into protons is incorrect because up quarks would vanish before you could do anything with them.

Too many of the particles that make up the universe and govern its actions are simply too hard to study in normal matter. No quark remains stable when isolated. The heavier leptons, the muon and the tau, also decay at some point. The particles that govern the weak interaction, the W and Z bosons, decay immediately. The carrier of the strong force, the gluon, fragments into quarks on an even faster time scale.

In the end, we explain sub-atomic physics in terms of the proton, the neutron, and the electron because these are the only particles that are present in normal matter. Nothing else, except for the photon and the nearly invisible neutrinos, hang around to let us take a look at it.

2.3.2 The Rule of Invisibility, or, We Know It's There Because We Can't See It

The other problem has much the same effect. W and Z bosons, for instance, are constantly at work around us. Yet we almost never see them. This is because they exist only for brief instants as they allow two particles to interact with each other.

In the same way that the nail that holds two boards together may be invisible from a certain angle, from our distant perspective we can never see the nail that hold the proton together, or that allows the neutron to decay into the proton. We can only observe that there must be a nail because so far the boards have not fallen apart.

2.3.3 So What Does That Mean?

The universe, as I said before, is made out of particles. A great many particles. However, we can see very few of the fundamental particles of nature. In fact, the only fundamental particles that we can find in the world around us are really the electron and the photon, both of which have been studied in such detail as to make further study a moot point.

In order to study the frontiers of particle physics, we have to find a way to look into the heart of matter, into those particles that do not appear normally in nature. To do that we need to crack open our buildings and take a look at what lies inside. That requires an accelerator.

2.4 The Standard Model

The Standard Model of Particle Physics is the sum total of all of our knowledge about the way the universe works, strung together on a mathematical framework that comes from both theoretical prediction and experimental verification. By itself it consists of the theories that govern the interactions of charged particles (Quantum Electrodynamics, or QED), charged and weak particles (Electroweak theory, unified into one mathematical block), and colored particles such as quarks and gluons (Quantum Chromodynamics, or QCD). It is, perhaps, the most well tested theory in all of physics, with experiment and theory agreeing in QED predictions to a degree of accuracy unprecedented in other fields of science.

Physicists, of course, hate it.

One problem with the Standard Model (SM), is its incompleteness. For instance, it includes neither neutrino oscillation (a relatively recent development) or, much more troubling, gravity.

More troubling philosophically is that, unlike theories like Classical Electromagnetism, which only really has one constant, the Standard Model has required dozens of measurements to fill in its huge charts of physically measured constants. The masses of the quarks, the charges, the CKM matrix parameters, all of these seem to be almost randomly decided. It seems awfully coincidential that there are

three generations of quarks and three generations of leptons, it seems strange that the top quark is so heavy, but the SM offers neither explanation nor excuse. The best it can offer is a half-hearted "That's just the way things are, you know?". It has become rapidly clear that the SM does not only explain nothing, but can explain nothing, and that if the SM is the answer to the mysteries of the unvierse that we obviously don't understand the question.

Nevertheless, all dislike aside, the SM persists because it works spectacularly well. As experiments continue to fill in more and more parameters in the Standard Model to better and better precision, it continues to work just as well as it always did.

A brief tour of the Standard Model is required then in order to understand the universe in which we will be working in.

2.5 Leptons

There are six leptons. Three of them are massive, interacting particles, the electron, the μ, and the τ. All of them are fermions, meaning that they have an intrinsic angular momentum of $\frac{1}{2}$. All of them have singular charge, defined as negative for real particles, and positive for their anti-particles. The other three are neutrinos, one counterpart for every one of the standard leptons, the ν_e, ν_μ, and the ν_τ. Neutrinos have extremely small mass, and no charge. They rarely interact.

Leptons conserve something called lepton number. There is an electron number, a muon number, and a tau number, which is carried both by the particle, its counterpart neutrino, and its antiparticles. An electron has an electron number of +1, a positron has an electron number of -1, a ν_e has an electron number of +1, and so on. Interactions conserve lepton number. Practically this means that if you have an interaction that emits an electron, it either had an electron going in, it emitted a positron as well, or it also created a ν_e. Neutral particles decay into e^+e^-, while charged particles tend to decay into $e^\pm\nu_e$.

Leptons interact in two ways, either electromagnetically, or through the so-called weak force. Under electromagnetism, two particles interact through the

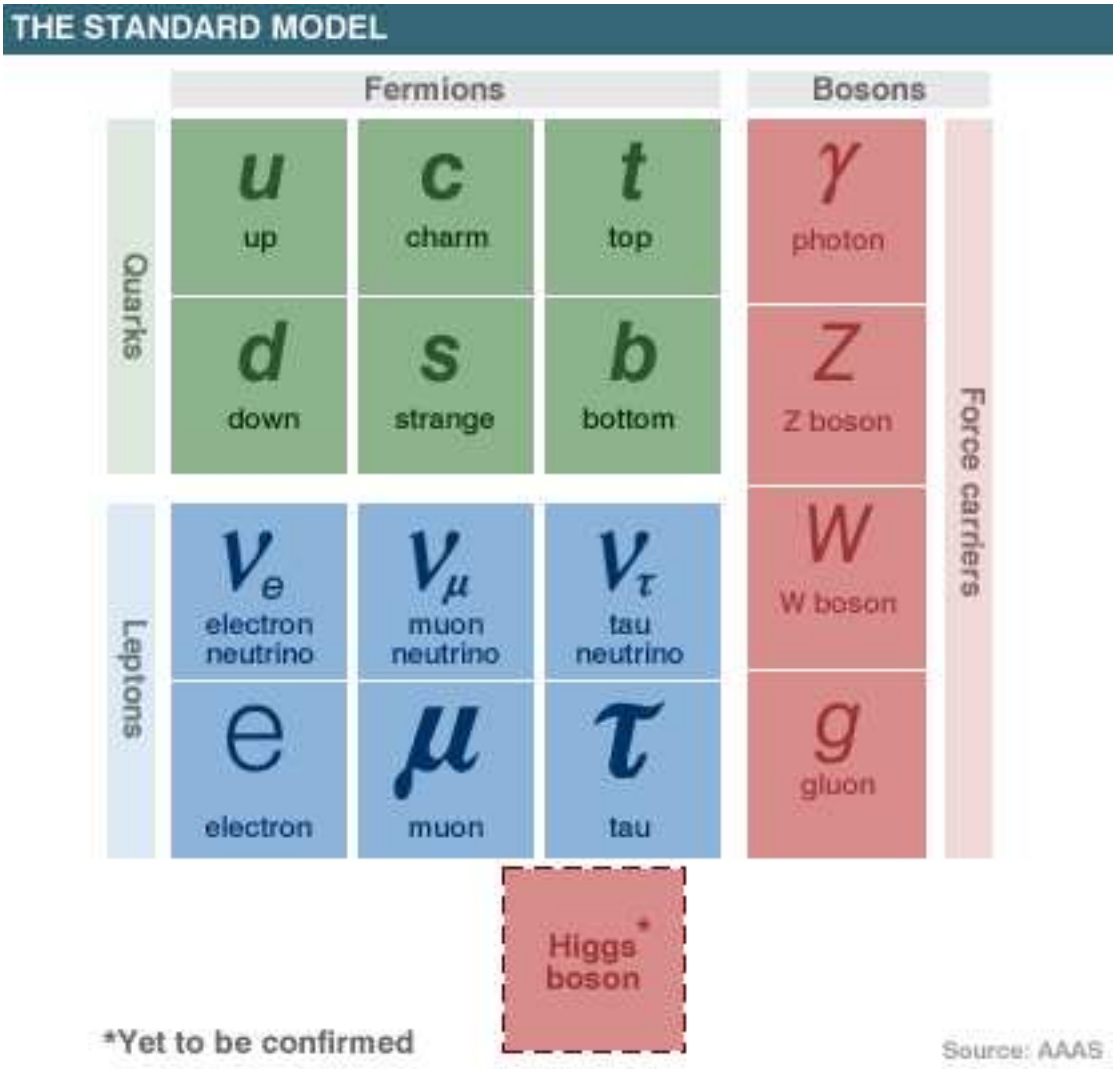

Figure 2.1: The particles of the Standard Model

exchange of a virtual photon, a process we will discuss in more detail in Section 2.7. Under the weak force, they interact through the exchange of the weak bosons, as described in Section 2.7.

2.6 Quarks and QCD

There are also six quarks, classified in three generations. Each generation has an up-type quark (with charge $+\frac{2}{3}$), and a down-type quark (with charge $-\frac{1}{3}$). The first generation consists of the up and down quark. The second generation consists of the strange ($-\frac{1}{3}$) and charm ($+\frac{2}{3}$) quarks, and the third generation of the bottom ($-\frac{1}{3}$) and the massive top ($+\frac{2}{3}$) quark.

As charged objects, quarks can also interact in the same way as charged leptons, by the exchange of a virtual photon. They also interact via the weak force through the weak bosons (Section 2.7). But the key to understanding quarks is through the strong force.

It became apparent early on that simple electromagnetism was not going to be able to explain the behavior of hadronic particles, the large and massive particles, similar to the proton, that seemed to fill an alarmingly large part of the universe. There were simply too many of them and they had too many strange properties to be easily explained.

The eventual theory that crystallized out of observation explained all those properties away by hypothesizing that hadrons were made out of quarks. These small particles had an interesting property, similar to charge, but different. Unlike charge, which tends to appear as only negative and positive values, there was a charge with three different types of values. Only particles with no actual value of this charge could occur.

Being physicists, this charge was named color, as the behavior mimicked that of the behavior of colored light. There are three colors in nature, red, blue, and green. The only particles that can exist in nature are colorless. This is done in one of two ways; you can either combine a quark and an anti-quark (red and anti-red for example), to make a meson, or three quarks (red, blue, and green) to make a

baryon. This explained the existence of both mesons and baryons, and led to the vast zoo of hadronic particles known today.

Mathematically, the color charge could be expressed by using group representations. The gauge group $SU(3)_C$ serves as the mathematical expression of the colored particle interactions, and the eight types of gluons that bind the quarks together are the eight generators of the SU(3) group.

As an experimental consequence, colored objects cannot be seen in nature. This means that there are no such things as "bare" quarks. Every time a decay produces a quark, that quark must immediately bind to other quarks to produce either a meson or a baryon, eventually resulting in a stable particle, or a spray of stable particles known as a "jet".

2.7 Electroweak Physics

Of more importance to this thesis is the development of Electroweak Physics. Where QCD is represented by the $SU(3)_C$ group, it was discovered that you could also describe the interactions of both the Electromagnetic and Weak forces through the $SU(2)_L \otimes U(1)_Y$ group representation, where L stands for left-handed weak isospin, and Y for hypercharge.

The weak force couples left-handed particles and right-handed anti-particles, while the Electromagnetic force governes the interactions dominated by charge. The unification of these forces led to an eventual Nobel Prize. It also allowed for the definition of the three bosons that carry these forces ($W^{\pm}$, Z, γ).

The Electromagnetic interaction is, as already mentioned, carried by the photon, often written as γ. The photon is a massless, spin 1 boson which is stable, and part of normal matter. The three other bosons are very massive objects. Charged weak interactions are carried by the $W^{\pm}$ boson, while neutral interactions are carried by the Z boson.

Both of these particles being very massive, they both decay before they can be seen by any of our instruments. A brief summary of their decay modes is presented in Table 2.1.

Table 2.1: Decay probabilities of the W and Z [10]

Decay Mode	Probability (%)
Z	
e^+e^-	3.36
$\mu^+\mu^-$	3.37
$\tau^+\tau^-$	3.37
$\nu\bar{\nu}$	20.0
hadrons	69.9
W	
$e + \nu$	10.8
$\mu + \nu$	10.8
$\tau + \nu$	10.8
hadrons	67.6

2.8 A Brief Summary

A summary of the basic properties of the Standard Model particles is provided in Table 2.2. This is the comprehensive summary of many years work done at a great many detectors.

2.9 Anomalous Couplings

The current goal of experimental particle physics is to test all the predictions made by the Standard Model and search for discrepencies in order to find hints at new physics that may explain some of the pecularities of the model. Because of the sheer size and scope of the Standard Model there are many different ways in which new physics might first appear. Finding these signatures is the work of particle physicists the world over.

One method is to search for Anomalous Couplings. The SM provides a concise and exact description for how each particle should couple to every other particle. This is what governs the creation of particles in particle colliders. However, the existence of particles and physics not present in the Standard Model can effect these couplings. Even if the piece of new physics is not itself apparent or visible directly, its existence can cause a change in the emission rate for SM particles.

Table 2.2: Particles in the Standard Model and some of their properties [10]

Particle	Mass	Charge	Colored	Stable
Leptons				
Electron	0.511 MeV/c^2	-1	No	Yes
μ	105 MeV/c^2	-1	No	No
τ	1777 MeV/c^2	-1	No	No
ν_e	?	0	No	Yes
ν_{mu}	?	0	No	Yes
ν_τ	?	0	No	Yes
Quarks				
u	1.5-3.3 MeV/c^2	$+\frac{2}{3}$	Yes	No
d	3.5-6.0 MeV/c^2	$-\frac{1}{3}$	Yes	No
s	104 MeV/c^2	$-\frac{1}{3}$	Yes	No
c	1.27 GeV/c^2	$+\frac{2}{3}$	Yes	No
b	4.2 GeV/c^2	$-\frac{1}{3}$	Yes	No
t	171 GeV/c^2	$+\frac{2}{3}$	Yes	No
Bosons				
γ	0	0	No	Yes
gluon	0	0	Yes	No
W^+	80.4 GeV/c^2	+1	No	No
W^-	80.4 GeV/c^2	-1	No	No
Z	91.2 GeV/c^2	0	No	No
Higgs	?	0	No	No

These non-SM couplings are referred to as Anomalous Couplings, and they are searched for by measuring production rates as a function of momenta, energy, and other kinematic variables for particles produced inside the collision. If no direct evidence is found, the amount of particles found, their "differential cross section", is then compared with the one suggested by the Standard Model, and a limit may be placed on the possible cross section of Anomalous Couplings.

Of particular interest, and the topic of this thesis, is the production of W and Z bosons in violation of SM predictions. Because of their high mass, W and Z bosons may couple preferentially to massive particles currently not present in the SM. New signatures and new loop diagrams (mechanisms that involve multiple interactions to get from the initial to the final state) previously unaccounted for in the SM may make their first appearance as a larger-then-expected production of SM particles. We refer to the couplings between combinations of three W and Z bosons as triple gauge couplings, as they involve only the gauge bosons.

We combine this interest in constraining nature to the Standard Model with additional searches that the UCSD group has done in the multi-boson final states, specifically ZZ and WZ. Only in the final years of the Tevatron's run has it become possible to carry out the first measurements of diboson production at hadron colliders. UCSD was instrumental in pushing through the WZ and ZZ measurements at CDF. Now we can begin to search for production beyond the Standard Model, limiting the anomalous production of diboson pairs at $\sqrt{\hat{s}} = 1.96$ TeV.

2.9.1 Neutral Triple Gauge Boson Couplings

The general Lagrangian for neutral triple gauge bosons can be written as seen in equation 2.1 ([12] [13]), where V is the neutral vector boson (Z or γ) involved in the coupling, M_V is the mass of the V boson, M_Z is the mass of the Z boson, and e is the charge of the proton. The Lagrangian has two adjustable parameters, f_4^V and f_5^V, where the 4 indicates that the coupling is forbidden by CP invariance, and the 5 that the coupling is Parity invariant. In the Standard Model, at tree level $f_4^V = f_5^V = 0$, and only t-channel vector diboson production (Fig. 2.2) is allowed, while s-channel production (Fig. 2.3) is prohibited.

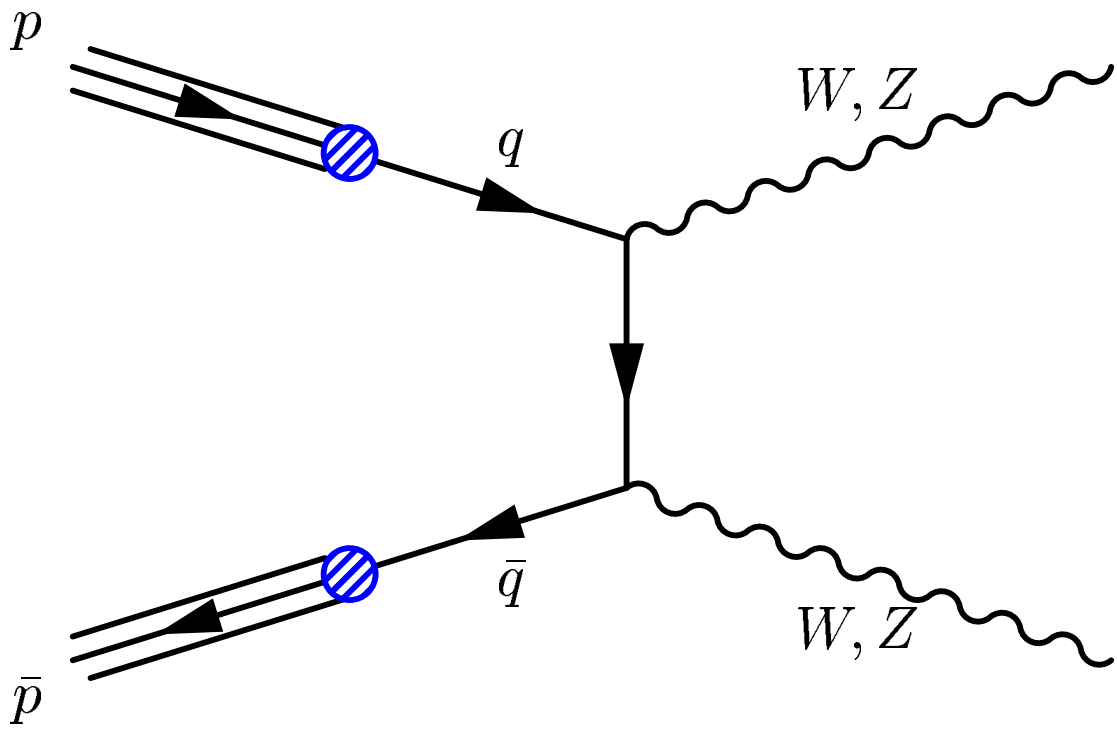

Figure 2.2: Generic t-channel production of diboson final states

$$g_{ZZV}\Gamma^{\alpha\beta\mu}_{ZZV} = e\frac{P^2 - M_V^2}{M_Z^2}[if_4^V(P^\alpha g^{\mu\beta} + P^\beta g^{\mu\alpha}) + if_5^V\epsilon^{\mu\alpha\beta\rho}(q_1 - q_2)_\rho] \tag{2.1}$$

In order to obey S-matrix unitarity, anomalous couplings have to approach their SM values at high energy. All f couplings must contain a momentum-dependent term to insure that this is true, which suppresses the anomalous coupling at high momenta. To insure this, the f parameters are constrained by a form-factor Λ as in equation 2.2:

$$f_i^V(\hat{s}) = \frac{f_{i0}^V}{(1 + \hat{s}/\Lambda_{FF}^2)^3}(i = 4, 5) \tag{2.2}$$

where Λ_{FF} is a cut-off form factor chosen to prevent infinite divergence. Choosing a value of Λ_{FF} is an important part of every analysis.

There are two neutral vector bosons we consider for the neutral gauge couplings, the Z (ZZZ) and the γ (ZZγ). Both couplings were measured at LEP II to high

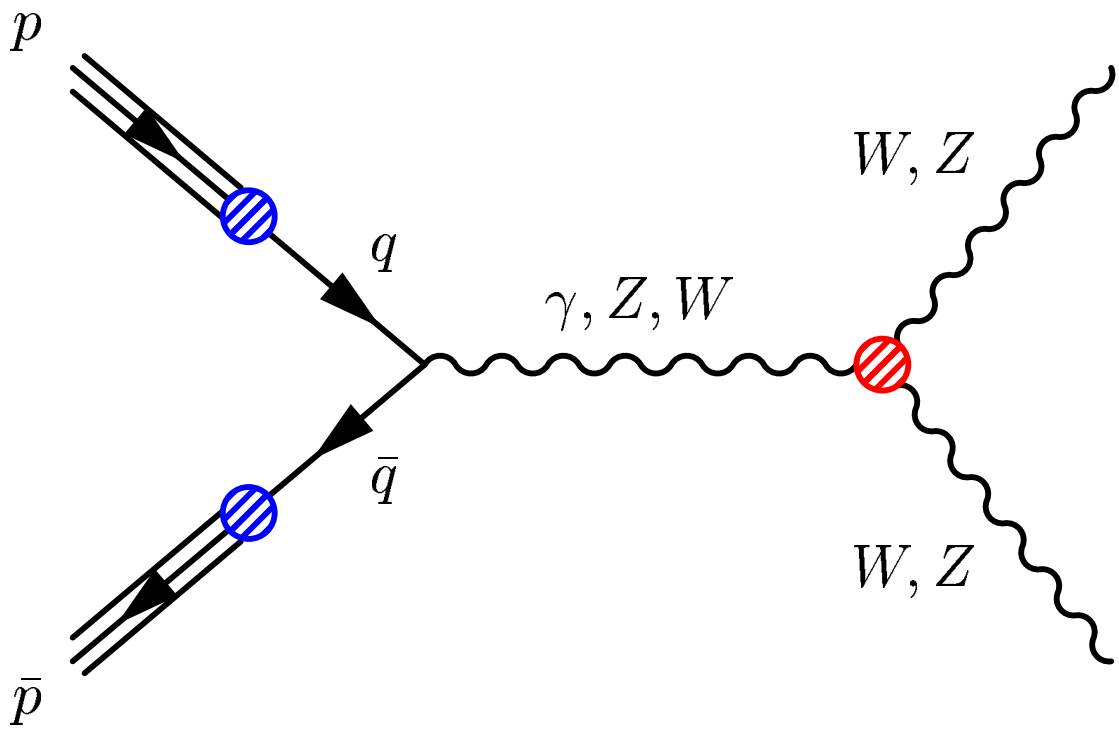

Figure 2.3: Generic s-channel production of diboson final states

Table 2.3: Cross section at leading order for different values of f_4^Z.

f_4^Z	LO Cross-Section (pb)
-0.3	2.88
-0.2	1.78
-0.1	1.12
0.1	1.12
0.2	1.78
0.3	2.88

Table 2.4: Cross section at leading order for different values of f_5^Z.

f_5^Z	LO Cross-Section (pb)
-0.3	2.49
-0.2	1.59
-0.1	1.06
0.1	1.10
0.2	1.68
0.3	2.62

accuracy [19], and have since been measured at D0 [5] in the four lepton channel. This analysis will confirm those values and improve upon them by a factor of approximately three. The cross-sections for ZZ aTGC production for a selection of aTGC values is presented in Tables 2.3, 2.4, 2.5, 2.6.

2.9.2 Charged Triple Gauge Boson Couplings

The charged gauge boson couplings have previously been measured indirectly in LEP II, and directly at both CDF [24] and D0 [4]. The CDF and D0 measurements were done in the trilepton neutrino decay channel for the WZ, and the CDF analysis

Table 2.5: Cross section at leading order for different values of f_4^γ.

f_4^γ	LO Cross-Section (pb)
-0.2	1.74
-0.1	1.11
0.1	1.11
0.2	1.74

Table 2.6: Cross section at leading order for different values of f_5^γ.

f_5^γ	LO Cross-Section (pb)
-0.3	2.43
-0.2	1.57
-0.1	1.06
0.1	1.09
0.2	1.64
0.3	2.54

was done by the UCSD group.

The most general Lagrangian for the charged triple gauge coupling can be expressed as:

$$\begin{aligned}
\frac{1}{ig_{WWV}}\mathcal{L}_{eff}^{WWV} &= g_1^V(W_{\mu\nu}^- W^{+\nu} - W_{\mu\nu}^+ W^{-\nu}) \\
&+ \kappa_V W_\mu^+ W_\nu^- V^{\mu\nu} \\
&+ \frac{\lambda_V}{M_W^2} V^{\mu\nu} W_\nu^{+\rho} W_{\rho\mu}^- \\
&+ ig_5^V \epsilon_{\mu\nu\rho\sigma}((\delta^\rho W^{-\mu})W^{+\mu} - W^{-\mu}(\delta^\rho W^{+\nu}))V^\sigma \\
&+ ig_4^V W_\nu^+ W_\mu^- (\delta^\mu V^\nu + \delta^\nu V^\mu) \\
&- \frac{\bar{\kappa}_V}{2} W_\mu^- + W_\nu^+ \epsilon^{\mu\nu\rho\sigma} V_{\rho\sigma} \\
&- \frac{\lambda_V}{2M_W^2} W_{\rho\mu}^- W_\nu^{+\mu} \epsilon^{\nu\rho\alpha\beta} V_{\alpha\beta}
\end{aligned} \tag{2.3}$$

Here, $g_{WW\gamma} = \mathrm{e}$ and $g_{WWZ} = \mathrm{e}\cot(\theta_W)$, and we use the reduced field strengths $W^{\mu\nu} = \delta^\mu W^\nu + \delta^\nu W^\mu$ and $V^{\mu\nu} = \delta^\mu V^\nu \delta^\nu V^\mu$ are used to simplify the equations. For proper massless photons, $g_1^\gamma = 1$ and $g_5^\gamma = 0$ to preserve $\mathrm{U}(1)_Q$ gauge invariance.

At tree level in the Standard Model, the parameters of this equation are simplified. We take $g_1^\gamma = g_1^Z = \kappa_\gamma = \kappa_Z = 1$, and the λ coupling is set to 0. Under the Standard Model, we produce diboson final states in both the t- and s- channels (Fig. 2.2 and 2.3). To vary our limits from the Stanard Model, we adopt the following conventions:

$$\Delta g^V \equiv (g^V - 1), \Delta\kappa_V \equiv (\kappa_V - 1) \tag{2.4}$$

aTGC limits are typically presented with three values, Δg^V, $\Delta \kappa^V$, and λ_V. In the case of this thesis, we will be measuring the couplings for the Z boson.

As in the neutral triple gauge couplings, a form-factor cut-off Λ is applied in order to prevent non-physical unitarity violation. The exact form for the Λ value in charged aTGC is:

$$f_i^V(\hat{s}) = \frac{f_{i0}^V}{(1+\hat{s}/\Lambda_{FF}^2)^2}(i = \Delta\kappa, \Delta g, \lambda) \tag{2.5}$$

Chapter 3

Accelerator

3.1 Overview

There are two general classes of particle colliders. One is the lepton collider, which collides electrons and positrons together in order to create particles by electroweak interactions. The second is the hadron colliders, which runs on the simplest type of hadrons available, protons. The Tevatron is an example of a hadron collider, colliding protons with anti-protons, in contrast to the Large Hadron Collider, which will collide protons with protons.

The primary advantage of a lepton collider is that the background involved in each collision is very low. Electrons are point particles, and the collision of an electron with a positron produces only one or two particles. Protons, on the other hand, are not simple. They consist of three "valence" quarks, bound together by a sea of virtual quarks and gluons, all of which will be released when the proton is collided with sufficient force. As a result, it is not uncommon for a proton anti-proton collision to create dozens of byproduct particles, making it harder to find truly interesting events.

However, there are advantages to using a hadron collider. Because of its very precise design, where two leptons are accelerated together and then collided, the lepton collider has a very specific center-of-mass energy. This is excellent for when you know the precise properties of what you are trying to create, but is only capable of examining one center-of-mass energy at a time. A hadron collider, on the other

hand, can simultaneously examine multiple energy scales at once.

The Tevatron was designed to accomplish several goals in particle physics that were considered particularly important.

- Discover and characterize the properties of the then unseen top quark.
- Constrain the elements of the CKM matrix with mesurements of B hadron decays.
- Search for new physics beyond the Standard Model.
- Test our knowledge of perturbative QCD at Next-to-Leading-Order.
- Perform precision electroweak measurements.
- Search for the Higgs Boson.

The scope of the experiment was such that it suggested the use of a hadron collider, where all searches could all be done simultaneously, because a hadron environment not only produces top quarks, it also creates large quantities of B hadrons, electroweak bosons, and QCD backgrounds at the same time without requiring accelerator tuning.

Since then, the Tevatron was become one of the primary tools for particle physics research in the gap between the canceled SSC and the Large Hadron Collider turn-on, originally scheduled for the mid-2000s.

3.2 Basic Properties

The Tevatron, although sometimes used informally to refer to the entire acceleration complex, really only refers to the circular ring-type accelerator that sits at the Fermi National Accelerator Laboratory facility in Batavia, Illinois, on the outskirts of Chicago. The ring is an underground tunnel, 6.3 km in length, which contains the necessary equipment to accelerate protons and anti-protons up to their final energy. It is the last step in a long chain of accelerators which allow us to perform physics.

The actual chain of acceleration runs as follows:

- Cockcroft-Walton: Ionizes hydrogen gas and begins the acceleration chain.
- Linear Accelerator (Linac): Provides the first boost, and eventually strips the ions of their electrons.
- Booster: A small circular accelerator, the Booster accelerates protons to 8 GeV before passing them to the main injector.
- Main Injector: A secondary ringed accelerator, it boosts protons to 120 GeV, and serves as the repository of both protons and anti-protons before injection into the Tevatron.
- Antiproton Source: The Antiproton source takes 120 GeV protons from the Main Injector and collides them with a nickel target to create antiprotons, which are stored in an accumulator ring prior to being returned to the Main Injector.
- Tevatron: The final ring, the Tevatron now accelerates particles to 1.96 TeV before colliding them in two points occupied by the CDF and D0 detectors.

3.3 Accelerator Properties

The original Tevatron, operated during Run 0 and Run I, reached a center of mass energy of $\sqrt{s} = 1.8$ TeV, and ran from 1985-1995. All the data for this thesis, however, comes from Run II, following the upgrade of the Tevatron collider to $\sqrt{s}$ = 1.96 TeV. CDF began to take Run II data in March of 2001.

As mentioned previously, there are several different components of the accelerator, which act in turn to accelerate both protons and anti-protons to the final velocity.

The Cockcroft-Walton pre-accelerator ionizes the gas from H to H^- ions, which are then passed off to the Linac with an energy of 750 keV. For the next two hundred meters or so, the H^- ions are acclerated by a series of Radio Frequency (RF) cavities. The RF cavities are arranged such that the oscillating electric field of each cavity has the side-effect of not only accelerating the ions, but also of

grouping them into bunches. From here, the bunches pass through carbon foil, which removes the electrons, leaving you with simply protons.

There are four circular or semi-circular components to the Tevatron, and each proton will see at least three of them on its way through the accelerator. The first is the Booster, a small circular accelerator 74.5 meters in diameter, which holds the protons for about 20,000 rotations, while they get boosted from the 400 MeV of the Linac to the final 8 GeV that is required for entrance into the Main Injector.

All protons are injected into the Main Injector, which is the second circular (in this case ovaloid) accelerator in the Tevatron chain. Here protons are accelerated up to 150 GeV. It is from here that 120 GeV protons are skimmed off and destroyed by slamming them into a nickel target, producing antiprotons as well as other particles. The third ring-shaped component, the Accumulator ring, holds these antiprotons until they are again released into the Main Injector.

Inside the Main Injector, bunches of either protons or antiprotons are brought up to 150 GeV before being injected separately into the final stage, the large Tevatron ring. The Tevatron is a circular accelerator with a radius of one kilometer that forms the final stop on the proton's path. Inside the Tevatron, both protons and anti-protons are formed into two separate loops and accelerated, each within the same magnetic field. The opposite charge of protons and anti-protons allows for the use of a single magnetic field to deal with two streams of particles going in opposite directions. During collisions, the two streams of particles are brought together to collide in the middle of the collision halls at points B0 and D0 on the Tevatron ring. The D0 detector is housed, appropriately, at the D0 point, while the CDF detector is housed at B0.

3.4 Antimatter Production

The fundamental constraint on the physics capabilities of the Tevatron is its ability to produce and retain antimatter. Antiprotons are not found in nature, and have to be produced through a messy and very inefficient process, involving the collision of 120 GeV protons on a nickel target. The shock of the impact is sufficient

to produce a mishmash of particles, some of which happen to be antiprotons created by various hadronization reactions.

However, antimatter creation is very difficult, even at these high energies. Even at this tremendous energy, it takes about a million protons to create just 20 antiprotons. As a result, antimatter has to be built up in the antiproton Storage Ring prior to a collision run, resulting in high wait times as the accelerator slowly builds up the store of antiprotons necessary to do a long physics run.

Also as a consequence of the decision to use antimatter, the store of antiprotons often degrades within the ring, leading to a decrease in the power and intensity of the beam over time, eventually leading to the number of remaining antiprotons falling below the threshold required to maintain worthwhile collisions. This is compensated for by frequent production and storage of antimatter.

However, the unique properties of a matter-antimatter collision were seen as outweighing the probable defects. Antimatter, when collided with regular protons, allows for a much higher production cross-section for several key processes, including the W and Z bosons in which we are interested.

3.5 Physics Properties

The functionality of the Tevatron is primarily constrained by our production of anti-matter, as described previously. Despite this constraint, the accelerator does regularly and consistenly deliver the required particles to the required targets.

The collision cross-section, the probability of a collision, between a lone proton and a lone antiproton is fairly low. The accelerator compensates for this by sending groups of protons and antiprotons, referred to as "bunches", around the detector in lieu of single particles. This creates a much higher collision rate (by many orders of magnitude), at a cost of sometimes having two different proton-antiproton collisions in a single bunch crossing.

The Run II upgrade for the Tevatron, which began producing data in July 2001, collides 36 bunches with a time between crossing of 396 nanoseconds, with the possibility of multiple collisions per bunch crossing. Design luminosities were

intended to top off at $2 \times 10^{32} cm^{-2} s^{-1}$. 1/136 ns is the fundamental frequency that the detector operates on - the detector must be capable of processing basic information about an event once every 396 ns, or run the risk of losing events due to data pileup, as events become backlogged.

3.6 Luminosity

The measure of how much an accelerator produces is measured in a quantity called luminosity, which is a function both of how many particle collisions occur each second, and the density of the bunches of particles that collide. Luminosity is defined as:

$$\mathcal{L} = \frac{f N_B N_p N_{\bar{p}}}{2\pi(\sigma_p^2 + \sigma_{\bar{p}}^2)} F(\frac{\sigma_{\updownarrow}}{\beta^*}) \tag{3.1}$$

where f is the revolution frequency, N_B is the number of bunches, $N_{p/\bar{p}}$ are the number of protons or anti-protons in a bunch, and $\sigma_{p/\bar{p}}$ are the RMS sizes of the beams at the interaction point. F is the form factor for corrections to the bunch shape, and depends on the bunch length $\sigma_{\updownarrow}$, and the beta function β^* at the interaction point, which is a measure of the beam width proportional to the x and y extent of the beam in phase space. Luminosity is measured in units of $\mathrm{cm}^{-2}\mathrm{s}^{-1}$.

In an experiment, the amount of data collected tends to be measured in integrated luminosity, which is a basic expression of the number of total collisions produced over a course of time. By integrating luminosity, you can get a quantity that expresses the total number of collisions and, given the cross-section of a particular type of event, the number of events of that type that should appear, on average, in your dataset. For instance, in 1 nb^{-1} of integrated luminosity, you would expect an event with a cross-section of 1 nb to appear once, on average, as explained in the following:

$$Number of Events = \sigma \dot{\mathcal{L}} \tag{3.2}$$

where σ is the cross-section (a measure of the probability) of a single event), and $\mathcal{L}$ is the integrated luminosity in your dataset.

The aTGC portion of this analysis was conducted with 1.9 fb^{-1} of integrated luminosity, representing the sum total of several years data. Luminosity is also measured in terms of peak luminosity, which is the highest luminosity achieved during a particular run, generally achieved the moment particles begin colliding.

At the end of 2006, the Tevatron managed to reach the peak luminosity anticipated in the design goals, 2×10^{32} $cm^{-2}s^{-1}$. This represents the culmination of many years of tinkering with the accelerator in order to iron out problems of building up antimatter stores and dealing with various other problems that crop up in a beginning experiment.

3.7 Collisions and the Parton Model

As in the introductory analogy, protons are the basic building block of matter, but despite their outward similarity, protons are not simple objects inside. A proton is three quarks, held together by a sea of gluons. The three quarks that make up the proton have a total mass on the order of 10 MeV/c^2 if one simply adds, but the mass of the three quarks together is on the order of 938 MeV/c^2. That remaining 900 MeV/c^2 is the energy that accumulates in the proton due to the interaction of the three particles. This is expressed in the sea of gluons that constantly work to keep the three quarks from flying apart.

However, when two protons collide, the force of the collision allows everything hidden inside the quarks to fly out. This includes the three valence quarks, any gluons, and any virtual quarks temporarily created by the gluons, all of which have tremendous energy because of the momentum of the protons. Gluons and quarks inside the proton, however, may have different amounts of momentum at the time of the collision, depending on what was happening inside at that exact moment. Each proton is unique, and so is what was happening inside.

Slowly, we have been able to calculate what are called Parton Density Functions (PDFs). PDFs give the distribution of gluons, virtual quarks (the so-called "sea quarks"), and valence quarks within the proton just after the collision as a function of multiple variables. The PDF distributions show the distribution of these released

particles in both the number of probable particles that result from the collision, and x, the fraction of the proton's total momentum that each particle carries.

The cross-section can be expressed mathematically as a sum over all particles in a two particle collision in terms of x as in Equation 3.3.

$$\sigma_{AB} = \sum_{a,b} \int dx_a dx_b f_{a/A}(x_a, Q^2) f_{b/B}(x_b, Q^2) \hat{\sigma}(ab \to X) \tag{3.3}$$

In this expression, Q^2 is the large momentum scale that characterizes the hard scattering collision, and is much larger then soft scales, such as the QCD scale (approximately $\Lambda_{QCD} = (200 \text{ MeV/c})^2$).

For protons and anti-protons, the majority of the energy is generally carried by the valence particles. Therefore the kind of interactions that occur at the highest energies are $q\bar{q}$ collisions, and CDF is built to measure the result of $q\bar{q}$ high energy collisions, which include both W and Z production in the SM, as well as the production of the WW, WZ, and ZZ diboson channels. Thus the CDF Run II environment is optimized for the kind of analysis that we want to do.

This is outwardly similar to the Large Hadron Collider, which is now approaching turnon at CERN. The major difference between the two colliders is that the collisions at CERN are proton-proton, reflecting differences in physics purpose. Physics at the LHC will be dominated by gluon-gluon collisions, which are independent of whether the colliding particles are matter or anti-matter. As a result, the decision there was made to use proton-proton, which is much easier to produce.

PDFs are assembled from x and Q^2 dependencies gathered from various experiments worldwide. Deep Inelastic Scattering experiments, in which hadrons are bombarded with high energy particles to gain some idea of what lies inside, or precision Drell-Yan measurements in fixed target experiments (where a beam of electrons or photons is collided against a solid target made up of standard atoms) are used to measure the high x regions with low Q. Low x regions are seperately measured in colliders like HERA (Hadron Electron Ring Accelerator), which also uses electron on protons to measure correct dependencies. High x information regarding gluons is gathered from distributions of jet transverse energy mostly at the Tevatron, which is the only facility capable (as of the writing of this section)

of generating events at those energies.

When two partons collide, the result is most often a rather uninteresting QCD jet event, or some other type of well-understood, and hence not very interesting, hard scatter. Only occasionally will particles of interest be produced. Those particles that are produced will tend to decay rapidly into the few stable particles in the standard model. In order to catch those particles before they can escape, the detectors used on particle colliders are some of the most advanced pieces of machinery in the world.

Chapter 4

The CDF Run II Detector

4.1 Overview

By its nature, a detector is something that detects things. This is not a profound statement, but it does have profound consequences when it comes to High Energy Physics. One of the simplest particle detectors is the geiger counter. Whenever a charged particle passes through a tube of gas, the energy deposited causes a discharge amid the gas, which eventually results in the clicking sound that marks the passage of radiative particles. A geiger counter is a direct measurement device. It measures particles which actually appear inside the detector. However, in modern High Energy Physics, we do not enjoy that same luxury.

The universe that we see every day is composed of a number of particles that we already, for the most part, understand. The matter that we touch every day consists of protons, neutrons, and electrons, all of which have been the subject of numerous experiments. The light of the sun comes to us in the form of photons, whose properties have been the subject of examination since before we even knew of its existence as a quantized particle.

Over the past fifty years, the frontiers of physics have been pushed far beyond the realm of the familiar. Quarks and gluons, once the subject of nearly limitless theoretical speculation are now the everyday stuff of experiments. We now probe at particles like the W and Z boson, and the top quark, all of whom are incredibly massive, and all of whom are unstable enough to decay before they can be measured

by any conceivable device. Our only method of measuring any of the properties of these massive, short-lived products is by reconstructing them from their decay products.

All massive, unstable particles eventually decay into smaller, long-lived particles. By measuring those particles, it becomes possible to reconstruct the original event. A decaying particle creates lighter and lighter particles, until the only particles remaining from the original decay fit into several distinct categories:

- Electrons: Charged, stable particles, electrons leave indicators of their passage throughout the detector until they are stopped.
- Muons: Charged particles, muons are stable enough to travel through the whole detector. Their low rate of interactions allows them to travel through a great deal of matter.
- Photons: Photons are neutral, massless particles that interact electromagnetically inside the detector, but not leaving any other evidence.
- Quarks: Because of QCD, quarks cannot exist by themselves (in the so-called "bare" state). Because of that, quarks released by a decay rapidly undergo a process known as hadronization, resulting in a small cloud of lower energy hadronic particles, tightly clustered in space, called a jet.
- Gluons: Like quarks, gluons carry color, the QCD equivalence of charge, and cannot exist by themselves. Gluons also decay into jets, mostly indistinguishable from quarks.
- Neutrinos: Neutrinos are completely invisible in most detectors, as their interaction rate is so low that they can pass through a detector, a building, and indeed the entire Earth without even slowing down. Neutrinos are detected, not by their presence, but by their absence, using a quantity known as Missing Transverse Energy (MET).

A modern detector is built to identify, and distinguish between, all of those particles.

Figure 4.1: CDF Run II

4.2 Detector Basics

CDF Run II is an example of a modern, multi-purpose detector, capable of using the rich collision environment of a high energy hadron collider to analyze multiple possible final states. To do this a modern detector is built in layers that, together, allow us to distinguish between each of those previous particle categories. CDF Run II has, like most detectors, five distinct components.

- Tracker: The tracker responds to the passage of charged particles. Usually consisting of multiple strips of silicon, or fields of charged wires, the tracker gives precise position information regarding the passage of particles, meaning that the detector can reconstruct the "track", or the path the particle took.

- Solenoid: In order to distinguish between a positively and negatively charged particle, detectors are often equipped with a solenoid which creates a magentic field inside the detector. This field bends positively charged particles in one direction and negatively charged particles in another, allowing the tracker to distinguish their charge and measure their momentum based on the bend in their tracks. The shape of the solenoid, and the field it creates,

fits the geometry of a beam-based collision, and forces the rest of the detector to adapt cylindrical geometry.

- Electromagnetic Calorimeter (ECAL): The ECAL is a device for measuring energy. Composed of a material that interacts well with electromagnetic particles, the ECAL acts as a brake of sorts, using the shower of energy created as particles pass through the detector to measure the original energy of the particle. This measures the energy of electromagnetic particles by counting the energy absorbed in stopping them.

- Hadronic Calorimeter (HCAL): A dense structure, usually composed of scintillators for measuring energy deposition, mixed with layers of heavy metal for slowing down particles and causing them to release showers of energy, the HCAL is useful for measuring jets and other hadronic partices in the detector. This also acts as a brake, absorbing all of the energy from both hadronic particles.

- Muon Chambers: Muons have an incredible ability to penetrate through the layers of the detector. They do, however, interact electromagnetically, allowing the placement of detector chambers of this type outside of the main detector body to measure the passing of individual muons.

Because of the structure of the detector, we are forced to construct the detector in a certain order. The tracker must come first, before the "brakes", either the ECAL or HCAL. The ECAL, which stops EM but not hadronic particles, must come inside the HCAL. And the muon chambers must go on the outside.

These layers can be created because different materials interact differently depending on what type of particle is sent through. Materials are generally categorized by two measurements. Radiation length (X_0), the measurement of how far a particle before electromagnetic interactions (Brehmsstrahlung and pair production) reduce its energy by a factor of 1/e, and Interaction Length (λ), the mean interaction length for hadronic interactions. EM calorimaters, for instance, have a high radiation length, to block EM particles, but a low interaction length, so as not to interfere with mesons and other strong particles.

With these five components, we can identify the individual classes of particles previously mentioned.

- Electrons: Electrons leave a track in the tracker, and deposit most of their energy in the ECAL. They do not penetrate farther through the detector.
- Muons: Muons leave a track in the tracker, but do not react much inside either the ECAL or the HCAL. They leave a set of hits in the muon chamber, sometimes referred to as a "stub". They are considered to be minimally ionizing, leaving a minimum of energy inside the calorimeters along their track.
- Photons: Photons leave a cluster of energy in the ECAL. Unlike Electrons, they do not leave a track.
- Jets: Quark and gluon jets create a cascade of particles, identifiable from their large energy deposition in the HCAL, especially compared to what they leave in the ECAL.
- Neutrinos: Neutrinos are measurable because they leave virtually no trace at all in the detector. However, since momentum should be balanced symmetrically in the detector, their presence can be traced by a momentum imbalance.

We will address each component in turn. The reconstruction on physics objects will be discussed in greater detail in Chapter .

4.3 Detector Geometry

The CDF Run II detector is an extremely large piece of metal and silicon, a 5000-ton piece of machinery sitting on the B0 collision point at the Tevatron. The detector is described by a simple coordinate system, generally analogaous to cylindrical coordinates. The three coordinates are z, the axial direction, ϕ the axial angle, and η, or pseudorapidity, which is defined as:

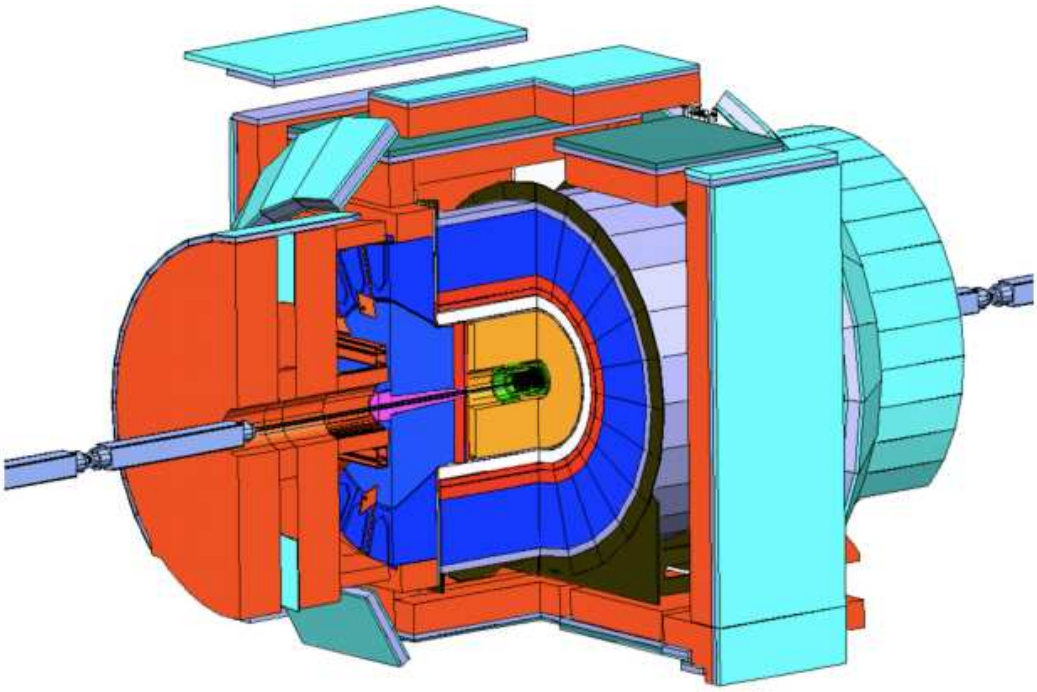

Figure 4.2: Cutaway view of the CDF Detector, showing the tracker, solenoid, ECAL, HCAL, and Muon chambers.

$$\eta = -ln(\tan(\frac{\theta}{2})) \tag{4.1}$$

where θ is the angle between the vector and the vector perpendicular to the z-axis in the same ϕ plane. η is useful for hadron collider physics because the quantity is Lorentz invariant, meaning that along any boost in the z-direction, the $\Delta\eta$ is the same. Because the collisions take place at rest in the x- and y-directions, the only momentum they tend to have is in the z-direction, and η serves as a constant measure of angle regardless of the initial boost of the particles. Because of this invariance to boosting, the production of particles is approximately constant in η. An η of 0 refers to the vector that is perpendicular to the beamline at the center of the detector (going straight into the center of the detector), where an η of 3.6 is approximately the end of the forward portions of the detector., at a θ of 0.054.

Broadly, the CDF Run II detector is divided into two parts, the barrel, and the endcaps. Both get their name from actual, physical components. The barrel is a cylindrical construct which, prior to detector activation, was sealed with the insertion of two large endcaps. As a result, the detector physically breaks into three pieces. The barrel region is considered to extend out to $|\eta| \leq 1.0$, the extent of the Central Outer Tracker, while the endcap region extends out to $|\eta| \leq 3.6$ or higher.

Particle behavior in the two regions is very different. High mass decays tend to produce particles with significant transverse momentum (p_T), which tend to be observed in the barrel. Lower mass or lower energy events tend to go forward and backward in the direction of the beams, and fill the endcap.

4.4 Tracker

An ideal tracker would measure position infinitely well, in three dimensions, without subtracting from the energy of the particles that pass through. Unfortunately, a real tracker is confined by the materials that we have available to us, the space that we can afford to devote in the detector, and the budget of the project.

The purpose of the tracker is simple measurement of the trajectory of a particle. This requires a tracker to strive to have a finely articulated detection mechanism, capable of determining the position of a particle to high precision, but also to minimally interfere with the particle so as not to smear the energy measurements performed in the calorimeter.

The CDF Run II tracker is the innermost component of the detector, running right next to the beam pipe, and consists of multiple layers of sensors. From the inside out, the tracker consists of one layer of single-sided silicon, the Layer 00 (L00), five layers of an inner silicon based tracker (the SVX II), one to two layers of the Intermediate Silicon Layer (ISL), and eight superlayers of the Central Outer Tracker (COT). Together these three devices allow a high resolution of particle tracks within the CDF Run II detector.

The effects of tracking on detector physics are discussed in more detail in Chapter 6.3.

4.4.1 Silicon Layer 00 (L00)

At the center of the CDF detector is an addition made during the Run IIA upgrade, the Layer 00 [18], a layer of single-sided silicon crystals installed almost directly on the beam pipe, from a radius of 1.35 to 1.62 cm. Each detector is a strip of silicon, 7.84 cm in length with a total hit resolution of approximately 6 μm.

The L00 is a Run II Upgrade improvement, meaning that it was proposed and installed as an upgrade to the detector instead of being present in the original run. The purpose of the L00 was to add to the resolution of the SVX II, and to increase our ability to do vertex reconstruction, and essential component in b-physics. The L00 was expected to increase our impact parameter resolution to:

$$\sigma = 9 \bigoplus \frac{34}{p_T} \rightarrow 6 \bigoplus \frac{22}{p_T} \mu m$$

for tracks that do not pass through SVX II hybrids.

We do not use b-tagging in this thesis, but the increased resolution provides additional information for tracking-based physics at CDF.

4.4.2 Silicon Tracker (SVX II)

The SVX II, so named to distinguish itself from CDF Run I's SVX I, is a five-layered silicon detector placed near the interior of the detector, running from a radius of 2.4 to 10.7 cm [29]. It provides information on tracks far out into the $|\eta| \leq 2.0$ region in three dimensions. It is possibly the most complex component of the detector, with 405,504 channels, and a resolution per measurement of 12 μm.

Silicon strip sensors can be made "double-sided". The 90 degree stereo sensors have strips running on both sides of the silicon strip, one side measuring r-ϕ positional information, and the other recording r-z information. Small angle stereo layers also have two layers, but there the difference in angle between the two sides is very slight, allowing for more precise r-ϕ information. There are two sets of sensors, silicon layers 0, 1, and 3, which are 90 degree stereo sensors, and layers 2 and 4, which comprise the small angle stereo layers.

4.4.3 Intermediate Silicon Layers (ISL)

The ISL was designed to help assist with tracking in the endcaps as well as the center, supplementing the loss of coverage created by the end of the COT. In the central region, the ISL is a single layer of silicon at a radius of 22 cm. In the region $1.0 \leq |\eta| \leq 2.0$, the ISL consists of two layers of silicon at a radius of 20 and 28 cm. The primary purpose of this configuration is to extend lepton ID and b-tagging capabilities out to the endcap region to compensate for the lack of COT coverage.

Because of its distance from the center of the detector, the ISL has a lower rate of radiation damage, and use somewhat longer strips then the SVX II. Otherwise, the two systems are very similar. The ISL has 268,800 readout channels, with a resolution of 16 μm on the axial side, and 23 μm on the stereo side.

4.4.4 Central Outer Tracker (COT)

The COT is an open cell wire drift chamber detector, a cylinder that fits around the inner tracker, running from an inner radius of 44 cm to an outer radius of 132 cm, in the region of $|\eta| \leq 1.0$, allowing coverage for the entire barrel region [8]. The combined COT has 2,520 drift cells, and 30,240 readout channels, and a resolution per measurement of 180 μm. The interior of the COT is filled with a gas mixture of Ar-Et-CF_4 (50:35:15), which has a drift velocity of 100 μm/ns, and a maximum drift distance of 1 cm.

Unlike the inner detectors, the COT is a wire drift chamber, a chamber filled with a series of conductive wires, and a mixture of gas. There are two types of wires inside the COT, the field wires, which project the field, and the sense wires that detect particle movement. When charged particles pass through the chamber, they cause the ionization of the gas in a field created by the field wires, leading to a cascade of charges striking the sense wires, which serves as a signal.

Each superlayer has twelve sets of wires in it. Hence a particle track should come near at least 96 wires on its trajectory through the drift chamber in the 100 nsec total drift time. These 96 points provide information regarding the r-ϕ position of the particle with extraordinary accuracy given the many measurement points provided. 48 of the COT layers with a 3 degree offset to give us small-angle stereo information about the z position of the particles.

The purpose of the COT is to give extremely detailed information about the track. The COT is meant to work in concert with the r-z and r-ϕ information from the SVX II in order to provide precise and accurate information regarding the total trajectory of a particle.

4.5 Solenoid

The Solenoid, although vital, is a fairly uninteresting part of the detector. Designed to last for up to ten years, the solenoid coil provides a 1.5 Tesla magnetic field to a region 2.8 meters in diameter and 3.5 meters long. The solenoid itself uses a uniform current density of 1200 A/m and is made of NbTi conductor. The

solenoid is indirectly cooled by liquid helium, and has a relatively minimal effect on particles passing through it.

4.6 Electromagnetic Calorimeter (ECAL)

The ECAL functions essentially as a brake for electromagnetic particles, primarily photons and electrons. High energy electromagnetic particles lose most of their energy in the high radiation length material, while the low interaction length depth reduces the amount of hadronic energy lost.

The CDF Run II detector has two distinct ECAL designs, the barrel ECAL, and the Endcaps. In order to cut down on backgrounds from the decay of neutral mesons, shower detectors are placed inside the calorimeters.

4.6.1 Shower Detectors

There are two shower detectors in CDF Run II, the Central Electromagnetic Shower Detector (CES) and the Plug Electromagnetic Shower Detector (PES). These detectors serve to measure the transverse shower profile of an electromagnetic event, in the hopes of distinguishing between a single shower (indicating a prompt photon), and a double shower (indicating the decay of a neutral meson to two prompt photons). In both cases, the shower detectors are embedded at approximately $6X_0$ inside the ECAL.

The CES consists of cathode strips used to provide z information, and anode strips used for ϕ information. The CES provides a position resolution of 2 mm at 50 GeV which compares favorably with that provided by other detectors.

The PES consists of two layers of scintillating strips, the U layer, offset from the radial direction by +22.5 degrees, and the V layer, offset by -22.5 degrees. This provides the same functionality as the central CES, with a position resolution of approximately 1 mm.

Table 4.1: ECAL properties at CDF

	CEM	PEM
Coverage	$\|\eta\| < 0.9$	$1.1 < \|\eta\| < 3.6$
Thickness (X_0)	$19X_0$	$21X_0$
Thickness (λ)	1λ	1λ
Sample (Pb)	$0.6X_0$	$0.8X_0$
Sample (scintillator)	5 mm	4.5 mm
Resolution	$13.5\%/\sqrt{E_T} \bigoplus 1.5\%$	$16\%/\sqrt{E_T} \bigoplus 1\%$

4.6.2 Barrel

In the central region, the ECAL functionality is handled by the central electromagnetic calorimeter (CEM), which consists of modules referred to as "towers", which have a diameter of 0.11 in η and 15 degrees in ϕ. Each wedge consists of layers of lead and polystyrene scintillator intermixed to a depth of 18 radiation lengths. The resolution of the calorimeter was expected to be $13.5\%/\sqrt{E_T} \bigoplus 1.5\%$.

4.6.3 Endcap

The endcap, or plug, ECAL consists of 23 layers of lead/polystyrene scintillator material known as the plug electromagnetic calorimeter (PEM). There are 960 towers involved in the plug calorimeter, The Barrel ECAL consists of 23 layers of lead/polystyrene scintillator material, arranged into modules referred to as "towers". There are 960 towers in the plug ECAL, covering the region $1.1 \leq |\eta| \leq 3.6$. The towers are segmented into different sizes, with towers of 15 degrees for $|\eta| > 2.11$ and 7.5 degrees for $|\eta| < 2.11$. The plug calorimeters were designed and installed as part of the Run II upgrade. The design energy resolution of the plug ECAL is approximately $16\%/\sqrt{E} \bigoplus 1.0\%$.

Table 4.2: HCAL properties at CDF

	CHA	WHA	PHA
Coverage	$\|\eta\| < 0.9$	$0.7 < \|\eta\| < 1.3$	$1.1 < \|\eta\| < 3.6$
Thickness	4.5λ	4.5λ	7λ
Sample (Iron)	1 to 2 in.	1 to 2 in.	2 in.
Sample (Scintillator)	10 mm	10 mm	6 mm
Resolution	$75\%\sqrt{E_T} \oplus 3$	$75\%\sqrt{E_T} \oplus 3$	$80\%\sqrt{E_T} \oplus 5$

4.7 Hadronic Calorimeter (HCAL)

4.7.1 Barrel

In the central region, coverage is provided by the Central Hadronic Calorimeter (CHA) and the End Wall Hadronic Calorimeter (WHA). The CHA is constructed of wedges of 15 degrees in ϕ, which are divided into ten towers, each with a range of 0.11 in η. The CHA covers the region $0 < |\eta| < 0.9$. Outside of this region there is coverage from the WHA, which covers the range from $0.7 < |\eta| < 1.3$.

Both the WHA and CHA are constructed out of 1 to 2 inches of steel absorber interspersed with an active layer consisting of 10 mm of acrylic scintillator. The hadronic calorimeter depth runs to approximately 4.5λ, where λ is the intereaction length of the material. The energy resolution of both calorimeters is approximately $75\% \sqrt{E_T} \oplus 3\%$.

4.7.2 Endcap

The endcap, or plug, HCAL is, like the ECAL, 23 layers, consisting of 5 cm layers of iron interspersed with 6 mm of polystyrene scintillator, referred to as the Plug Hadronic Calorimeter (PHA). There are 864 towers in the endcap HCAL, and is 7 interaction lengths deep, compared to only 1 length for the ECAL. The design energy resolution of the plug HCAL is $80\%/\sqrt{E} \oplus 5\%$.

4.8 Muon Chambers

The Muon chambers form the outer layer of the CDF detector, and are visible in orange in Figure 4.3.

4.8.1 Central Muon Detector (CMU)

The CMU is the original Run I set of muon chambers made of single wire cells. Each cells is 6.35 x 2.68 x 226 cm in size, and contain a single wire in the center, which produces a charged reaction whenever a muon enters. Muon stubs are provided for the region of $|\eta| \leq$ 0.6. The CMU is hidden from the main decay products of a collision by the HCAL, and provides limited ϕ and z information. Muons down to a p_T of 1.4 GeV/c are detectable by the CMU.

4.8.2 Central Muon Upgrade (CMP)/ Central Scintillation Counters (CSP)

The CMP is a central upgrade to the detector allowing greater accuracy in muon identification, added during the Run II upgrade. The CMP muon chambers occupy a region behind the CMU and an additional layer of steel shielding. The CMP consists of four layers of single-wire drift tubes stacked on top of each other.

Also installed are 269 scintillation counters, the Scintillation Counters (CSP), which serve to further increase the accuracy of muon measurement inside the central region.

4.8.3 Central Muon Extension(CMX)/ Scintillation Counters (CSX)

The CMX/CSX system was added to improve the coverage of the muon system from $|\eta| \geq 0.65$ to $|\eta| \leq 1.0$ by essentially expanding the central muon system into the outer reaches of the barrel. A series of conical sections of drift tubes (comprising the CMX) and scintillation counters (CSX) were added to the ends of the central muon system, putting 2208 total drift tubes and 324 scintillation counters on the

outside of the muon system. The CMX drift tubes are placed in four layers of twelve tubes each, while a layer of four CSX counters is placed on the inside and outside surface of each sector of the CMX.

Combined, these two systems should have the ability to identify muons down to p_T of 1.4 GeV/c tracks.

4.9 Online Computing

For the most part, CDF is a profoundly uninteresting experiment. Consider the search for the ZZ $\rightarrow \ell\ell\ell\ell$ decay. The CDF detector receives data from events happening once every 396 nanoseconds, several years of which was gathered together to perform the initial analysis, out of which they could only find one candidate event. This is, to be honest, a rare channel, but it gives you some idea of the general rarity of interesting physics. Every collision does not produce new and interesting physics. On the contrary, most events are filled with old and fairly well understood data.

CDF can only function as an experiment as long as researchers avoid being swamped by the sheer amount of data available. There are two steps to this. The first is done by throwing out uninteresting events, the job of the trigger system. The second is by providing each researcher with a comparatively large amount of computing power with which to process the remaining data.

The Trigger is the heart of CDF's data collection abilities; three levels of electronics and computers that exist to basically make one decision for each event, yes or no. There are three levels to the trigger, each one throwing out more events. Those events that do pass have to possess certain traits which physicists have ruled to be interesting, requirements referred to as trigger requirements, and which are grouped into separate trigger "lines". An analysis can only use events that pass one set of trigger requirements. The trigger lines used for this analysis are discussed in 6.5.1.

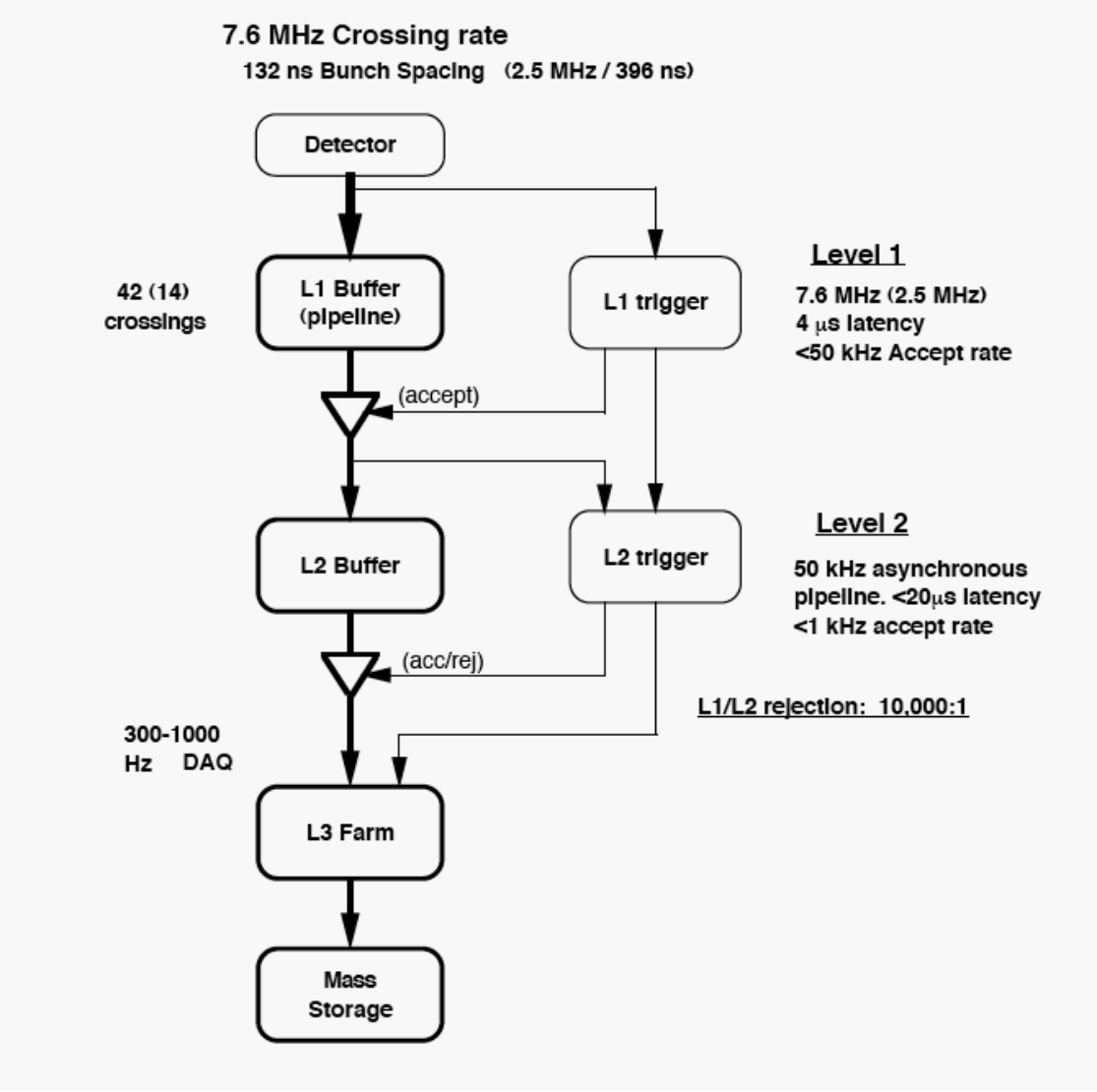

Figure 4.3: Flow Chart of the CDF Trigger System

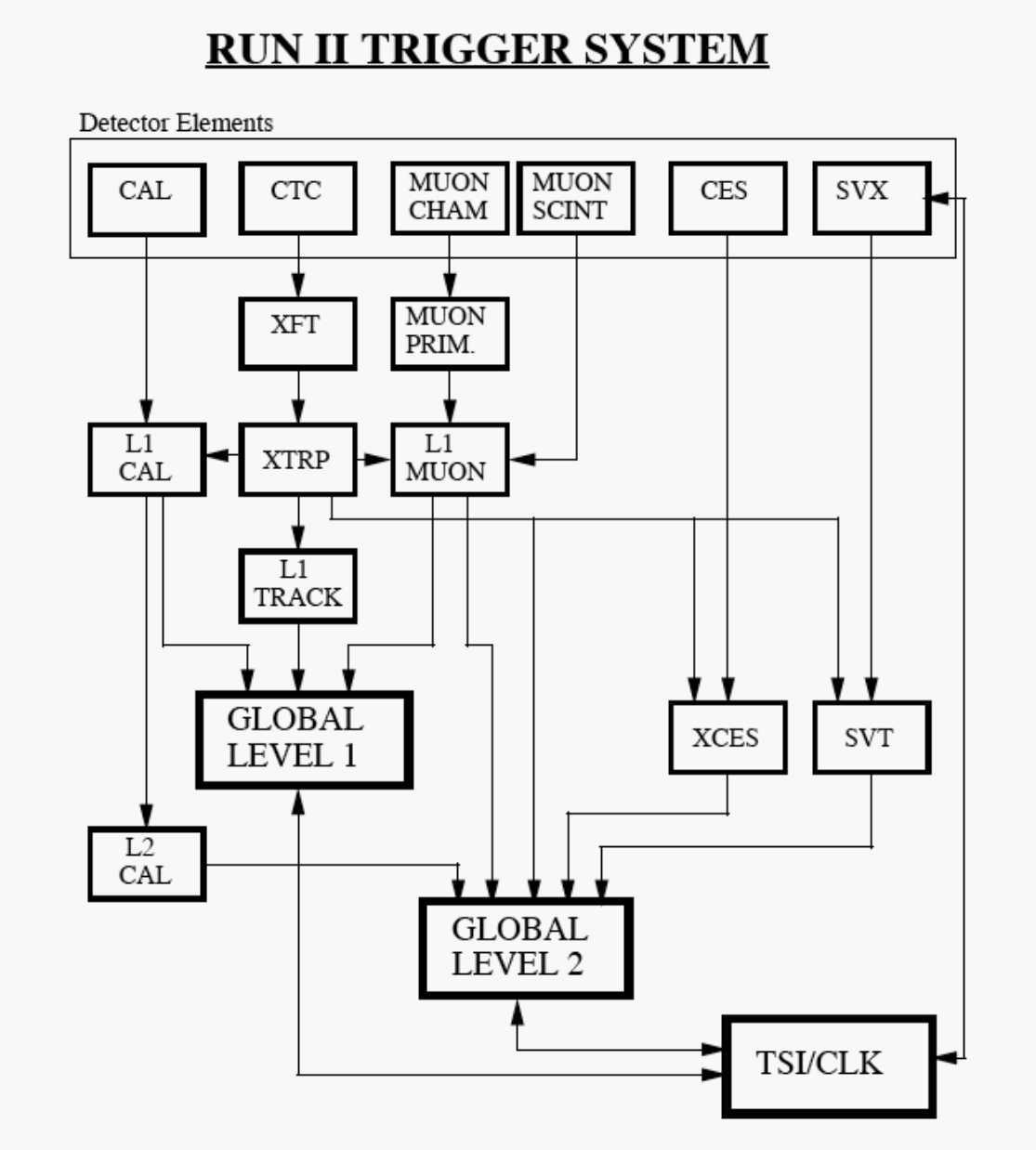

Figure 4.4: Systematic Diagram of the CDF Trigger System

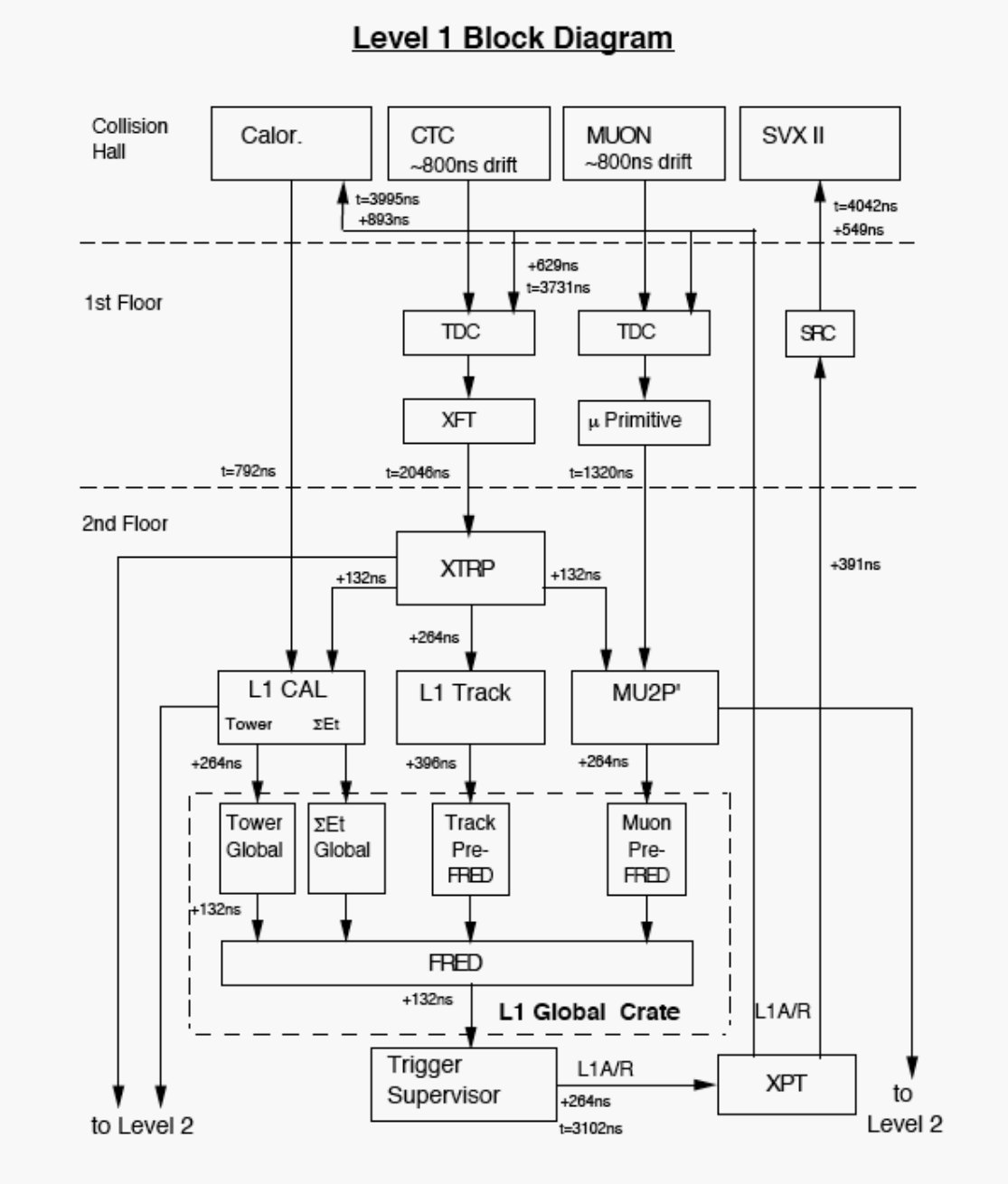

Figure 4.5: Logical Schematic of the CDF Level 1 Trigger

4.9.1 Level-1 Trigger (L1)

The Level-1 Trigger is the most basic level of triggering, consisting of dedicated hardware built for the purpose of determining which events are useful[21]. The output for the Level-1 Trigger is 40 kHz by design. The key limitation of the L1 is time. With a new event happening in the detector every 396 nsec, there is a definite upper limit on the amount of time the L1 can use to make a decision. Although data can sit in the "pipe" for longer then this time, the L1 must be able to make a decision once every 396 nsec. The original design latency of the L1 Trigger is 4 μsec, allowing for approximately ten events to be queued up at a time, undergoing the decision making process. The depth of the L1 buffer, which holds all the event information, is sufficient to hold 14 crossings.

The L1 triggers on electrons, photons, jets, total energy (ΣE_T), and Missing E_T, but only with limited information. Because of the necessity of making a decision every 396 nsec, with the total time of the decision never running above 4 μsec, the L1 trigger has to operate with the minimum amount of computer effort. The L1 triger receives information from the calorimeters, the muon chambers, and the COT, but not from the full Silicon tracker. Requirements are based on simple thresholds on calorimeter triggers for the objects (electrons and such), and quick summation of all towers for the global variables (such as ΣE_T). Track information is added by the eXtremely Fast Tracker (XFT) using information from the COT. The XFT has a ϕ_0 resolution better then 6 mrad, and a momentum resolution of $\Delta p_T/p_T^2 < 2\%$ for tracks above 1.5 GeV.

4.9.2 Level-2 Trigger (L2)

Once an event is accepted by the Level-1 Trigger, it is written into one of four Level-2 buffers. The L2 is more comprehensive then the L1, which translates into more and more time spent analyzing events. The event rate for accepted events for the L2 trigger is estimated at 350 Hz.

The L2 trigger uses several more detailed algorithims to construct events then the L1 trigger. For example, the L1 jet trigger is based upon the energy deposited in a single calorimeter tower, but the L2 uses clusters of towers to create and test

jet events. The L2 trigger can also use inputs from detector components that take more time to process, such as the Central Shower Maximum (XCES), and the Silicon Vertex Tracker (SVT), which reconstructs information from the CES and the SVX II respectively.

4.9.3 Level-3 Trigger (L3)

Unlike the previous two crate-based triggers, the L3 trigger is based on a PC farm, which processes the entire event record, reconstruting the 350 Hz event rate from the L2. The objective of the L3 was to use much more complicated physics algorithms, based on detailed study of the detector and its reconstruction abilities, to reduce the event rate to 100 Hz. The software for the L3 trigger is based on the offline production code, to ensure the best match between the L3 trigger outputs and the actual production data.

Chapter 5

Computing

The fundamental philosophy of CDF Computing is that physicists are smart people, and are collectively much better at doing physics then the people who run their Computing are. There are thousands of problems and challenges that await a physicist seeking to do physics at CDF, and each of them has solutions that we cannot anticipate at the beginning of an experiment.

Because of this we cannot commit the computing platform for CDF to a pre-specified set of analysis tools. We have no way of understanding, or predicting, what types of methods will be used by physicists in undertaking their analyses. It is impossible to design the computing platform with a specific set of pre-existing tools in mind, or around a particular, non-modable production framework. All you can do is give physicists access to a versatile, capable working environment that can run anything they can do on their own desktop, and a modular code package that can be easily modified, and hope that they do not crash your system in the process. The only job of physics computing is to provide physicists with easy and copious access to versatile computing resources and data. All else must be left to the physicists themselves.

Although impolitic to mention, CDF was also profoundly limited by the available budget for the construction of new computer facilities at FNAL. The restrictions on available space, power, and cooling for new hardware forced CDF to become an early adopter of large-scale grid computing technologies. In retrospect this was a very important choice, because not only did it allow an unprecedented

amount of computing resources to be brought to the fingertips of CDF users, but it also provided a test case for the computing models of the Large Hadron Collider experiments, whose computing problems are of the same type, but of greater complexity.

CDF Computing is responsible for three pieces of the experiment, storing and maintaining both the data and the CDF software in a central facility, securing computer access for use by CDF users, and then connecting the two, so that a user can obtain versatile computing power with access to both data and software versions, without being restricted to running on their own desktop.

5.1 Data Storage

Once data leaves the Level-3 Trigger, it goes to tape. At the time the detector was first planned, the data volume expected for Run II was 250 TB [1]. As of the moment I am writing this down, CDF is using 15,606 tapes to store approximately 3.6 PB of data, which will doubtlessly have changed by the time you read this. Nevertheless, despite the occasional panic, CDF continues to store data in a consistent manner, and so far has performed within the expectations of the data storage group. The data is stored on-site at FNAL at the Feynman Computing Center (FCC). The CDF data handling system then transfers the data to analysis sites when required, but this is beyond the scope of this document.

5.2 On-Site Computing

The heart of CDF's computing resides at FNAL: the CDF Analysis Center (CAF). Over the years the singular CAF that started everything off has branched into many separate pools (the GroupCAF, the CondorCAF, and the FermiGrid Glide-In pool), but the principles remain the same. The CAF at FNAL is a dedicated CDF resource that provides rapid access to computing for CDF users, and easy access to on-site data storage at the FCC.

As the central node in the CDF Computing network, the CAF has also served

as the template around which all the distributed analysis farms, the dCAFs, were built. Later the system was used as the testbed for the FermiGrid pool, which also served as the testbed for our expansion into the Grid at large. During the time it saw use as such, the CAF remained a production tool, and was under constant heavy use by the users of CDF.

The CAF is built around the Condor High Throughput Computing batch-management system produced by the Condor Research Project at the University of Wisconsin - Madison. Condor, which is freely available, serves as a full batch-management system, managing the submission, authentication, queueing, and scheduling of jobs. A Condor system administrator can not only set strict guidelines on what jobs can and cannot be run (and who can and cannot run them), but also on what priority each user should have, or each group should have, and adjust resource allocation to match local priorities.

Mechanically, the Condor system depends on a headnode, either a single machine, or a headnode cluster, which houses two permananet daemons, the Collector and the Negotiator. The Collector serves as the recipient of all information regarding the state of either worker nodes in the Condor cluster, or jobs submitted to the system. This information comes in the form of "ClassAds", standard information packets sent out by each worker node and by each job. There are two types of ClassAds, resource ClassAds, representing available computing resources, and job ClassAds, representing jobs that need to be run. The Negotiator daemon then matches resource ClassAds with job ClassAds according to the rules specified by the system administrator.

User jobs gather on the Schedds, or Scheduler daemons, which then communicate their ClassAds to the Collector. These jobs sit there in the job queue until they are assigned to a resource somewhere in the cluster. From there, the schedd opens up a TCP connection to the destination machine, allowing the direct transfer of the job and its attendent files. The job runs on the worker node until it finishes, it suffers a system failure (such as the worker node rebooting), or it is removed for some reason specified by the system administrator. If the job does not complete successfully, it is returned to the queue.

CDF wrote an interface layer using active python daemons to interface between the Condor system and the users. This system provided for an easier submission interface, where the user could use a GUI to actually submit their jobs, and simplified the farm specification system so that the user only needed to know the name of the farm they intended to submit to. Users could also specify an output location for their results, using the same credential they used to submit the job. More importantly, the python scripts acted as an interface to both active and passive monitoring tools. From a webpage, users could monitor the status of their jobs, including the worker node it was running on, the CPU allocation, the memory allocation, and the processes currently running. By using their credential, they could also examine the output of the logfiles, the size of certain files, remove their job if necessary, and even run gdb to examine core files produced by segmentation faults.

The result was a system which removed the traditional overhead of a cluster computing system, the necessity of each user being able to work on the cluster, at the cost of an enhanced maintenance load. A primary administrator had to deal with stuck jobs or malfunctioning nodes, and look for problems in the job submission system, as well as keep an eye out for the normal problems of maintaining a large-scale cluster. The maintenance of the CAF cluster could, however, be covered essentially by a single person, a duty I performed for approximately a year, starting in August of 2005.

5.3 Distributed Computing

After the initial success of the main CAF, CDF made the decision to enhance their computing abilities by running jobs at member institutions. Part of this decision was based upon the relative availability of computing facilities at member institutions, and part on the relative scarcity of space, power, and cooling at Fermilab during that period. This lead to the distributed CAF system (or dCAF system).

The dCAF system had approximately ten member institutions at its height,

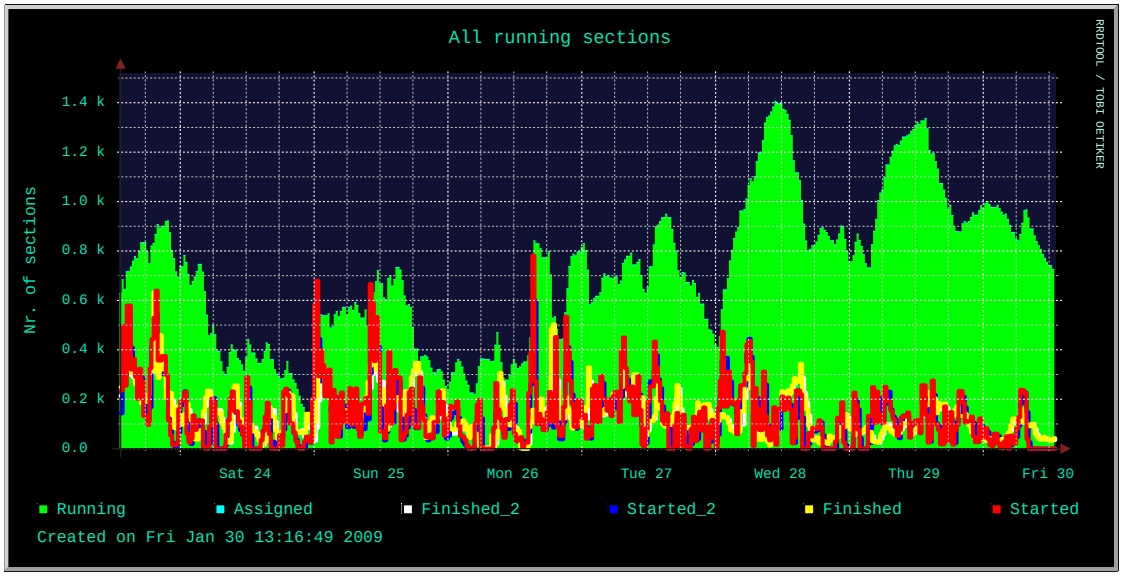

Figure 5.1: 1 week history of jobs run on the Fermigrid CAF

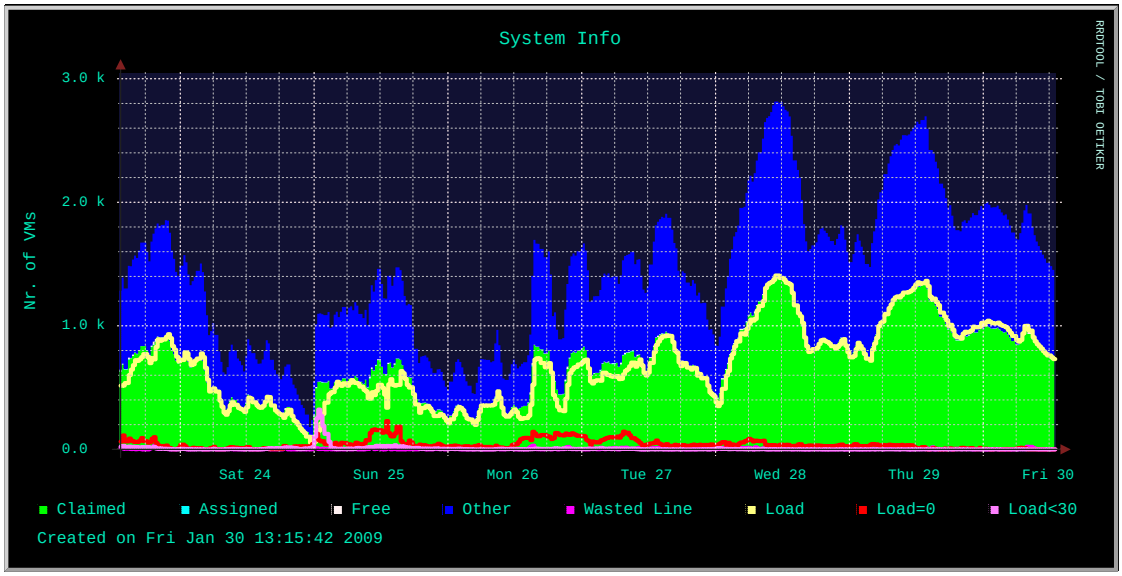

Figure 5.2: 1 week history of the system status on the Fermigrid CAF

each hosting their own small Condor cluster, using the standard CDF CAF python framework to accept and manage jobs. Users at Fermilab could then run their jobs at JPCAF in Tsukuba, Japan, or CNAF, in Bologna, Italy, with the touch of a button. The primary difference was the lack of CDF computing infrastructure at the target institutions. Even though each institution attached the CDF software, most of them had absolutely no access to data, so no data could be processed at the dCAFs.

However, there was a great deal of MC production ongoing at CDF, and the dCAFs were very good at processing MC, and other jobs that did not require access to large datasets. Because local administrators could also help arrange their own priorities, they also provided significant advantages for the hosting institution.

But it rapidly became clear that the future of computing was not going to allow either us or future institutions to build massive farms of machines dedicated to a single experiment. The dead-times necessary for a large scale project were tremendous. In order to have enough computing to meet requirements during periods of intense activity, a massive number of machines would have to be purchased. But since computing activity in HEP is a cyclical process governed by the conference schedule, this leads to long periods of time when computing is severely underutilized. It was also becoming increasingly difficult to find space that people were willing to devote to dedicating computing for a single project.

Eventually, we turned to the Grid.

5.4 Grid Computing

The development of Grid Computing as a practical measure in High Energy Physics had been proceeding alongside CDF's adoption of the CAF system as part of the preparation for the LHC experiments. It was apparent early on that the vast amount of computing needed for the LHC experiments, CMS and ATLAS, would require the use of a grid infrastructure. CDF served as the precursor to those institutions, as it joined the Open Science Grid project (OSG).

CDF joined the OSG when it was in its first real attempt to actually serve

as a practical Grid Computing project. As a result of the relative newness of the project, the user overhead, the knowledge that a user had to possess in order to make effective use of what was then a disparate and very unreliable grid, was very high. The goal of CDF was to take advantage of grid resources, especially those resources which were being brought online for the LHC experiments but not yet utilized by LHC users, without increasing the burden of the CDF user base. This meant that the CAF interface would have to be expanded to cover the Grid; users would see the Grid the same as they saw any of our dedicated clusters, but underneath the interface, a large infrastructure would have to be developed to use Grid resources instead of dedicated worker nodes.

Our solution was to use a system based on what we called "glide-ins", pseudo-jobs that make it easy to run other jobs, to take full advantage of available Grid resources without posing a burden to users.

5.4.1 The Open Science Grid (OSG)

The Open Science Grid (OSG) is a collaborative grid computing project jointly funded by the DoE and the NSF aimed at meeting the increasing demands of science for high-throughput distributed computing. Member institutions run their own sites under a common architecture and with a common method of accessibility, but entirely under local control.

The High Energy Physics projects all have an OSG presence in order to manage their tremendous workloads. Similarly, several other fields maintain OSG sites and participate in the project. The project also provides both expertise and limited technical support for member sites.

CDF was one of the first projects to systematically enable its users to access resources from across the grid.

5.4.2 Glide-Ins

A "glide-in" is essentially the software package of a condor worker node submitted as a job. When the glide-in, having been submitted to an OSG site, gets

assigned to a worker node and begins to run, it activates the daemons normally present in a Condor worker node. Like a regular Condor batch slot, it reports its presence to a Collector specified in its configuration file.

The only difference is that, instead of reporting to a local Collector, the glide-ins all report to a central Collector at Fermilab. Glide-ins that have started running at diverse locations, such as the University of Florida, or UCSD, or Caltech, or the University of Nebraska report back to a central machine at FNAL. The FNAL headnode then sees a standard array of worker nodes; worker nodes that just happen to be geographicaly distributed to regions across the United States, and eventually across the world.

Once a job is assigned to one of those worker nodes, information is exchanged with the daemons that are running on top of the local site's batch system. The job itself is packaged up as a tarball on a web server and brought through a direct http download. The result is that CDF has managed to turn resources at Grid sites around the world into a dedicated computer cluster, while the local sites never have to know who or what is running at their site. It allows CDF to centrally assign priorities and allocate resources, while simultaneously running their jobs on distributed nodes.

5.4.3 Generic Connection Broker (GCB)

The architecture of Condor requires communication between the schedd and the worker node. Under the glide-in system, the schedd is located at FNAL, while the worker node is located at local sites. The schedd has to be able to open connections to the worker node. However, this procedure does not work through Network Address Translation (NAT), or through firewalls, both of which are present around worker node clusters.

In the NAT case, which is most common, the worker nodes sit on their own private network to avoid eating up valuable IP addresses. As a result, the address that they report to the Collector is a private network address. Because the connection from the worker node is opened from the worker node, this problem does not effect communication from the worker nodes to the Collector. However, once

the job is assigned, the address is passed off to the schedd, which usually fails to open a connection to a private address.

The solution to this is the Generic Connection Broker (GCB), a package developed for inclusion in Condor. CDF was the first major facility to test GCB.

In GCB, a series of nodes is established as GCB servers. When a glide-in job starts, it opens a permanent TCP connection using X509 authentication back to the GCB server. The GCB server then acts as an intermediary. When a schedd is handed a worker node for assignment, it is passed an address that points to the GCB server, and an ID string for the worker node in question. All communication then passes through the GCB server.

This allows for communication with any node that has outbound communication. With the continuing drought of IPv4 addresses, many computing centers are hiding their actual clusters on private networks, making GCB a vital service for Condor on Grid systems. GCB was commissioned in CDF mostly due to my work testing and integrating it. It was first used in large scale in the NAMCAF.

5.4.4 North American CAF (NAMCAF)

Glide-ins were originally tested on dedicated clusters, such as the Fermilab OSG site, where we had full control over the worker nodes, the addresses, and actual access to the site. The first attempt to expand the glide-in system to a wider audience was the North American CAF, or NAMCAF, which was the culmination of my service projects.

The goal of the NAMCAF was to build a system where CDF users could submit their jobs to a central headnode cluster, as in a standard CAF or dCAF, and then those jobs would harvest resources from the grid. The first test was to use central glide-ins to harvest resources from sites that we already owned - CDF sites like UCSD or Fermilab. Once that was complete, we branched out to the CMS Tier 2 sites. In the run-up to the LHC turn-on, the computing resources that were to be dedicated to the LHC experiments were being deployed at the Tier 2 sites, but were not yet being used by their respective experiments, giving us a window to use their underutilized resources.

As of the time I left the project, we had succeeded in running jobs on all the CMS Tier 2s, the first time that CDF had deployed wide-scale usage of computing resources at non-CDF institutions. We had also managed to get limited job slots at various other sites, although the relative inaccessibility of the non-CMS sites limited their utility. However, by any measure, we were effectively using not only our own resources, but whatever spare resources were not being used by other experiments on the OSG.

Chapter 6

Leptons and Jets

6.1 Overview

The title of this thesis refers explicitly to the final state that we are searching for, two leptons and two jets. What the detector produces, however, is a series of analog and digital data from the systems described previously. From there, we have to construct two leptons and two jets.

The key to this is the properties discussed earlier.

- Electrons: Leave a track in the tracker, and energy in the ECAL
- Muons: Leave a track in the tracker, minimum ionizing energy in the ECAL and HCAL, but penetrate through to the muon chambers.
- Jets: Leave multiple tracks in the tracker, some energy in the ECAL, and the bulk of their energy in the HCAL.

Because of this we can identify electrons, muon, and jets with fairly high accuracy.

All values of η in this section refer to detector η unless specifically labeled otherwise.

6.2 Backgrounds

In a $ZZ \rightarrow \ell\ell jj$ event, there will be several types of particles within the detector that will show up in the final analysis. There are, of course, the two leptons and the two jets from the ZZ hard scatter. There are also going to be jets that are created in QCD interactions, or that come from the other quarks and gluons that were inside the colliding protons. Often these are extremely high momentum objects that are oriented down the beam pipe and never appear in the detector, but sometimes you see traces of them. This background, which comes from the actual $p\bar{p}$ collision is referred to as the "underlying event", and includes initial and final state radiation as well as other beam-beam effects.

A second source of non-scatter background can come from out-of-time signals. The passage of particles through the detector is not always a simple task, and you sometimes have the effect of energy and particles from a previous event showing up in a current event, due to either delay in the machinery, or an actual "late" particle (although the later is very rare at CDF). This is accounted for, along with noise, in the minimum bias calculation. Minimum bias events are events where the only noise in the event comes from beam crossing, and there is no hard scatter. This is well measured at CDF.

To summarize, there can be noise-based signatures in the detector, usually in the form of energy in the Calorimeters, as well as real particles, gluons and quarks releasing large amounts of particles into the detector. All of these add up to make a formidable background.

Let us look for a moment at the backgrounds that can fake each signature.

- Electrons: Electrons are formed from a track and energy deposited in the ECAL. Therefore electrons can be faked by:
  - A photon (no track) providing energy in the ECAL and a track in the calorimeter from a nearby electron. Common in Bremsstrahlung radiation, where a photon in the detector undergoes showering to $\gamma \rightarrow \gamma e^+ e^-$. This is limited by a conversion check discussed later. Most photons come from the decay of $\pi^0 \rightarrow \gamma\gamma$, and are effectively reduced

by isolation as well.

  - A charged pion (π^+/π^-) from a jet converts via QCD charge exchange into a pion, which immediately decays via $\pi^0 \rightarrow \gamma\gamma$, leaving most of its energy in the ECAL. This produces both a track and an EM cluster without the normal signature of a hadronic particle. Reduced by isolation.
  - Decay of a heavy quark (b,c) into an electron in the process $b \rightarrow e\nu X$, where X consists of a small shower of hadronic particles. Reduced by isolation.

- Muons: Muons tend to be cleaner then electrons, because the muon system takes advantage of their low interaction. Because muons do not interact well with matter, the muon chambers can be protected by tons of steel and other heavy materials that will stop almost any other particle, but the muon will still get through. A general rule of thumb is that only a muon can fake a muon signature.

  - Punch-through to the muon chambers, in which another particle makes it all the way through every layer of the detector to the outer muon chambers. A very, very rare event.
  - Decay in flight. There are several particles, such as the K mesons or the pion, that decay into muons. If those decay "in flight", while they are in the detector, the result will be the release of a muon from a jet particle. This is limited by isolation and a quality cut on the track fit, which eliminates in flight decay by noticing kinks in the track due to the decay.
  - Decay of a heavy quark (b,c) into an electron in the process $b \rightarrow \mu\nu X$, where X consists of a small shower of hadronic particles. This is especially difficult as a muon produced in this manner will pass through all barriers and enter the muon chambers. This is limited by calorimeter isolation.

- Jets: There is no such thing as a "fake" jet, since a jet is just a wide cone of energy in the calorimeters, but there can be sources of jets that do not originate from the physics of the hard scatter. The primary issue in jet reconstruction is not identification, or suppressing fakes, but are in improving the resolution of the jets themselves.
  - Jets from QCD Initial State and Final State radiation (ISR/FSR), part of the underlying event.
  - Random energy (noise, particles from ISR/FSR) that form clusters of energy grouped together by chance.
  - Very noisy leptons (ones that leave large amounts of energy scattered through the detector) may actually fail the lepton cuts and be classified as jets. This may include objects such as electrons with large brehmstralung fractions, resulting in e^+e^- conversion pairs throughout the tracker.

6.3 Tracking

6.4 Tracking Algorithims

There are three major methods for reconstructing a track from physical data. All of them use a type of "seeding", using hits in certain layers of a detector to form a "seed", the initator of a search, and then looking for tracks that lead to that seed. Over time, CDF has investigated and optimized all three methods [23].

- **Outside-In:** Take hits in the very exterior ring of the detector as the seed, and then extrapolate inwards, looking for a track.
- **Inside-Out:** Take hits in the interior of the detector as the "seed", and extend their flight path outward, looking for a consistent track.
- **Silicon Only:** An outside-in method using two 3D points on the outer layers as a seed. Fast enough to be performed in the Level 3 trigger.

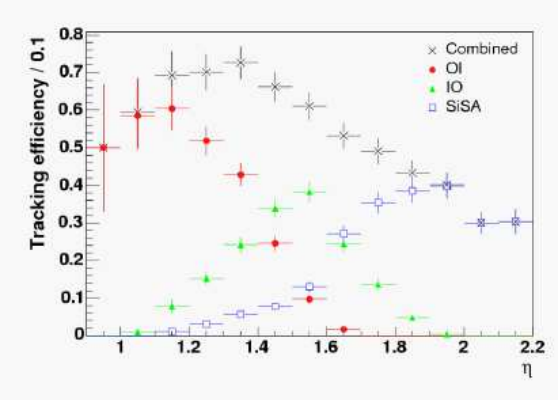

Figure 6.1: Efficiency of tracking algorithims as a function of η

We discuss these three methods below.

6.4.1 Outside-In Tracks

The preferred method of assembling a particle track is the so-called outside-in method, looking for evidence of a track in the outer layer of the COT and then extrapolating it back to the center of the detector using COT and Silicon hits. The Outside-In method is preferred because of the relative dispersal of tracks in the outer layer of the detector.

If the COT were unrolled, the inner layer, which is 44 cm from the beam pipe center, would be about 2.8 meters long. The outer layer, 132 cm from the collision point, would cover 8.3 meters. Since a good track is present in both the inner and outer layer, the tracks are on average more dispersed in the outer layer. This means that every measurement in the outer layer of the COT has much less interference from other tracks.

There are two methods used to assemble a track from the hits in the COT superlayers. First is simple segment linking, matching all the hits in the COT with a probable trajectory. The second is the histograming method, which creates a profile containing the sum information of all the hits, and uses the center and shape of the profile to evaluate the track. The histogramming method can be faster, but has a weakness to situations with large multiple scattering, which distorts the

shape of the histogram. In CDF both methods are used and merged in the most common tracking algorithims.

6.4.2 Inside-Out Tracks

Inside-Out tracks are the tracks least utilized in CDF. Even though it is possible to trace a track from the crowded inside to the more sparsely populated exterior of the tracker, the precision is much lower. Nevertheless, we use Inside-Out tracks to look for patterns that the Outside-In algorithims might miss.

6.4.3 Silicon-Only Tracks

The stand-alone silicon tracks start with two 3D points from the outer layer of the silicon tracker, and operate from there in an outside-in manner. They define their basic search around a "road", a helix formed by the two exterior points and the center of the beamline. From there they attempt to use the other silicon layers in a progressive road search to find the proper track. Attempts to use a single 3D point, or one 3D point and one 2D point resulted in much higher fake rates.

6.5 Leptons

The Z can decay into three particles classified as leptons, the electron (e), the muon (μ), and the tau (τ). Because of the nature of the τ, it decays before it can leave the interior of the detector, so we discount it as a final state particle of interest. The effect of this on our analysis is discussed in Section 7.3.1.

As mentioned earlier, the CDF Run II detector was built in part with the idea of identifying both electrons and muons. Years of work with the detector has allowed us to assemble lepton categories, dividing detector information into certain categories based upon detector components in order to create different classes of leptons. Categories exist for both electrons and muons.

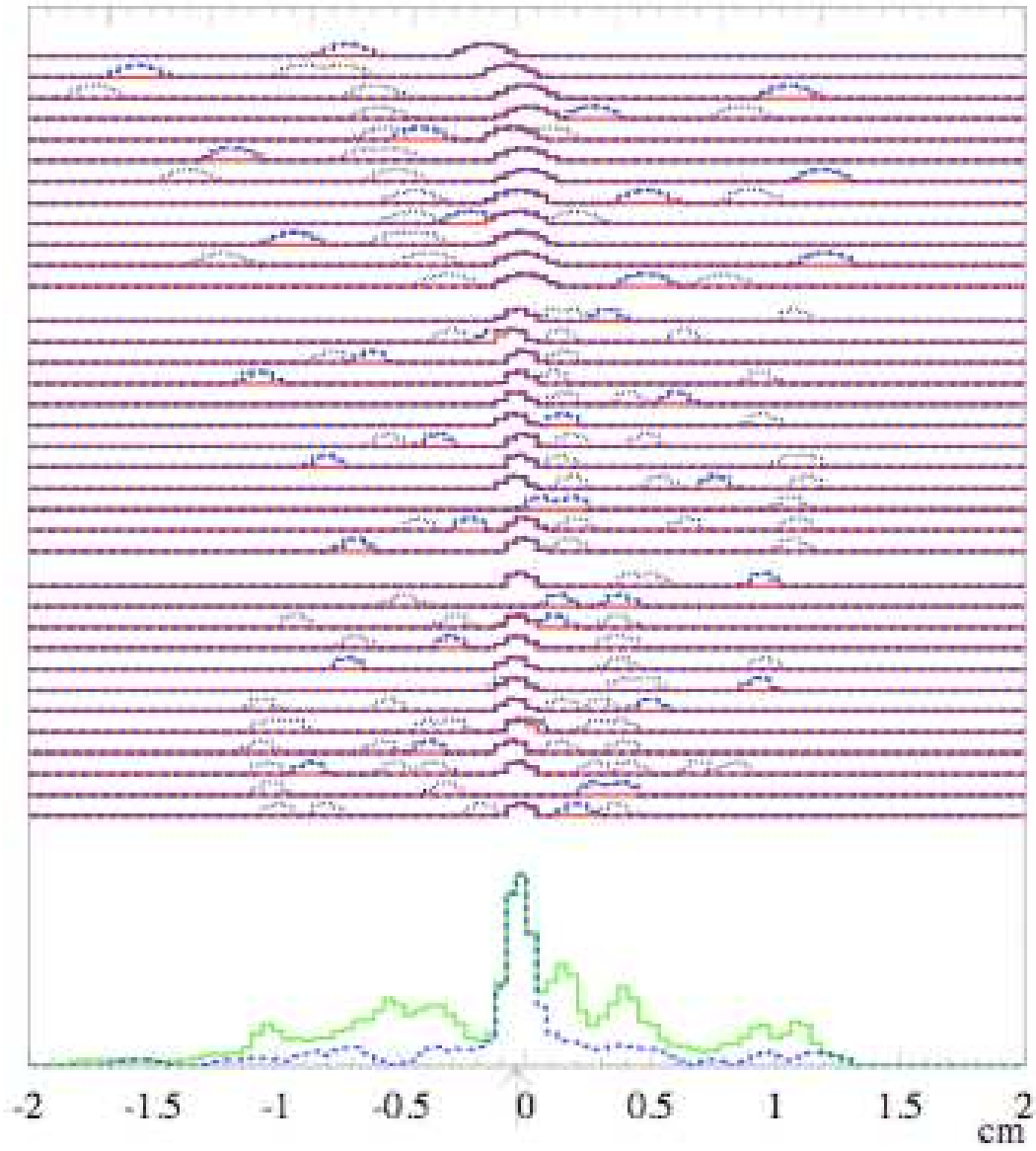

Figure 6.2: Diagram of COT hits used in the histograming reconstruction method

6.5.1 Trigger Paths

Leptons are more distinctive then jets as a signature of the dilepton-dijet final state. Jets are a natural background process for the detector, and are produced in every hard scatter collision in the detector. Leptons, on the other hand, are relatively rare. High p_T leptons in particular, with $p_T > 10$ GeV/c, are especially rare, since most background leptons come from relatively low momentum b or c quark decays.

In CDF, data is accumulated in several "Trigger Paths", each one of which has its own requirements at the Level 1, 2, and 3 triggers. Each Trigger Path has a separate purpose, but they are all geared toward general analysis, allowing the user to create an analysis strategy as unconstrained as possible.

We use several of the standard CDF lepton trigger paths, which contain data taken by events with high momentum leptons. Those trigger paths, as well as their requirements are listed below:

- ELECTRON_CENTRAL_18 This is a central electron trigger incorporating both calorimeter and tracking information with an acceptance rate of 64, 2, and 1 Hz at Levels 1, 2, and 3 respectively. This adds up to a cross-section of 50nb and a trigger efficiency measured as 96.2 ± 0.6%.

  - Level 1: A central ($|\eta| < 1$)EM trigger tower with $E_T \geq 8$ GeV. If the cluster has $E_T < 14$ GeV, E_{HAD}/E_{EM} must be less then 0.125. There must be matched XFT track with $p_T \geq 8$ GeV/c.
  - Level 2: A central EM cluster with $E_T \geq 16$ GeV and $E_{HAD}/E_{EM} \leq 0.125$, with a cluster from adjacent towers with $E_T > 7.5$ GeV . There must be matched XFT track with $p_T \geq 8$ GeV/c.
  - Level 3: A central EM cluster with $E_T \geq 16$ GeV and $E_{HAD}/E_{EM} \leq 0.125$. The seed tower of the EM cluster must be matched to a fully reconstructed 3D track with a minimum p_T of 9 GeV/c.

- MUON_CMUP18

This is a central ($|\eta| < 0.6$) muon trigger using the CMU and CMP, as well as tracker information. The trigger accept rates were 30, 4, and 0.15 Hz at Levels 1, 2, and 3 respectively, and the efficiency is measured to be 89.8 $\pm$ 0.5%.

  - Level 1: A CMU stub with $p_T \geq 6$ GeV/c matched to an XFT track with $p_T \geq 4.0$ GeV/c and a CMP stub.
  - Level 2: None.
  - Level 3: A fully reconstructed 3D COT track with $p_T \geq 18$ GeV/c matched to the CMU stub with $|\Delta X|$ of 10 cm and to the CMP stub with $|\Delta X|$ of 20 cm.

- MUON_CMX18

  This is an extended muon trigger covering the range of $0.8 < |\eta| < 1.0$, using the extended muon chambers of the CMX. The trigger acceptance rate for the CMX18 is 2, 2, and 0.1 Hz for Level 1, 2, and 3 respectively, with a measured efficiency of 96.7 $\pm$ 0.4%.

  - Level 1: A CMX stub with $p_T \geq 6$ GeV/c, along with hits in the central muon wall scintillator extension (CSX) and a COT track with $p_T \geq 8.34$ GeV/c passing through four or more superlayers.
  - Level 2: None.
  - Level 3: A fully reconstructed 3D COT track with $p_T \geq 18$ GeV/c within 10 cm in the r-ϕ plane of the CMX stub.

6.5.2 Datasets

There are several different datasets that can be extracted just from these trigger requirements. We draw from six of them in order to create this analysis.

- EM_NOSI
- EM_CMUP_NOSI

- EM_MU_NOSI_CMXIGNORED
- EM_SI
- EM_CMUP_SI
- EM_MU_SI_CMXIGNORED

Each symbol has a meaning. EM means that the ECAL was active during the run (a requirement for all events for isolation, minimum ionization and other classifications). CMUP means that the CMU and CMP were both in working order. CMXIGNORED refers to early runs in which the noise in the CMX detector rendered it useless. SI and NOSI refer to the operational status of the silicon detector. Good silicon is required for the forward lepton types (PHX and CMIOPES) discussed below.

6.5.3 Track Reconstruction

Tracks are reconstructed in CDF primarily from the COT with well tested reconstruction code. The hits on the wires in each superlayer are assembled into independent track segments. Two separate algorithims are then employed to create 2D axial tracks out of these hits; a segment finding algorithim and a histogram linking algorithim. Both of these algorithims produce tracks which are then merged together.

In order to expand the 2D tracks of the COT into three dimensions, the information from the stereo layers of the tracker are added to the mix. The resulting tracks are then forced to originate from the beamline in the r-ϕ plane in order to improve momentum resolution, before being written out to the datafiles.

COT track efficiency drops to zero outside the practical range of the COT (beyond $|\eta|$ of 1.2). In the forward region up to $|\eta| < 1.5$ we use silicon seeded tracks extrapolated to the COT (IO tracks). A forward calorimeter-seeded track for reconstructing electrons was also used, discussed in chapter 6.5.4.

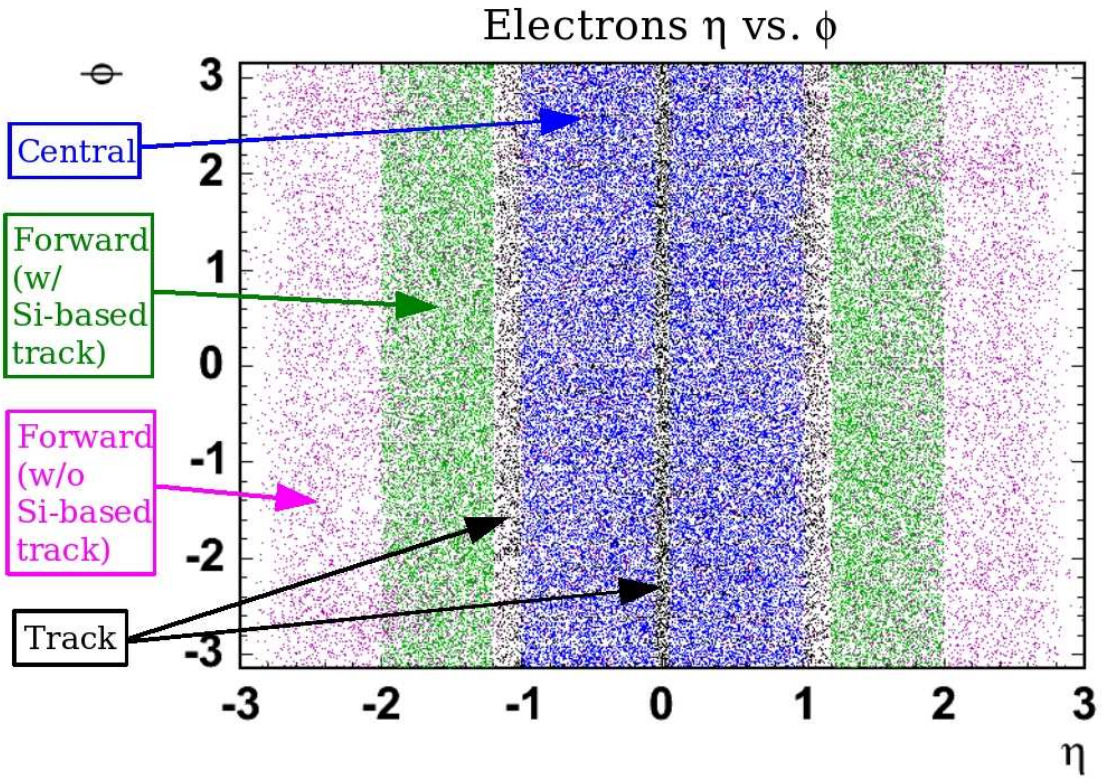

Figure 6.3: Detector coverage of electrons by category, demonstrating the nature and position of each of the categories in this chapter

6.5.4 Electrons

Each lepton category that we use has a set of cuts on various physics quantities in order to remove background. The most prominent sources of background for lepton reconstruction are photons from hadron decays (π^0, η or other mesons decaying into asymmetric e^+e^- pairs before reaching the COT), from charged hadrons from jets, and from the decay of heavy flavor quarks (b,c) into a real lepton (either an electron or a muon). To eliminate these, we have developed a large number of properties which an ideal lepton should possess.

- Conversion: Electrons can be faked by $\gamma \rightarrow e^+e^-$ conversions where one of the electrons has a dominant signature. The conversion-finding algorithim looks for signs of this by looking for the partner lepton, hunting for an opposite sign track that originates from a common point (with an r-ϕ separation $\Delta XY <$ 0.2 cm), and is parallel to the COT track within $\Delta \cot\theta < 0.04$.

  There is the possibility that a real electron might emit a bremsstrahlung photon during its passage through the detector, which might decay in the same way. To avoid this, we look for "trident" events, with a third track (due to $e^{\pm} \rightarrow e^{\pm}\gamma \rightarrow e^{\pm}e^+e^-$) and keep those events.

- Had/Em: High Energy charged hadrons can sometimes look like electrons when they pass through the ECAL. One way to filter them out is to look for relatively high deposits of energy in the HCAL by the same particle, nearly always a sign of hadronic activity. This is the standard measure, the ratio of energy in the HCAL over energy in the ECAL.

- Iso/E_T: Many fakes can come from QCD objects, either mesons decaying in flight or undergoing QCD charge exchange, or heavy quarks decaying to leptons via $q \rightarrow \ell\nu X$. A signature of this is the presence of other particles in close proximity to the possible lepton, due to the shower from the QCD interaction that created the original quark, gluon, or meson. In order to limit contamination from these sources, we require our leptons to be isolated, to have a cut on the energy in a cone of $\Delta R \leq 0.4$ once we have subtracted the energy of the lepton cluster ($E_T^{cluster}$).

- Lshr: The Lateral Shower Profile for EM objects was measured in test beam data [11] for the CEM and CES, and we require our objects to match the same general profile. The L_{shr} profile is properly expressed as:

$$L_{shr} = 0.14 \sum_i \frac{E_j^{adj} - E_i^{expected}}{\sqrt{(0.14\sqrt{E})^2 + (\Delta E_j^{expected})^2}} \tag{6.1}$$

  where:

  - E_j^{adj} is the measured energy in the CES cell.
  - $E_i^{expected}$ is the expected deposit energy.
  - $\Delta E_j^{expected}$ is the uncertainty in the expected deposit energy.

- E/P: Further information on whether a particle is a good lepton can be derived from comparing the momentum of the track with the energy in the calorimeter. Since a tracker has very good resolution on charged particles, these two should agree. However, tracks from jets or other phenomenon deposit energy in the ECAL from sources other then the primary track. The ratio between the cluster E_T and the track p_T serves as a very good benchmark to supress those backgrounds.

- Signed CES Δ x and CES Δ z: It is possible to eliminate some jets and to look for electrons that have emitted large bremsstrahlung radiation by looking for particles with a CES cluster geometrically inconsistent with their track. This is the r-ϕ difference between x and z measured with the track and with the cluster. The symmetry is designed to accept brehmsstrahlung radiation tracks, but reject fake electrons from jets.

- PEM 3x3χ^2: We have measured the forward electromagnetic shower profile in a 3x3 area in test beam data. This is the χ^2 fit result of comparing that with data.

- PES 5x9 U/V: Isolation can be calculated in separate ways. In the forward region covered by the PES, we use the ratio of energy in the central five strips of our PES cluster to the energy in all nine PES strips in order to measure the effective isolation of the lepton we are measuring.

Table 6.1: Selection for TCE Candidates

Quantity	Requirement
Fiducial	Track Fiducial to CES
Track p_T	$p_T \geq 10$: ≥ 5 if $E_T < 20$
Track $\|z_0\|$	$\|z_0\| \leq 60$ cm
NAxSL	≥ 3
NStSL	≥ 2
Conversion	false
Had/Em	$\leq 0.055 + 000045E$
Iso/E_T	≤ 0.1
Lshr	≤ 0.2
E/P	$< 2.5 + 0.015E_T$
Signed CES ΔX	-3 $\leq$ q$\Delta X \leq$ 1.5 cm
CES $\|\Delta Z\|$	$\|\Delta Z\| < 3$ cm
Tracks	BcTrk (Larry's Correction if Data)

Tight Central Electron (TCE)

The Tight Central Electron category is for electrons that impact within the barrel region of the CDF detector, and are one of the easiest and cleanest signatures available at CDF. The characteristics of TCE are given in Table 6.1.

Phoenix Electron (PHX)

Phoenix electrons are electrons that are reconstructed out of the track information in the forward portion of the detector. They use the Phoenix algorithim, which is used to reconstruct possible electron candidates in the forward ($|\eta| >1.2$) region of the detector, beyond the coverage of the COT.

Information from the shower maximum and electromagnetic calorimeter are used to define two points where the particle impacted the calorimeter. This creates two possible tracks dependent on the charge of the particle. After being run through a pattern recognition algorithim that attempts to match the proto-tracks to silicon hits, the best Phoenix track is chosen based on χ^2.

The PHX ID efficiency is actually time dependent, and varies between 79.4 $\pm$ 0.6% and 85.0 $\pm$ 0.5%. The requirements for PHX electrons are listed in Table 6.1.

Table 6.2: Selection for PHX Candidates

Quantity	Requirement
Pes2DEta	$1.2 < \|\eta\| < 2$
Had/Em	≤ 0.05
PEM3x3FitTower	true
PEM3x3χ^2	≤ 10
Pes5x9U	≥ 0.65
Pes5x9V	≥ 0.65
Iso/E_T	≤ 0.1
ΔR(Pes,PEM)	$\Delta R \leq 3.0$
Track Match	true
NSiHits	≥ 3
Track $\|Z_0\|$	$\|Z_0\| \leq 60$ cm

6.5.5 Muons

Muons are identified by a different selection, as they rely upon different components of the detector. Most muons are defined relative to the stubs produced by the muon chambers. As a real muon passes through the muon chambers it creates hits, which can later be assembled into line segments referred to as stubs. Since nothing else should be able to penetrate entirely through the detector, the presence of a stub is generally an indication of a muon.

Muons pass through the detector because of their lack of interactions with the dense materials of the inner layers. A particle of this type is referred to as minimum ionizing, which means that they do not leave large energy deposits inside the ECAL, unlike their electron cousins.

The largest source of fake muons comes from the decay of heavy flavor quarks (b,c) on the beamline that release a muon in the process, and in the in-flight decay of mesons into products involving a muon. Both of these are combated by vertex reconstuction and isolation cuts.

Specific muon cuts are discussed below:

- Iso/p_T: This is the same as in the electron case, except that we use track p_T instead of E_T.

- E_{EM}/E_{HAD}: This is the energy present in the ECAL/HCAL, which con-

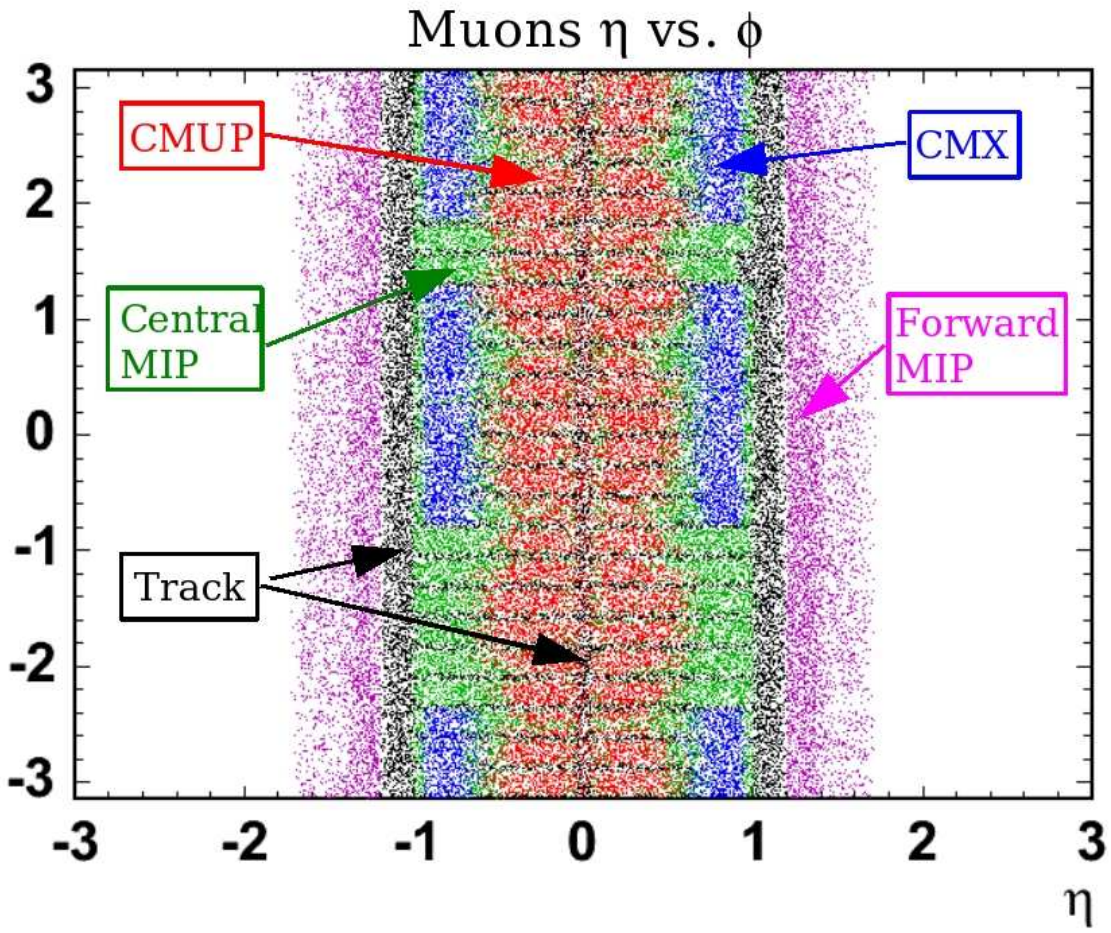

Figure 6.4: Detector coverage of muons by category

strains muon tracks to minimum ionizing particles, and allows us to weed out various hadronic backgrounds.

- Track $|D_0|$: The decay of heavy quarks generally takes place some distance from the collision vertex, as both b and c quarks have a significant flight time (due to the nature of their decay chains). In order to reduce backgrounds from those sources, we can cut on the impact parameter, the closest point of approach that the backwards-extrapolated track makes with the collision vertex.

- ρ_{exit}: This is a variable designed to require the passage of all particles through the entirety of the COT, and is defined as follows:

$$\rho_{COT} = \frac{sign(\eta) z_{COT} - z_0}{tan(\lambda)} \tag{6.2}$$

  where $lambda = \pi/2$ - θ, $\theta = 2tan^{-1}(e^{\eta})$, and z_{COT} is 155 cm, used as the length of the COT.

- NAxL/NStL: In order to guarantee a relatively good muon track, we place requirements on the number of hits in the silicon layer a muon has to go through for tracks reconstructed from silicon hits.

- COT Hit Fraction: For CMIO muons, we can calculate the expected number of hits a muon track should have in the COT by calculating its trajectory. To check for track quality, we require a certain fraction of those hits to be actually present.

CMUP/CMX

Central muons are formed by matching muon stubs to COT tracks. Hits in the chambers of the CMP, CMU, and CMX allow reconstruction software to form line segments tracing the path of the muon through the detector. These line segments are required to match the extrapolated COT track within 3, 5, and 6 cm in the CMU, CMP, and CMX respectively in order to allow for multiple scattering effects. To remove the possibility of other fake particles (such as meson decay in-flight to a real muon), minimum ionization is required in the calorimeters.

Table 6.3: Selection for CMUP and CMX Candidates

Quantity	Requirement
CMU Fid	x-fid $<$ 0 cm: z-fid $<$ 0 cm
CMP Fid	x-fid $<$ 0 cm: z-fid $<$ -3 cm
CMX Fid	x-fid $<$ 0 cm: z-fid $<$ -3 cm
E_{EM}	$\leq$ 2 + max(0,(p-100)*0.0115)
E_{HAD}	$\leq$ 6 + max(0,(p-100)*0.028)
Iso/p_T	$\leq$ 0.1
NAxL (5 hits)	$\geq$ 3
NStL (5 hits)	$\geq$ 2
Track $\lvert Z_0 \rvert$	$\leq$ 60 cm
Track $\lvert D_0 \rvert$	$\leq$ 0.2 cm (0.02cm if NSiHit $>$ 0)
χ^2/dof	$\leq$ 4 (3 if run $\leq$ 186598)
$\lvert \Delta X_{CMU} \rvert$	$\leq$ 7 cm
$\lvert \Delta X_{CMP} \rvert$	$\leq$ 5 cm
$\lvert \Delta X_{CMX} \rvert$	$\leq$ 6 cm
ρ_{exit}	$>$ 140 cm if CMX
CMP veto	No Bluebeam in CMP for run $<$ 154449
CMX veto	No CMX for run $<$ 150144
Arches	Arches only for all run range
	Arches removing wedge 14 on West Side for run $>$ 190697
Tracks	BcTrk (Larry's Correction if Data)

The identification efficiency for the CMX runs from 87.7 $\pm$ 1.7% to 93 $\pm$ 0.1%, for the CMUP from 86 $\pm$ 1% to 92.6 $\pm$ 0.9% with track isolation. The requirements for CMUP/CMX muons are listed together in Table 6.3.

CMIOCES/CMIOPES

The CMIOCES/CMIOPES categories are for stubless muons in the central and forward region. Stubless muons are tracks where the track fulfills the minimum ionizing particle criteria, but either have no muon stub, or one that failed the requirements. The requirements for CMIO leptons are listed in Table 6.4.

Table 6.4: Selection for CMIOCES and CMIOPES Candidates

Quantity	Requirement
E_{EM}	$\leq 2 + \max(0,(\text{p-100})*0.0115)$
E_{HAD}	$\leq 6 + \max(0,(\text{p-100})*0.028)$
Iso/p_T	≤ 0.1
Uniqueness	Not a CMUP or CMX muon
Track $\lvert Z_0 \rvert$	≤ 60 cm
Track $\lvert D_0 \rvert$	≤ 0.2 cm (0.02cm if NSiHit > 0)
$E_{EM} + E_{HAD}$	> 0.1 GeV
Central (CES)	Track CES Fiducial
NAxL (5 hits)	≥ 3
NStL (5 hits)	≥ 3
χ^2/dof	≤ 3
Forward (PES)	Track PES Fiducial
COT Hit Fraction	> 0.6
	No Beam Constraint on IO tracks

6.5.6 Track-based Leptons

As part of an earlier analysis, the UCSD group developed a Track-based lepton category, very similar to the CMIO, but dealing with the numerous cracks in the detector. One of the primary problems with reconstruction at CDF lies in the fact that the detector coverage is both uneven and spotty - numerous "cracks" exist in the detector, leaving gaps in calorimeter coverage.

However, tracker coverage is still relatively thorough, and the UCSD group has been able to leverage that into the Crack Track (CrkTrk) category of leptons. This consists of single isolated tracks that point to regions not covered by the CES or PES. This allows us to pick up leptons that have been lost from normal categories due to gaps in the calorimeter. The nearby sections of the calorimeter are used to search for evidence of a particle shower in the detector consistent with expectation.

CrkTrk leptons are a recent addition to the CDF repertoire, and are not triggerable. They serve as the non-trigger lepton in a dilepton event, and can be counted as either an electron or a muon, as we lack the necessary calorimeter information to determine the type of lepton.

Table 6.5: Selection for Crack Track Candidates

Quantity	Requirement
Iso/p_T	≤ 0.1 using CDF Muon or using nearest CDF EMObj with $\Delta R < 0.05$
Track $\lvert Z_0 \rvert$	≤ 60 cm
Track $\lvert D_0 \rvert$	≤ 0.2 cm (0.02cm if NSiHit > 0)
NAxL (5 hits)	≥ 3
NStL (5 hits)	≥ 3
χ^2/dof	≤ 3
Uniqueness	Not a CMUP or CMX muon
Fiducial	Track not CES or PES fiducial
Conversion	false

6.5.7 Leptons vs. Muons

As seen in Figure 6.3 and in Figure 6.4, the coverage between the electron and muon categories is radically different at CDF. Most of this is a result of factors discussed in Chapter 4. Muon coverage depends either on hits in the tracker, or muon chambers, or both, and coverage of the tracker and muon chambers is limited in high $|\eta|$. Muon chamber coverage terminates at $|\eta| \leq 1.0$, while coverage from the tracker grows sparser at high $|\eta|$ as each track passes through less layers of the tracker as it heads into the endcap. In contrast, electrons have solid ECAL information as far out as $|\eta| = 3.6$ for the PEM giving it much wider, and larger coverage.

The two images also allow direct viewing of the cracks between the various components of the CDF detector. Electrons and muons are both often lost in those cracks, although many of the particles are redeemed by the Crack Track category.

6.6 Jets

Jets tend to be simpler objects then leptons to identify. There is, after all, no such object as a fake jet - as the only thing that could conceivably fake a jet is another jet. In truth, a jet is any object that leaves energy in the detector, and

leptons can be seen as a sub-category of the wider class of jets.

A jet's primary signature is an abundance of tracks in the tracker, as well as energy deposited in both the ECAL, and the HCAL. Jets are primarily composed of low-mass mesons, π^+, π^-, and π^0. Because of their neutrality (they decay to two neutral photons), the π^0 is generally not seen in the tracker, but all three particles leave deposits of energy in the detector. The majority of the jet energy ends up in the HCAL, which acts as a gigantic backstop, preventing all but the tiniest sliver of energy from reaching the outer layers, and thus preventing muon fakes.

Jets are assembled using a fixed cone size and a certain algorithim. Information from the ECAL and HCAL towers is taken into account, and large deposits of energy are identified. The jet algorithim is then used to find the optimal grouping of energy deposits from the calorimeter to make a jet. The simplest possible algorithim simply finds all geometric cones for which the energy inside the cone passes some cutoff, and then eliminates all those cones that intersect other cones of higher energy. The end result will be a collection of jets, each with a transverse energy (E_T), and a direction[14].

Jets used in this analysis were picked from a standard CDF selection. We assembled jets using a cone size of $\Delta R < 0.4$, using the JetClu algorithim[6]. The JetClu algorithim starts with a set of "seed towers", calorimeter towers with an E_T deposit greater then 1 GeV. Towers inside a cone of $\Delta R = 0.4$ are then taken and a center-of-mass is calculated using the tower centroid position, and taking the E_T deposits in each tower as weights. This procedure is carreied out iteratively, with the final goal to have each tower be part of only one jet by splitting towers from one jet and merging them into another. A typical JetClu central jet of this cone size has 15 towers.

The latest level 5 corrections were used to correct the absolute energy scale of the jets, taken from the jetCorr06b tag of the JetUser package. This includes all corrections levels 1-5, as detailed below.

- Level 1: Relative Corrections: Jet Energy Scale uniform in η and across detector components.
- Level 2: Stability corrections: Correct for luminosity and aging effects.

- Level 3: Raw Energy Scaling: Corrects CEM response to match Run I.
- Level 4: Multiple Interactions: Compensates for multiple interactions.
- Level 5: Absolute Energy Scale: Corrects for non-linearity in the calorimeter and detector energy loss using $\sum p_T$ of particles within the cone that match the jet direction with $\Delta R < 0.5$.

We do not correct for either out of cone or underlying event corrections, to match other CDF diboson analyses. Because we do not wish to double count our objects, we veto any jet that is within $\Delta R < 0.4$ of any of our leptons.

Jets have basic kinematic requirements of $E_T \geq 15$ GeV and $|\eta| \leq 2.5$.

Chapter 7

Anomalous Triple Gauge Coupling Searches

7.1 Overview

The first topic covered in this thesis concerns searches for Anomalous Triple Gauge Couplings in the dilepton-dijet channel. The results discussed herein were blessed as two separate analyses by the CDF Run II collaboration, but are closely enough related that they can be discussed as a single analysis.

The purpose of this analysis is to search for production of either ZZ or WZ bosons in a way that exceeds the boundaries of the Standard Model, as discussed in Section 2.9. This provides two separate results. One is a limit on so-called Anomalous Triple Gauge Couplings (aTGCs), which are mathematical terms that can account for a large number of possible effects modifying the direct coupling between ZZZ and WZZ bosons. The second is an absolute cross-section limit on the creation of WZ and ZZ pairs at high p_T beyond the Standard Model prediction, which puts an indirect limit on the production of new particles with high mass that decay favorably to WZ or ZZ.

Systematics for this analysis will be covered in Chapter 8.

This analysis was completed in three stages, all with 1.9 fb^{-1} of integrated luminosity. The data was originally unblinded in summer of 2007 as part of a

Table 7.1: Limits on $Z \rightarrow ZZ$ and $\gamma^* \rightarrow ZZ$ aTGC from LEP II

Coupling	Limit
f_4^Z	(-0.30,0.30)
f_5^Z	(-0.34,0.38)
f_4^γ	(-0.17,0.19)
f_5^γ	(-0.32,0.36)

Table 7.2: Limits on $Z \rightarrow ZZ$ and $\gamma^* \rightarrow ZZ$ aTGC from D0

Coupling	Limit
f_4^Z	(-0.28,0.28)
f_5^Z	(-0.26,0.26)
f_4^γ	(-0.31,0.29)
f_5^γ	(-0.30,0.28)

ZZ aTGC analysis, and was presented for the first time in public. Work on the analysis was carried out throughout the year, until the analysis was finally blessed in June of 2008 with 1.9 fb^{-1} of data and the limits presented in chapter 9 for ZZ anomalous couplings. Further work was done from this point on to use the same data to produce WZ aTGC limits, in concordance with the $WZ \rightarrow \ell\ell\ell\nu$ analysis then being produced by Rami Vanguri of the UCSD group. This result was blessed in September of 2008. The final results are presented combined in this chapter.

7.2 Previous Work

7.2.1 Previous $Z \rightarrow ZZ$ and $\gamma^* \rightarrow ZZ$ aTGC Measurements

Previous work on the $Z \rightarrow ZZ$ and $\gamma^* \rightarrow ZZ$ aTGC channels was carried out both at LEP II [19] and at D0[5]. The limits determined by these previous analyses are displayed in Tables 7.1 and 7.2.

7.2.2 Previous $W \rightarrow WZ$ aTGC Measurements

7.3 Event Selection

The fundamental task of any High-Energy Physics experiment is to separate the events you want, the signal, from the background. In a hadron collider environment, the background is large and multi-varied, and it can become exceedingly difficult to separate a small signal from the large background. This is especially true of a channel requiring jets as jets are a large part of the underlying event at a hadron collider.

To do this, we are given two handles. We must separate dilepton and dijet pairs that come from W and Z bosons from those that arise from Standard Model background sources, and we must then find traits that separate aTGC events from their Standard Model cousins - as well as the background that makes a dilepton-dijet mode unfavorable.

Our strategy here is not to cut background down to zero. We recognize that the Monte Carlo models of this region of Drell-Yan and diboson phase space are not well verified with respect to data. In order to compensate for possible excesses in background production we plan to use fitting, comparing our signal to background and signal templates, to determine the statistical significance of our results, instead of just counting events.

7.3.1 W and Z properties

The W and the Z boson were first discovered by the UA1 and UA2 experiments on the SPS in the 1980s in an act that eventually resulted in the 1984 Nobel Prize in Physics. Their properties were, at the start of CDF Run II relatively well known.

The Z has two decay channels we are interested in; Z to leptons ($Z \rightarrow e\bar{e}$ and $Z \rightarrow \mu\bar{\mu}$, and Z to jets ($Z \rightarrow q\bar{q}$). Because of the better performance of our lepton ID and selection, the leptonic channel gives us much more precise information on the state of the particle before the decay then the dijet channel. We use this in both searches to limit the contribution of background.

Background for a dilepton-dijet search comes primarily from QCD events, where two jets decay leptonically, thus creating a false dilepton signature, and two associated jets. The vast majority of these events are removed by the lepton selection, which guards against QCD fakes as previously described. However, those leptons which pass tend to be both low p_T and arranged randomly in the detector. We can limit the contribution of these background events by forcing the lepton pair to resemble a Z.

A Z boson has a mass of 91.19 GeV/c^2, and a narrow width of 2.5 GeV/c^2 [10], which gives a very distinct signature. Experimentally, this width is enhanced by the non-ideal resolution of the detector, which results in a relatively wide peak compared to the theoretical ideal, but still very narrow compared to the background. We use this to set a Z-window, only looking at events where the dilepton mass is within a range of 76 to 106 GeV/c^2.

This has the effect of greatly reducing the contamination from $Z \rightarrow \tau\tau$ backgrounds, already reduced by 90% due to branching fractions alone, as shown in figure [**?**]. QCD leptons, which tend to have an extremely random dilepton mass, tend to fall outside the Z-window as well.

The W has only one channel we are interested in, $W \rightarrow q\bar{q}$, which is very similar to the $Z \rightarrow q\bar{q}$ channel. Because of this, we treat this channel in a very similar way in both analyses.

With the majority of QCD background eliminated first by the lepton ID, and the remainder by using the Z-window, we are left with a background dominated by Z + Jets, where the dominant force is dealing with a Z produced in conjunction with two QCD jets. The two jets have a broad spectrum (like the leptons would have), and the Z decaying to two leptons is exactly identical to our Z.

In order to eliminate the QCD jets of this background we can fit our data to templates representing both the likeliest mass shape of a W or Z boson, and that representing QCD background. This way we can evaluate, for each event, the probability of that event being either a W or Z.

However, this still leaves us far too many background events. To eliminate them, we have to look at the kinematic properties of the aTGC events themselves.

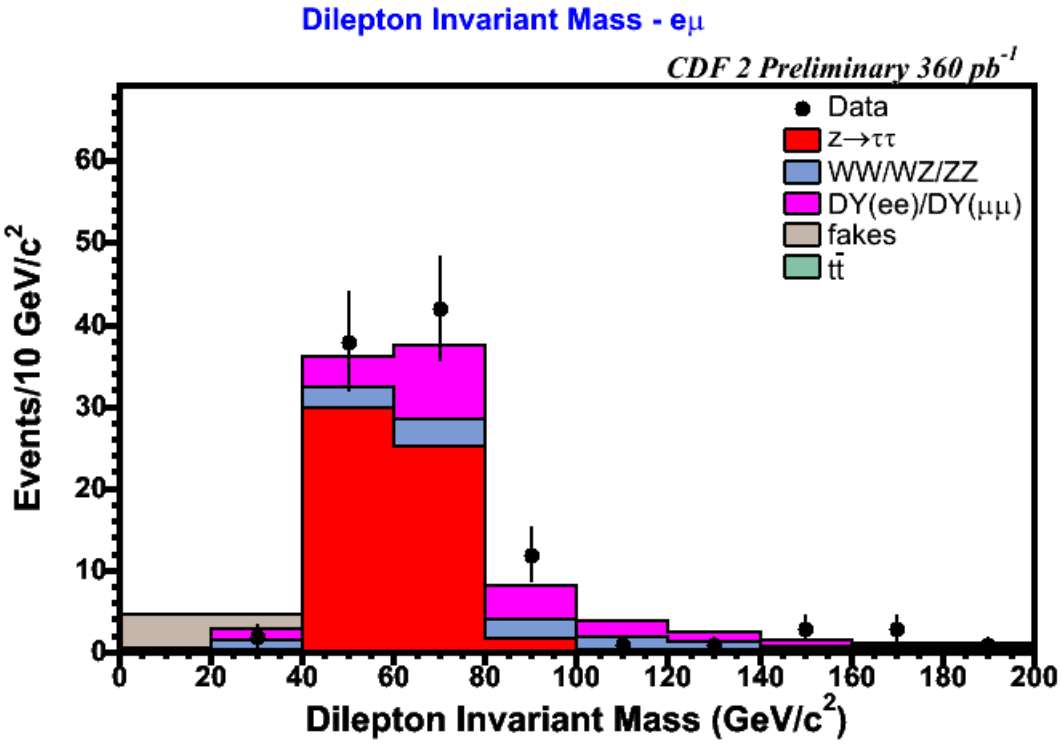

Figure 7.1: $M_{e\mu}$ for the Z system as measured in [17], showing the wide mass spectrum in the high-purity $e\mu$ channel. This figure can be compared with the results from this analysis in Figure 9.1

7.3.2 aTGC Properties and Binning

Anomalous Triple Gauge Couplings have several interesting properties, but only one is really of interest in this analysis; aTGC events tend to be produced at relatively high $\hat{s}$ with respect to Standard Model events or backgrounds. This high center of mass energy allows for the possibility of extremely high momenta in the resulting dibosons.

Due to the PDFs of proton collisions at 1.96 TeV, the p_T spectrum of Drell-Yan background events at the Tevatron is extremely peaked at the low end, and most events are predominately low p_T. Likewise, the spectrum for SM WZ and ZZ production shares the same characteristics; events that appear only at low p_T. However, the high $\hat{s}$ of aTGC events make them dominant at much higher p_T.

Because of the nature of the detector, lepton information becomes much more accurate then jet information. Hence we can apply a background elimination cut by only looking at events at high dilepton p_T, caused by high p_T of the Z. This eliminates most of our background with minimal cost to signal.

We made the decision to limit our search to three bins in dilepton p_T as described in Table 7.3. These bins were selected based on a simple likelihood optimization as to which bin size would give us the best result in searching for a signal equivalent to the f_4^Z limit from the LEP II combined results. Signal bin sizes were allowed to vary in mutliples of 10 GeV/c in dilepton p_T.

Our ability to model our physical data well with Monte Carlo will be determined by extensive tests in the Control Region, the region with p_{Tll} between 105 and 140 GeV/c. This region dominated by background, but it already lies in the tail of the Drell-Yan dilepton p_T distribution, and proves valuable to evaluating our ability to predict the shape of that distribution.

7.3.3 Full Selection

Our event selection requirements can then be summed up in Table 7.4.

The purpose of this selection is to identify all events that will pass the CDF trigger and fulfill the minimum requirements we can establish to be a candidate event. Because this analysis will depend on fitting we establish a loose selection

Table 7.3: Bin properties

Bin	Dilepton p_T	Description
Control Region	$105 < p_{Tll} < 140$ GeV/c	Used for comparing data with MC prediction.
Medium Bin	$140 < p_{Tll} < 210$ GeV/c	Mixed signal and background.
High Bin	$p_{Tll} > 210$ GeV/c	Dominated by Signal

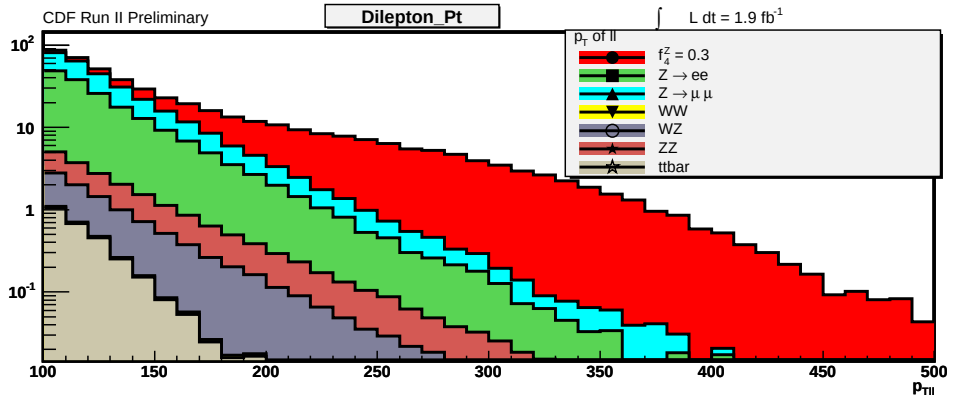

Figure 7.2: p_{Tll} distribution in MC for various backgrounds and aTGC signal for ZZ final state, normalized to 1.9 fb^{-1} expected yield.

Table 7.4: Event Selection for WZ/ZZ aTGC analysis

Requirement	Value
Trigger Lepton	
p_T	20 GeV/c
Lepton Type	TCE, CMUP, CMX
Non-Trigger Lepton	
p_T	10 GeV/c
Lepton Type	TCE, CMUP, CMX, PHX, CMIOCES, CMIOPES, CrkTrk
Jets	
N_{Jets}	$N_{Jets} \geq 2$
E_T	15 GeV
$\|\eta\|$	$\|\eta\| \leq 2.5$
Isolation	$\Delta R \geq 0.4$ from nearest lepton.
Dilepton	
Mass	$76 < M_{ll} < 106$

here in order to provide statistical power to our fitting procedure in the tail regions, and plan to isolate our signal based on the shape of the dijet mass distribution.

Given the relative looseness of our selection, our analysis has now taken shape. We will discriminate signal from background using the dijet mass shape, and use fitting to obtain relative likeihoods of signal and background.

7.4 Analysis Strategy

Our analysis strategy is simple: $WZ \rightarrow \ell\ell jj$

- Use fully-simulated MC to develop templates showing the shapes of signal and background in dijet mass.
- Develop a resolution and efficiency function to enable us to turn MC into yields for every aTGC point in each of our dilepton p_T bins.
- Create a test statistic that enables us to differentiate between signal events and background events. This statistic must avoid dependence on background normalization.
- Generate thousands of simple MC jobs to get a distribution for the test statistic for signal and background.
- Compare this distribution to one that comes from a Standard Model (no aTGC) point as a means of calculating probabilities.
- Compare with data to establish limits.

We must then accomplish the following goals:

- Use fully-simulated MC to develop dijet mass templates.
- Create a Universal Efficiency Function (UEF) which will allow us to transform generator MC into expected yields.
- Decide upon a well-behaved test statistic, and then generate distributions of it for prominent aTGC points.

- Deal with WZ/ZZ crossfeed contamination.

Our major challenges lie in the unpredictable behavior of signal and background in the high $\hat{s}$ region. From previous analyses in this region, we already know that there are inaccuracies in PYTHIA when it predicts the cross-section for Z + jets events, so our fit must "float", depending only on the shape of the background distribution, and not the actual cross-section prediction from PYTHIA. Additionally, we have to show that our signal shape is not dependent on aTGC, that we can treat every aTGC as having the same shape. If this is not true, then we will have to create separate templates for each coupling, and each combined coupling, and the analysis will bog down in minutae and be unreasonably CPU dependent.

We will discuss each of these problems in upcoming sections.

7.5 Generators

Before we can fully enter the period of planning our analysis, we first must have some way to understand the models we are proposing to test. In HEP, this is done through MC simulation. MC generators are produced by theorists, who equip each MC generator to produce a set of events according to a theory they have developed. These generators are then used to produce individual events and full kinematic distributions for any of the physics they contain.

Generators deal with several different steps of the simulation process. We deal with two different types of generators here. All generators are capable of doing "hard-scatter" calculations, creating a specific set of particles and decay products. PYTHIA[31], Baur[12], and MCFM[16] are all capable of this. In our case we use them to create our most essential particles; $ZZ \rightarrow \ell\ell jj$ for example.

PYTHIA provides extra functionality. It is capable of doing the other tasks of a generator, creating the extra particles that come about from colliding two protons, forcing them to undergo hadronization, and then decaying them into their final products. All of these steps are necessary to actually simulate the physics of a particle collider, so we feed hard scatter results from other MC Generators through PYTHIA in order to produce accurate results.

We use three different generators in the course of this analysis.

7.5.1 PYTHIA

PYTHIA[31] is a standard physics generator used not just by CDF, but by a great many modern particle physics experiments, including CDF's successors, CMS and ATLAS. A descendent of an older program known as JETSET[30], PYTHIA serves to accurately model multi-particle production from hard scatter collisions at all high energy colliders. CDF uses the 6 series PYTHIA generator, which is coded in FORTRAN 77.

For CDF, PYTHIA serves in a dual role. First, it can generate events out of hard scatter collisions like most other generators, and was used in this analysis to generate the Z + jets background sample. In this mode it uses basic models to create a distribution of particles that emerge from the hard scatter.

In the second role, PYTHIA exists to do both fragmentation and showering of existing particles. The hard scatter particles generated either by PYTHIA or by another generator, are sent through another process in PYTHIA where they undergo the fragmentation that they would normally undergo before entering the detector. In this mode PYTHIA strives to generate an accurate depiction of the formation of jets and other QCD background objects from the initial $p\bar{p}$ collision. This step is necessary to accurately simulate what a real event will look like inside the detector.

7.5.2 Baur

The "Baur generator" is a generator developed by U. Baur and D. Rainwater in order to do a large number of electroweak simulations described in [12]. It comes in several different packages, of which one is a leading-order generator for ZZZ and ZZγ aTGC. This is, to our knowledge, the only generator for these anomalous couplings.

Output from the Baur generator can be transformed from the raw text given at output to the common LesHouches format described in [9]. This allows the output

to be fed into PYTHIA to undergo fragmentation and from there to be placed through the full CDF GEANT based simulation. During this process, some changes were made to the generator information. The Baur generator only produces one type of final state, requiring both a particular flavor of lepton and a particular flavor of final-state quark. It also omits all information on the initial state parton, which is required in order for the event to undergo PYTHIA fragmentation.

To overcome this we produced multiple samples for each aTGC point we generated, restricting the generator to a single initial state parton in order to know what particle generated the collision, and producing separate final states for both up and down type quarks to satisfy the differences in the (c_v - c_a) structure of the Z boson. We randomized the lepton flavor and the color of the quarks, and made the assumption that out of the proton, only up, down, and strange type quarks make a significant contribution to final production (this assumption was verified by cross-section analysis as in Table 7.5).

The Baur generator for ZZ aTGC had not been previously used at CDF. This forced us to do a number of comparison checks. We compared the generator-level Z-mass templates to those provided by PYTHIA for our preliminary check, and then compared a sample of the Standard Model ZZ fully produced via the CDF GEANT simulation to one created entirely by PYTHIA, and found that they matched to our satisfaction.

One of the faults discovered was that the Baur generator does not appear to adequately reproduce the basic gluon showering model from PYTHIA, thus preventing Baur from accurately forming the ZZ center of mass p_T (Figure 7.3). This had to be corrected in the generator level MC before the final yields could be calculated. We eliminate this problem by using a histograms of the ZZ p_T from the Pythia sample, at generator level, to boost the ZZ system in Baur. A random number is selected according to the distribution of the Pythia ZZ p_T, which is then applied as a boost to the Baur MC. We take a selection of histograms for different ranges of ZZ Mass, on the basis that the p_T available for the ZZ system should be somewhat dependent on the overall mass. Mass ranges are from 0 to 200, 200-300, 300-400, 400-600, and 600+ GeV of M_{ZZ}.

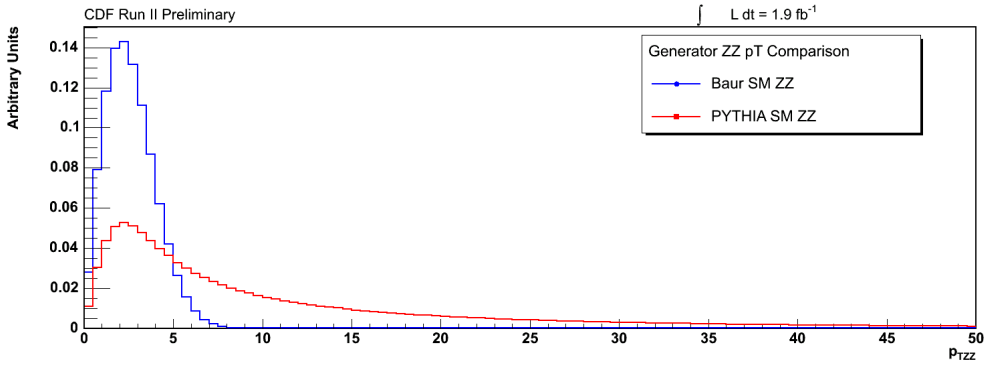

Figure 7.3: p_T of the ZZ system for Pythia and Baur before correction

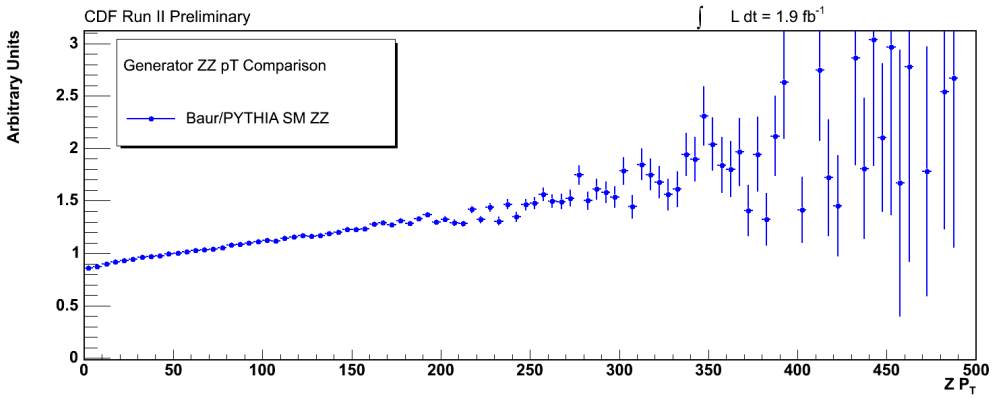

Figure 7.4: Ratio of p_T of the ZZ system for Pythia and Baur before correction

The result of boosting a LO Baur MC distribution by this method is compared with the original Pythia ZZ p_T distribution in Figure 7.5.

NLO in Baur

Because the Baur generator does not have an NLO option, we were forced to come up with several different methods for obtaining an NLO cross-section from the generator. One was to use the k-Factor correction used by the ZZ or WZ analyses, but this was ruled unfavorable, as the ZZ NLO factor is based on t-diagram loops, and the ZZ aTGC NLO factor would be based primarily on s-

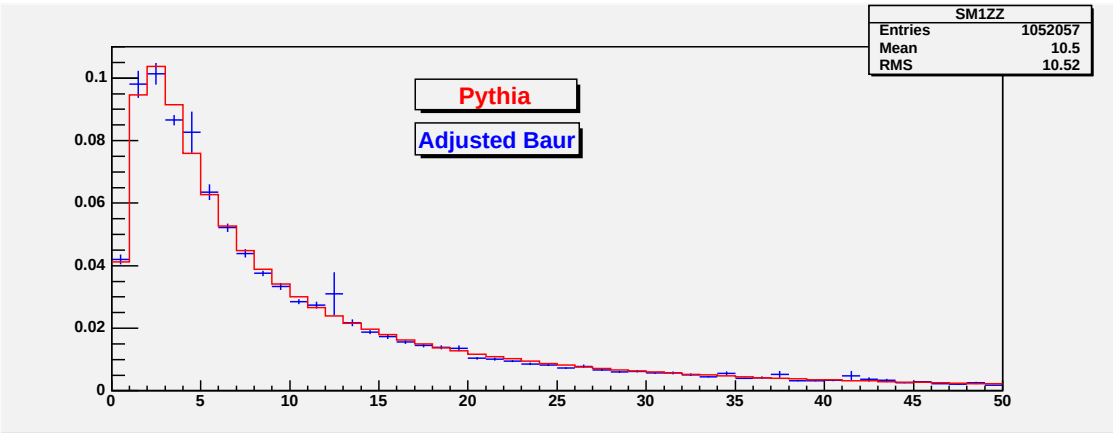

Figure 7.5: p_T of the ZZ system for Pythia and Baur after correction

Table 7.5: Cross-Section for different quark types in Baur MC

Quark	Cross-Section $f_4^Z = 0.3$
b	0.163E-05
c	0.427E-05
s	0.320E-04
u	0.540E-02
d	0.128E-02

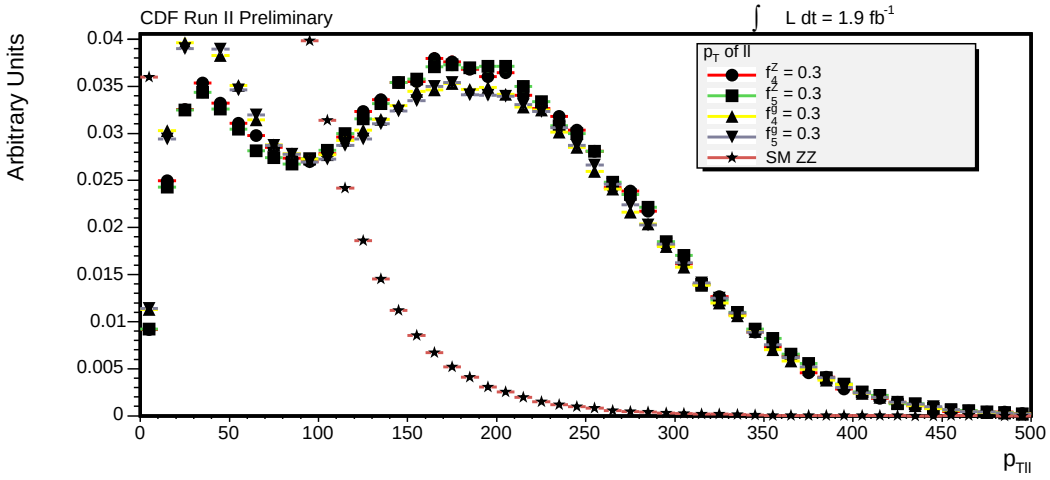

Figure 7.6: Reconstructed Dilepton p_T distribution for aTGC samples, normalized to unit area

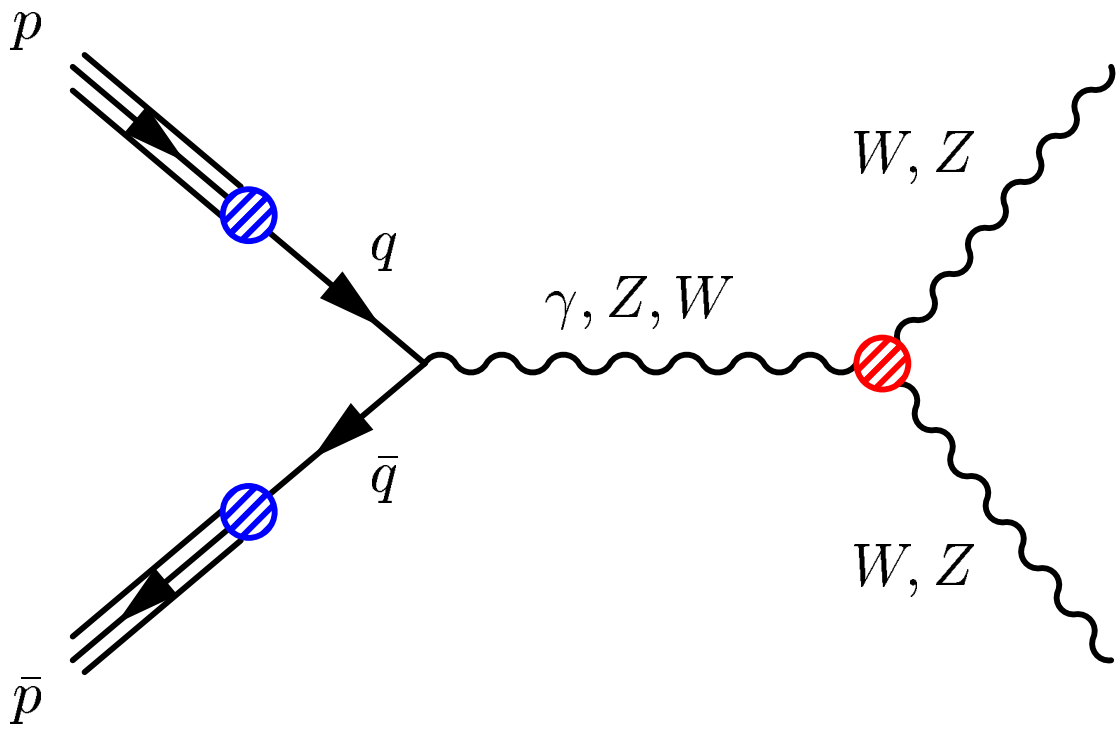

Figure 7.7: Generic s-channel production of diboson final states. This diagram covers both the production of the ZZ and $Z\gamma$ final state.

diagram loops. Another was to use the s-channel factor from the DY samples, although the smaller mass made this somewhat questionable.

In the end, we settled on a compromise solution offered by Baur in private communication, using the results of an NLO experiment on the similar $Z \to Z\gamma$ channel. Because this channel has many similarities to the $Z \to ZZ$ channel, the NLO corrections should be very similar (Figure 7.5.2). The NLO correction for $Z \to Z\gamma$ has a range that is partially $\hat{s}$ dependent. We picked the more conservative lower end of the range, and settled on a straight k-factor of 1.2 for NLO corrections.

Factorization Scale in Baur

The Baur MC, by default, uses a factorization scale based on a constant value, M_Z^2. This scale is different from the one adopted by default for PYTHIA in CDF, which is based on $\hat{s}$. A result of this is a discrepency between PYTHIA and Baur when it comes to the center of mass p_T for the whole ZZ system. This is further

addressed by a systematic correction applied to the final results in section 8.4.2.

7.5.3 MCFM

The Monte Carlo for FeMtobarn processes generator, better known as MCFM, is a generator for various femtobarn level (i.e., non QCD processes) at hadron-hadron colliders. Unlike the Baur generator described in section 7.5.2, it is an NLO generator, computing the distribution of final state particles based on all first-order diagrams. It is also a familiar generator to those who work at CDF, and has been used on analyses before.

MCFM computes the aTGC couplings for WZ production, and was used in the $WZ \to \ell\ell\ell\nu$ analysis, making it the logical choice for us to use for our $WZ \to \ell\ell jj$ analysis. However, MCFM does not produce WZ events in the final state we require. To account for this, a simple code was written to transform the W products from a lepton-neutrino pair to a pair of quarks, using the V-A coupling of the W to compare the two, with the quark pairs and colors chosen randomly. This transformation assumed that the V_{ud} and V_{cs} terms of the CKM matrix were dominant. Since we do not use b-tagging in this analysis, contributions from other quarks were expected to have no effect on the final result.

7.5.4 Templates

CDF produces a wide variety of Monte Carlo samples for Standard Model channels and backgrounds. However, the high $\hat{s}$ region in which we choose to operate in this analysis is beyond the reach of most of those samples. This forced us to generate our own Monte Carlo using the CDF engine in order to create proper signal and background templates.

Background

The primary background (in effect, the only background) for this analysis comes from Drell-Yan, where the Z goes either to two muons or two electrons, and there are two associated jets. There is a standard CDF MC background set for this

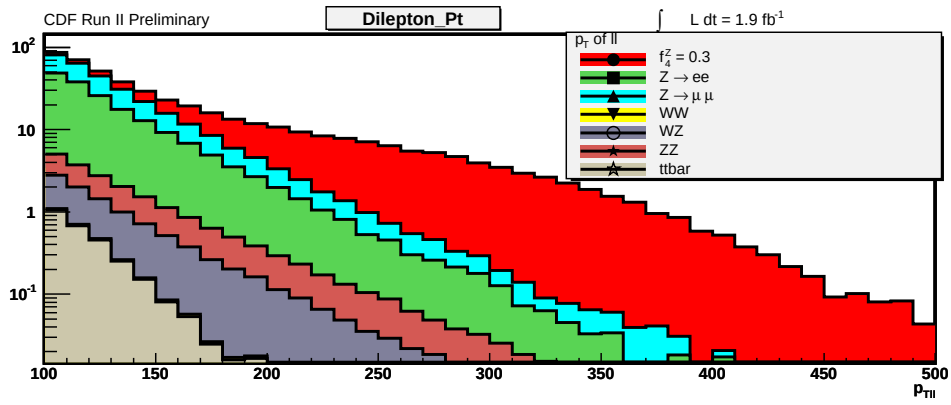

Figure 7.8: Background and Signal comparison as a function of Z p_T for $f_4^Z = 0.3$

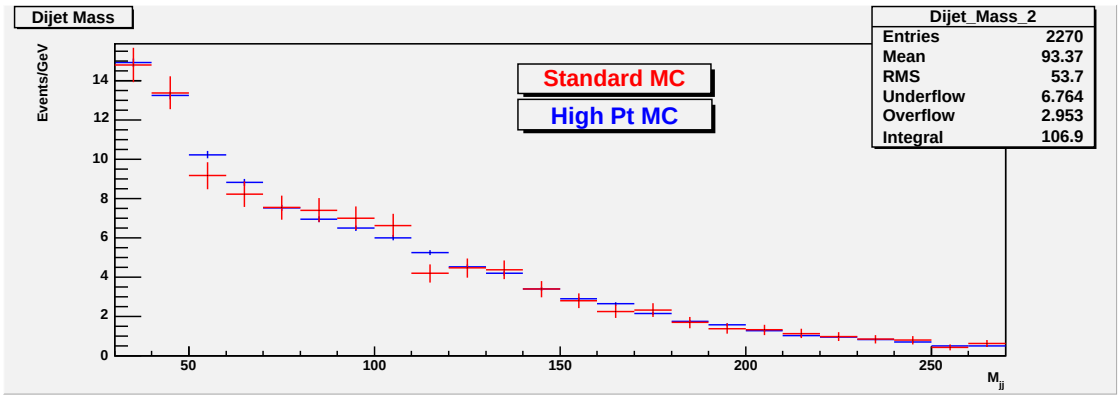

Figure 7.9: M_{jj} comparison between standard MC (red) and our High p_T Drell-Yan sample (blue) for dilepton p_T between 140 and 210 GeV.

channel, but because it was generated as a Standard Model background, most of its events are concentrated at low p_T, leaving very low statistics for a high p_T analysis. In order to get an accurate shape of background at high p_T, we generated our own template.

In this template we generated events in the Z inclusive channel. To that we added a generator-level filter that required at least two leptons in the final state, and a dilepton $p_T > 100$ GeV/c. This allowed us to produce a relatively large sample of the events that we were interested in. A comparison between the high p_T sample and the original CDF sample is provided in Figure 7.9.

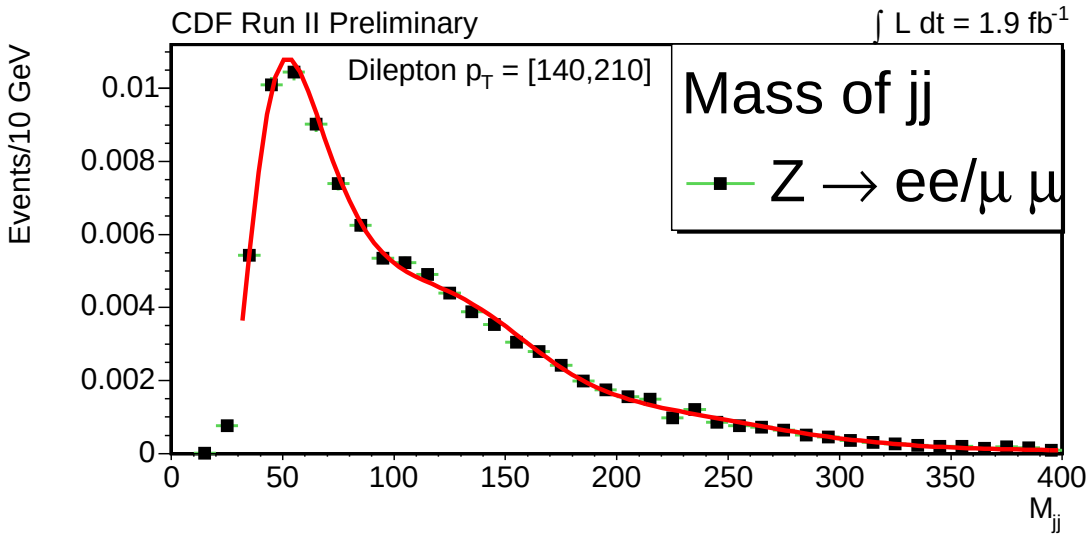

Figure 7.10: M_{jj} distribution for Z+jets background and Z-pT within 140−210GeV in Monte Carlo simulation results.

Templates were produced by fitting the resulting dijet mass shape in each bin to several different fit functions and picking the most appropriate final fit. The templates finally chosen can be seen below in Figures 7.10 and 7.11.

Signal

Signal in this case consists of all production of WZ or ZZ events in the stated bins. This theoretically would allow us to measure the WZ or ZZ Standard Model cross-section with the assistance of extra data.

We generate signal templates by fully generating MC featuring aTGC points. Four aTGC points, at approximately the limits set by the LEP II search, were generated for $ZZ \to \ell\ell jj$, and three aTGC points were generated for the $WZ \to \ell\ell jj$ search at limits chosen to match the production for the UCSD $WZ \to \ell\ell\ell\nu$ analysis. ZZ events were generated by using the Baur MC, and then feeding the resulting events into PYTHIA in order to correctly fragment them. WZ events were produced in the same way using MCFM. The combined result was run through the full GEANT-based MC of the CDF Simulator. This gives a fairly accurate picture of what events look like after being seen by the entire detector.

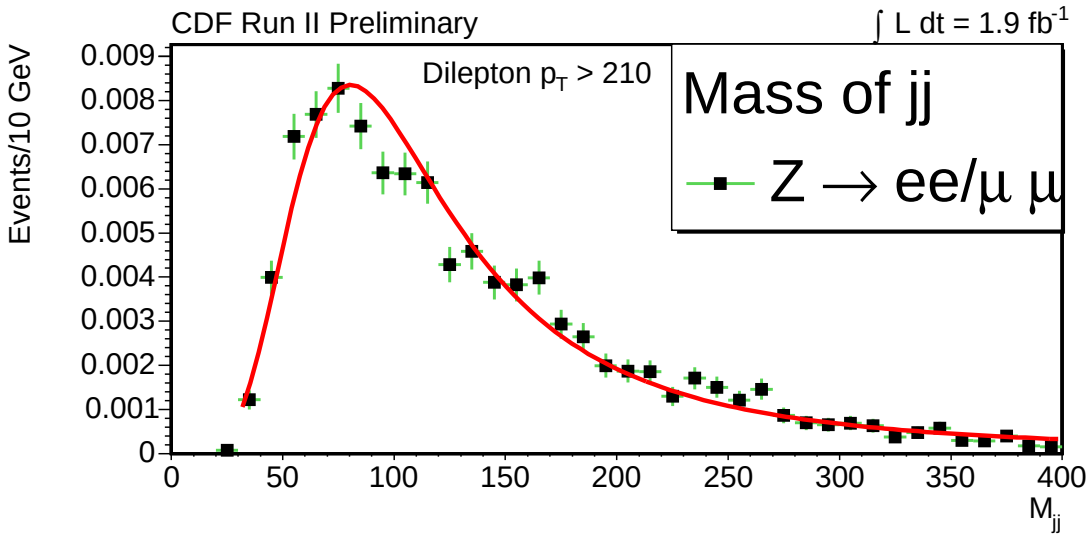

Figure 7.11: M_{jj} distribution for Z+jets background and Z-pT greater than 210GeV in Monte Carlo simulation results.

For our analysis strategy to be valid, we must also ascertain whether or not the shape of the Z-mass peak is the same regardless of the anomalous coupling involved. If the mass shape is a function of aTGC, then we must come up with a separate method to measure each aTGC. Plots were made to compare the shape of the M_{jj} distribution from each aTGC, and a conclusion was reached that the difference between aTGC signal shapes due to different couplings is negligible. These plots are provided in Figures 7.12, 7.13, and 7.14.

From these events, we apply our selection and produce a set of dijet mass distributions for the different aTGCs. Those are used together to create a dijet mass template for all samples in both bins. Two templates exist for ZZ (Figure 7.15 and 7.16) and two for WZ (Figure 7.17 and 7.18).

We also are aware that there are slight variations between the different aTGC points in terms of the dilepton p_T distribution. Obviously, since we have two different functions for the two different signal p_T bins, there are differences between the dijet mass shape at different values of dilepton p_T. Smaller differences, the differences in the dilepton p_T distribution within each bin, can also cause minor variations in the shape.

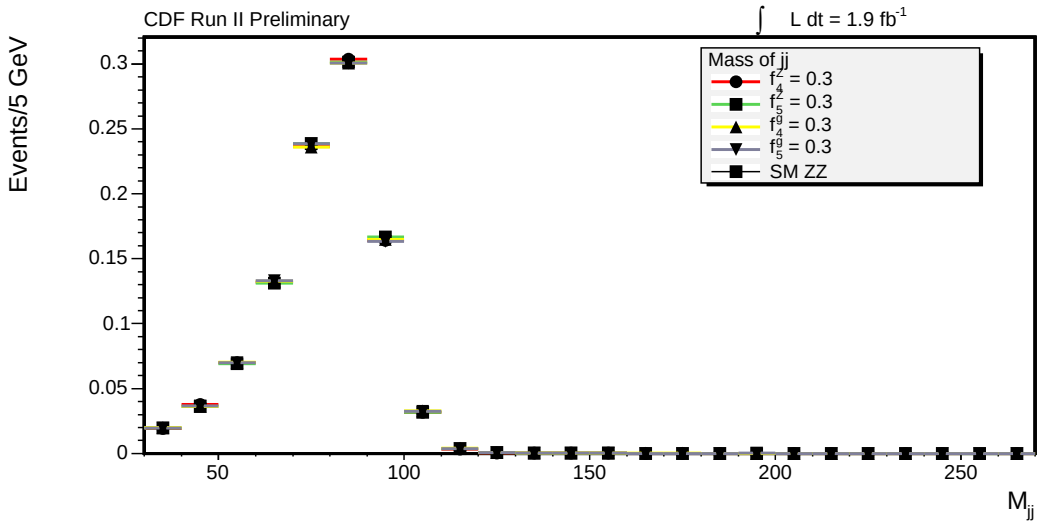

Figure 7.12: M_{jj} for ZZ in all bins for several aTGC values

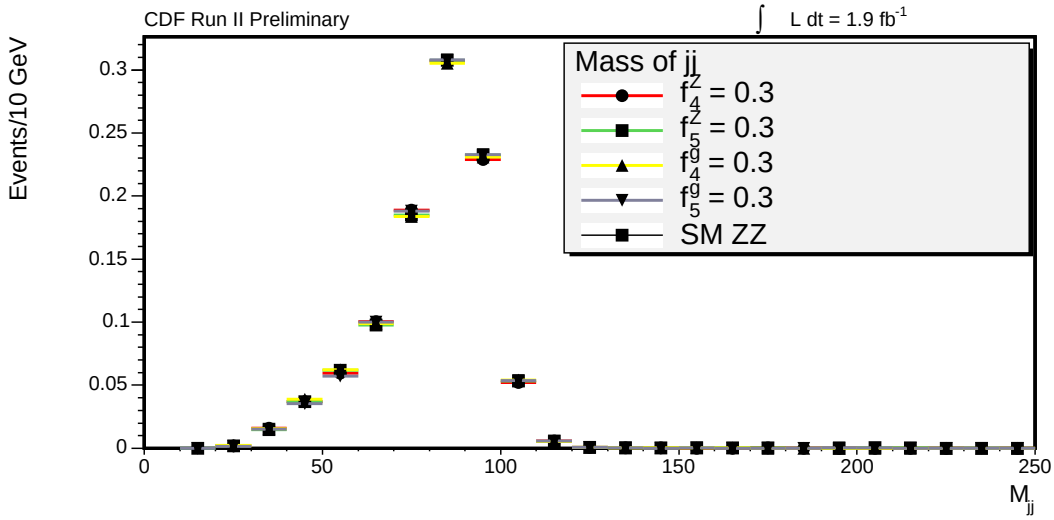

Figure 7.13: Reconstructed M_{jj} distribution for ZZ aTGC samples with p_T between 140 and 210 GeV

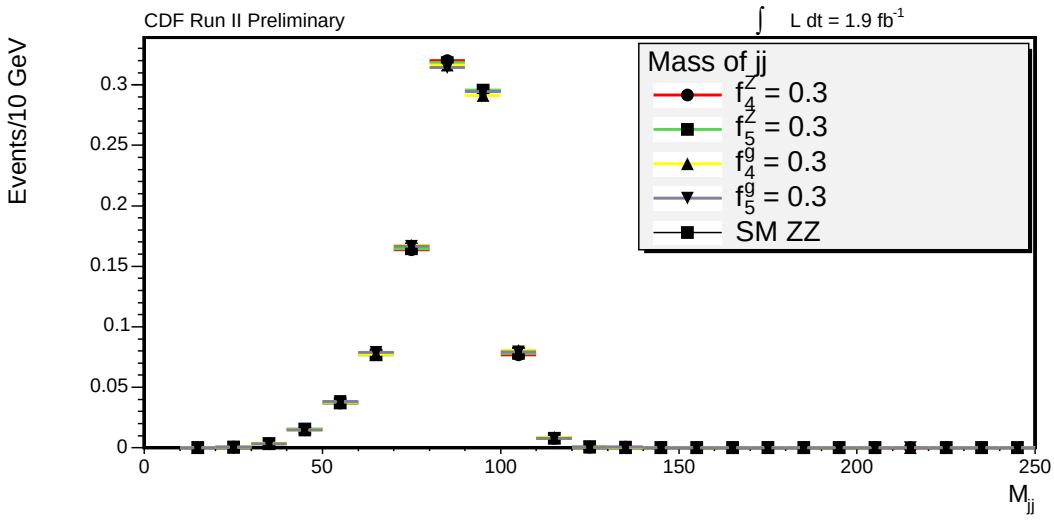

Figure 7.14: Reconstructed M_{jj} distribution for ZZ aTGC samples with p_T above 210 GeV

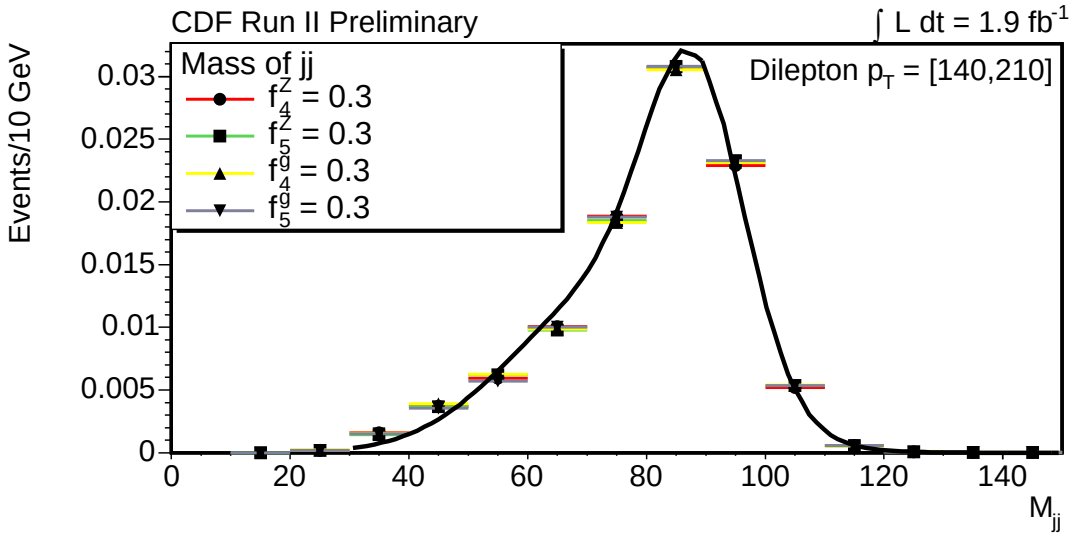

Figure 7.15: ZZ M_{jj} distribution for signal and Z pT within $140 - 210$GeV

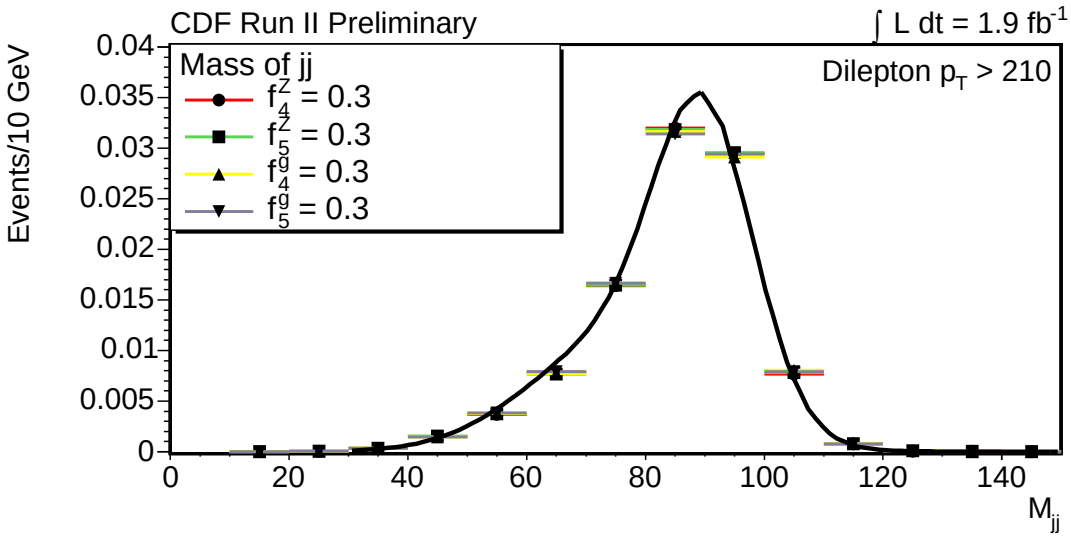

Figure 7.16: ZZ M_{jj} distribution for signal and Z pT greater than 210GeV.

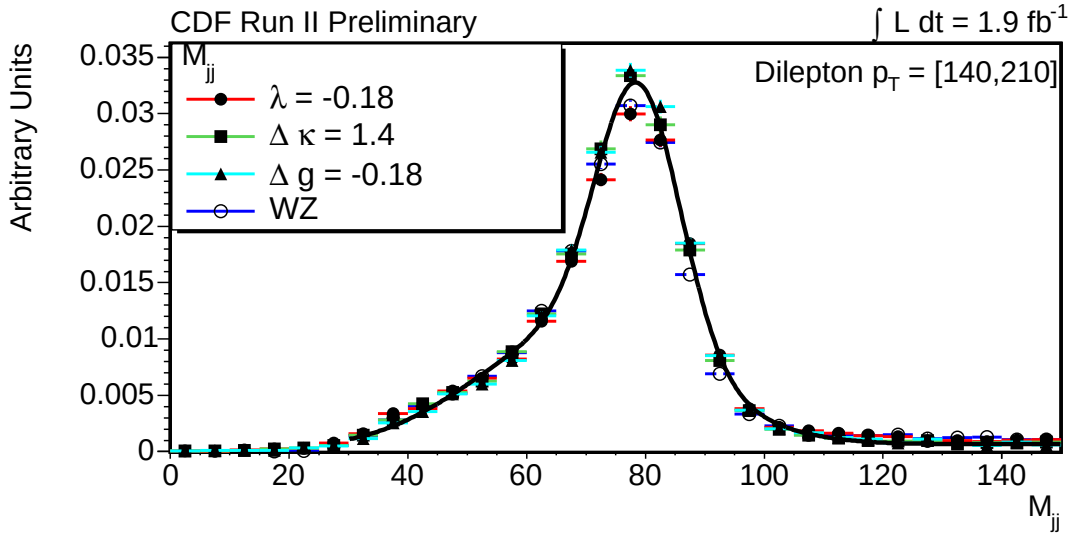

Figure 7.17: WZ M_{jj} distribution for signal and Z pT within $140 - 210$GeV

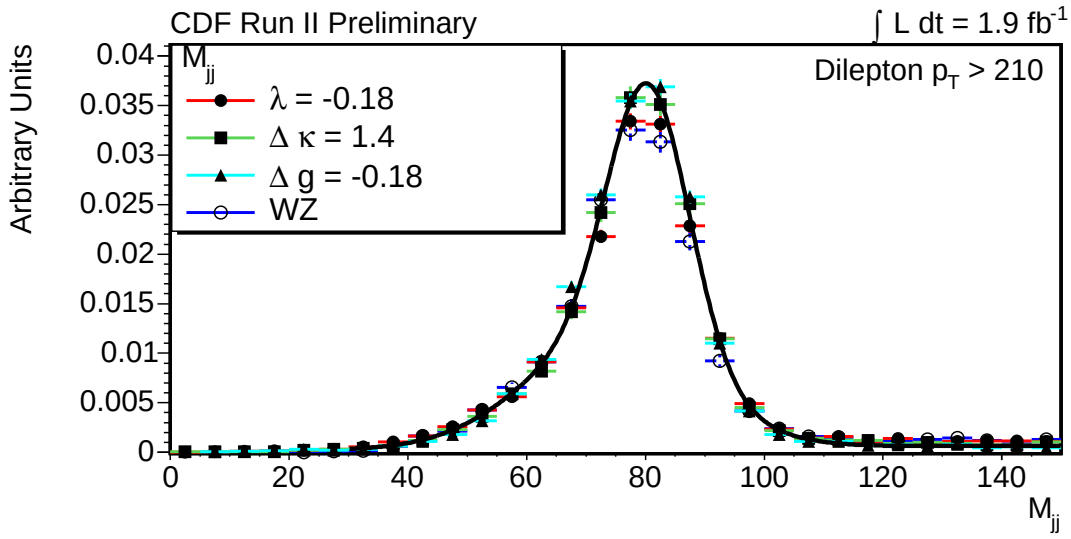

Figure 7.18: WZ M_{jj} distribution for signal and Z pT greater than 210GeV.

A comparison is given for the WZ aTGC points in Table 7.6 showing the breakdown of the WZ aTGC signal MC points into smaller brackets to illustrate the difference between them. This effect, although noticeable, was ruled to be subordinate to the similar Jet Resolution systematic, discussed in Chapter 8.2.1.

7.5.5 Universal Efficiency Function (UEF)

The signal MC mentioned in section 7.5.4 is used to determine what we term the Universal Efficiency Function. According to a simple view of the decays involved, we hypothesize that a ZZ or WZ system decaying with a certain dilepton p_T will be seen by the detector, on average, as the same regardless of which aTGC it came from. If this is true we can make a simple curve as a function of dilepton p_T that can be used to turn generator distributions of dilepton p_T into expected yields in the actual detector.

This is done by comparing the output of the signal MC, which represents the number of events that have passed all of our cuts inside the detector, after reconstruction, with the original distribution at generator-level, as a function of dilepton p_T. In other words, we divide the dilepton p_T distribution that survives the de-

Table 7.6: WZ aTGC MC by p_T

p_T	NEvents	Mean	RMS
$\Delta\kappa$			
(140,180)	9111	73.9	14.49
(180,210)	4517	74.64	12.98
(210,260)	3611	77.4	11.86
(260,310)	1657	78.71	10.3
(310,∞)	907	80.01	11.18
Δg			
(140,180)	13367	74.09	14.16
(180,210)	6822	75.84	12.74
(210,260)	6161	77.49	11.37
(260,310)	4748	78.45	9.55
(310, ∞)	1878	79.33	10.96
λ			
(140,180)	10607	73.64	15.42
(180,210)	6350	75.55	13.68
(210,260)	5292	77.03	13.04
(260,310)	2667	77.89	11.36
(310, ∞)	2706	79.36	11.58

tector by the distribution that went into the detector to get a function that maps how well the detector actually captures events.

This UEF can then be applied directly to dilepton p_T distributions created by the Baur or MCFM generators in order to produce an expected yield of events in data. This is important because the process of more accurately simulating this using the full GEANT-based simulation is time consuming, and gobbles huge amounts of CPU power that are not necessarily available to us in this experiment.

We produce two UEFs, one for ZZ (Figure 7.19) and one for WZ (Figure 7.20). The curve itself is built by averaging together the aTGC points, and is compared to the Standard Model production in order to establish a sense of correctness.

The UEFs both experience a drop-off at high dilepton p_T. This can be explained through the dilepton requirements. As the p_T of the dilepton system gets higher, the resulting pair of leptons gets closer together. At a certain point, we began to see more and more leptons within a ΔR of 0.4 of each other, the size of our lepton isolation cone. Since we require there to be no major objects within our

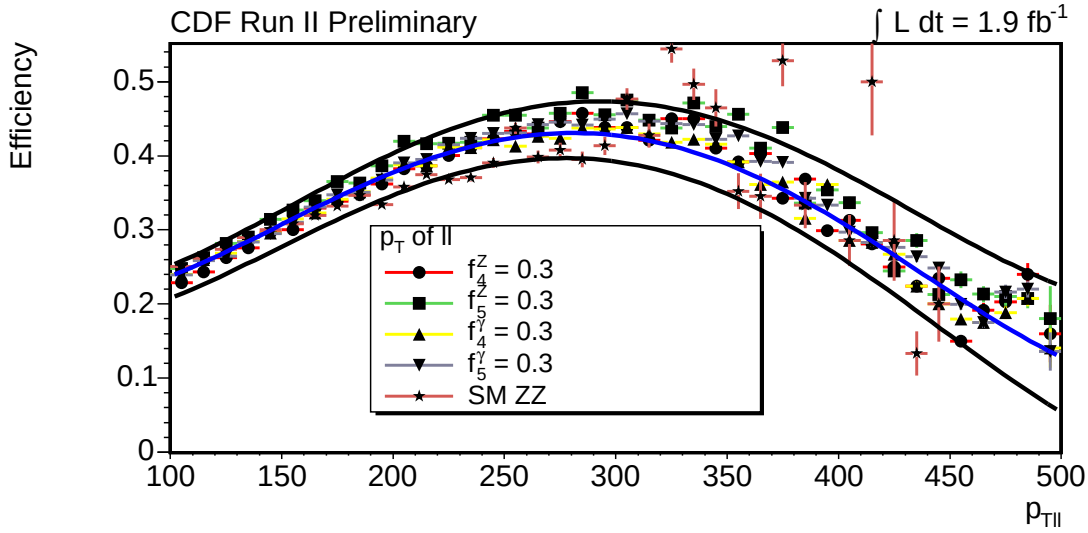

Figure 7.19: Efficiency as a function of Z-p_T for various ZZ aTGC and SM with $\pm 1\sigma$ error bars

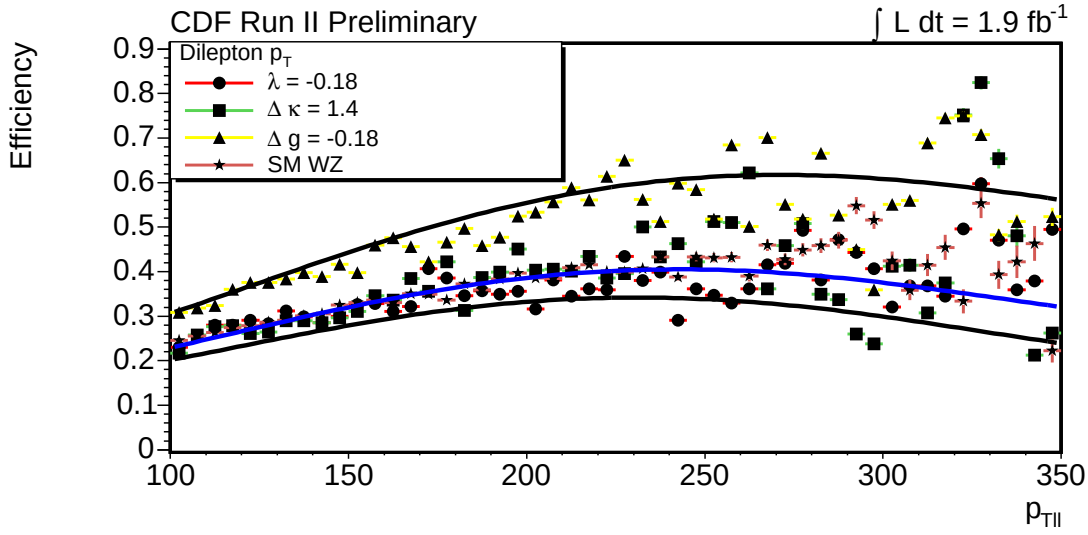

Figure 7.20: Efficiency as a function of Z-p_T for various WZ aTGC and SM with $\pm 1\sigma$ error bars in the regions with significant statistics

isolation cone, this removes the lepton from consideration. In essence, as our Z becomes higher and higher in momentum, eventually our leptons self-veto, leading to a reduction of efficiency for high values of dilepton p_T.

7.5.6 Test Statistic

We require a well-behaved test statistic to allow us to discriminate between signal and background. In this case we base our test statistic on a simple likelihood ratio:

$$T = Log(\frac{L(s = N_{ExpectedSignal}/N_{Data})}{L(s = 0)}) \tag{7.1}$$

where:

$$L(s) = \prod_{i=1}^{N_{Data}} s \times P_{signal}(x_i) + (1 - s) \times P_{background}(x_i) \tag{7.2}$$

Here $P_{background}$ is the probability that the event is background, P_{signal} is the probability that the event is signal, both from the templates, N_{Data} is the number of events in data, and $N_{ExpectedSignal}$ is the yield predicted by MC. The probabilities are created by using the signal and background templates, and in both cases, normalizing the total area under the curve to one. This allows us to use the signal and background templates as Probability Density Functions, which become the measure of the relative probability that an event is signal, or that an event is background.

A separate test statistic T can be calculated for each value of the aTGC, based on changing expected yields.

This test statistic is based on the standard Likelihood Ratio that one would use if this analysis was done as a fit. In fact, the test statistic was actually first developed when we were considering using fitting for the optimal signal fraction as the method of choice. Because of this, T behaves as you would expect a likelihood ratio to behave, and acts both continuously, and without prejudice, on the data sample.

Table 7.7: R values for aTGC and SM

Bin	λ	$\Delta\kappa$	Δg	Standard Model
Med.	8.73%	9.28%	8.61%	11.2%
High	7.09%	7.84%	6.62%	10.6%

7.5.7 WZ Signal Contamination

In the WZ channel, there is a probability that extra background can be generated by the signal. In this case, a $WZ \to \ell\ell\ell\nu$ event with two extra jets can masquerade as a $WZ \to \ell\ell jj$ event, since we do not veto on extra leptons or extra MET. The dijet mass spectrum of $WZ \to \ell\ell\ell\nu + 2j$ events was studied and found to be very similar to that of the Z + jets background. To compensate for this effect, we decided to add a factor to the background equal to a small percentage of the signal.

We calculated the size of the effect using the value R, where R is defined by:

$$R = \frac{N_{4jets}}{N_{2jets}}$$

The results for R values calculated from out $WZ \to \ell\ell jj$ samples are available in Table 7.7.

Because of the difference in cross-section between $WZ \to \ell\ell jj$ and $WZ \to \ell\ell\ell\nu$, we estimate that the total cross-section of $WZ \to \ell\ell\ell\nu + 2j$ events will be a factor of 3.5 lower then this. Being conservative, we therefore add a factor of 3% of the signal size to the background for each aTGC value.

7.6 Distributions and Toy MC

In order to properly map the expected behavior of data we used what is known as "toy MC", a very simple Monte Carlo generator created by picking numbers randomly from a very simple distribution. In this case, we were only using information from one distribution, the dijet mass distribution. Using this simple toy MC we run thousands of mock experiments, which simulate the results we could expect from the entire CDF Run II $1.9fb^{-1}$ dataset.

For each experiment we pick a number of events from both background and signal based upon their expected yields in each bin. The expected yield for background comes from the expectation predicted by the PYTHIA Z + jets MC, modified by a correction factor equal to the amount of data in the control region over the amount expected. The amount of signal comes from the signal MC, operated on by the UEF to get a yield, multiplied by the k-factor to account for NLO. In other words:

- Signal Yield: Generator Yield times Efficiency Function times NLO k-factor.
- Background Yield: PYTHA expectation times $\frac{Data}{MC}$ in control regions + Signal Dependent Correction (WZ only).

The yield is poisson-varied seperately for each experiment in order to account for the wide statistical variation in number of events expected in each actual run of data.

Background events are picked by randomly selected a dijet mass point out of the background templates in each bin. Signal events are selected in much the same way. A full toy MC dataset looks like a series of dijet mass values, which is exactly the same as what we will receive from data.

Those values then undergo an unbinned calculation of the test statistic, using the templates they were generated from as probability distribution functions. Each dijet mass value generates an L-ratio, which is summed together in logarithmic form to create the total T value for the entire experiment. This procedure is repeated thousands of times, both for every value of aTGC, and for the SM point, where there is no WZ/ZZ contribution at all.

7.6.1 T-value Distributions and Limits

95% confidence level limits can be extracted directly from the distribution of T-values that comes out of the toy MC. We can calculate the 95% CL cutoff point, the T-value for which 95% of toy MC experiments have a higher T-value, meaning that they look more like signal then background. Should the T-value from data be

Table 7.8: Expected ZZ Limits for $\Lambda = 1.2$ TeV

Coupling	Expected Limit w/o Systematics	Expected Limit w/ Systematics
f_4^Z	(-0.09,0.09)	(-0.11,0.11)
f_5^Z	(-0.09,0.08)	(-0.12,0.11)
f_4^γ	(-0.09,0.09)	(-0.11,0.11)
f_5^γ	(-0.10,0.09)	(-0.12,0.11)

above that point, then data will be consistent with that signal. Should the T-value from data be below that point, then we can safely say that the probability of that aTGC point creating that data value is less then 95%, and that the aTGC point has been excluded at a 95% CL.

7.6.2 Expected Limits

Expected Limits are determined jointly from the signal T-value distribution for various aTGCs, and the background T-value distribution. We use the signal T-value distribution to calculate the 95% cutoff point. We can then compare it to the background-only T-value distribution. The percentage of the background-only distribution that has a higher T-value then the 95% cutoff is the percent chance that background will fake signal at this particular aTGC.

The aTGC point where the chance of background faking signal is exactly 50% would be our ideal expected limit - the point where half the time the SM background looks more like signal, and half the time less like signal. Since we do not want to go into that level of exact detail, we pick the point closest to 50%, but from the bottom side, where the majority of events have T-values lower then the 95% cutoff. This provides a slightly conservative expected limit.

Expected results for several aTGC values are given in Tables 7.8, 7.9, and 7.10.

7.6.3 Fitting

Also of interest, a fit is performed to optimize the test statistic, and to help calculate a signal fraction as a function of that same statistic. In this case, the

Table 7.9: Expected WZ Limits for $\Lambda = 1.5$ TeV

Coupling	Expected Limit w/o Systematics	Expected Limit w/ Systematics
Δg	(-0.15,0.25)	(-0.16,0.26)
$\Delta\kappa$	(-0.81,1.09)	(-0.88,1.16)
λ	(-0.13,0.14)	(-0.14,0.15)

Table 7.10: Expected WZ Limits for $\Lambda = 2.0$ TeV

Coupling	Expected Limit w/o Systematics	Expected Limit w/ Systematics
Δg	(-0.14,0.24)	(-0.15,0.24)
$\Delta\kappa$	(-0.73,1.00)	(-0.81,1.07)
λ	(-0.12,0.12)	(-0.13,0.13)

test statistic is interpreted as a proper likelihood ratio, of the form:

$$T = Log(\frac{L(s)}{L(0)}) \tag{7.3}$$

where:

$$L(s) = \prod_{i=1}^{N_{Data}} s \times P_{signal}(x_i) + (1-s) \times P_{background}(x_i) \tag{7.4}$$

and s, the signal fraction, is allowed to float. This quantity is maximized using the tools provided with root. Signal fractions are reported in Chapter 9.4 and are unconstrained, and thus allowed to go negative.

7.6.4 Fit Tools

Fitting was accomplished by minimizing a set of likelihood values representing the total likelihood that a pseudo-event belonged to a given template. Minimization was handled by using the TMinuit module of root version 4.00/08, incorporated as part of the 6.1.4 release of the CDF Software. TMinuit is a minimization package originally deriving from the MINUIT package, part of PACKLIB, written in Fortran by Fred James, and is described in [25]. TMinuit was written by R.

Brun in order to bring the functionality of the original MINUIT package to the C environment of root, and has been widely tested.

Our fitter operates by only allowing one parameter to float free, the signal fraction, and our pseudo-dataset consists entirely of M_{jj} datapoints, created from a combination of signal and background templates. The likelihood fit is unbinned, meaning that the M_{jj} pseudo-data point is compared directly with the probability value of the template. Our minimization routine minimizes the -2 Log Likelihood of the sum total of pseudo-data events.

Initialization sets the starting parameter, the signal fraction, to 0.0, and the step size to 0.1. The value is then run through a variety of different scanning procedures as described below. The results do not change significantly as a function of initial signal fraction. Due to the nature of TMinuit, each step can alter the step size, and the final value is then passed onto the next procedure. The actual minimization routines used are all based on the MIGRAD procedure, using different search strategies.

MIGRAD

MIGRAD is a minimization routine developed from the gradient method outlined in [20], as implemented in the TMinuit package. MIGRAD depends on knowledge of first derivatives, and uses these to approximate the second derivatives of a function is necessary. As part of its running procedure, MIGRAD checks for positive-definiteness, and produces a set of error matricies. MIGRAD is the method recommended for use by the TMinuit documentation.

SIMPLEX

We run a brief scan with the SIMPLEX method in addition to using MIGRAD. SIMPLEX appears to be a produce of the Simplex Method, or Downhill Simplex Method developed by Nelder and Mead [27], which is designed to find local minima on functions that vary smoothly. Only one scan is done with SIMPLEX during the course of the minimization.

Errors

Parabolic errors on the parameter, the signal fraction, are reported automatically by TMinuit, based on the covariance matrix as determined by the scanning parameter in question. Limits on the accuracy of the error measurement, and on possible situations that may fool the minimization procedure are outlined in the TMinuit documentation. The outcome of the fit does not depend on the error, although it remains a good measure for the accuracy of the final signal fraction.

Part of this chapter is being considered for potential publication by the CDF Collaboration.

Chapter 8

Systematics for the WZ/ZZ Anomalous Triple Gauge Coupling Analysis

8.1 Overview

Of course, estimates based on a detector simulation (written by humans), based on physics models of astonishing complexity (written by non-experimental physicists), run on computers (built by engineers) with the aid of an active C++ interpreter (written, apparently, by the Devil), cannot ever be wholly accurate. Our understanding of the detector, of the physics involved, of everything actually, is only mortal, and is somewhat prone to comprehension failure. To deal with that, we attempt to account for these problems by introducing systematics.

In this analysis we introduce systematics by altering the toy MC before generating our toy experiments. We can do this by altering the templates that are used to generate our toy datapoints, or by altering the yield expected out of each experiment. Once this is complete, we then calculate the test statistics for each toy by using the standard distributions. The non-systematic analysis is our best guess of how things should look, so we use it in conjunction with the worst case estimate of how bad things can get to set limits on aTGC parameters.

Our systematics are based on estimations of how far we may have misjudged the actual state of the system. Sometimes, for things like Jet Resolution and Jet Energy Scale, the behavior of the CDF detector with respect to the physics it involves is well understood. In other cases, such as the error introduced by the way we created the Universal Efficiency Function, we have to parameterize our error on our own. In any case, we have to justify, for each systematic, that we did the correct thing in regards to estimating the effects on data.

We divide our systematics into three general categories, ones that effect the signal templates, ones that effect the background templates, and ones that effect the signal yield. We list them as follows:

- **Signal Systematics** Systematics that alter the signal templates.
  - **Jet Resolution** The error on the detector's ability to reconstruct jets.
  - **Jet Energy Scale** The error on reconstructing the energy in the attendent jet.
- **Background Systematics** Systematics that alter the background templates.
  - **Background Shape** A M_{jj} dependent variation to account for imperfect jet reconstruction, based on Data/MC in the Control Region.
- **Yield Systematics** Systematics that alter the total signal yield.
  - **Universal Efficiency Curve** Accounting for the error introduced in using the UEF.
  - **Acceptance Systematics** Corrections for error in predicting the ability of the detector to identify good events.
  - **Factorization Scale (ZZ only)** Correcting for different factorization scales in the Baur and PYTHIA generators.

8.2 Signal Systematics

Signal systematics are those problems with reconstructing the dijet mass that would prevent you from accurately reconstructing the dijet mass peak in real data. These primarily come from the difficulty in fully reconstructing jets to correctly match their initial quark.

8.2.1 Jet Resolution

Jet Resolution is applied in order to account for the imperfect way in which the CDF Run II detector reconstructs jets in the dataset. Due to potential energy loss from out-of-cone particles, calorimeter mismeasurement, and the error introduced by having physical interference between the actual collision and all the measurement components, the detector does not actually measure jets with perfect precision.

The standard procedure for dealing with Jet Resolution is to introduce a Gaussian smear of 10% to the jet four-momenta. We assembled a new signal template by taking jets from the signal MC, and then smearing their momenta multiplicitavely by 10% using a standard Gaussian shape. The resulting template is used to generate events that then have their test statistic values calculated by the standard template. The smeared template is compared to the standard template in Figure 8.1.

8.2.2 Jet Energy Scale (JES)

A series of corrections are used in order to transform the jets as reconstructed in the detector back into particles that resemble the initial partons as much as possible. The total energy of the corrected jets, as compared to their actual energy, is sometimes referred to as the Jet Energy Scale. Errors on our ability to correct for jets will interfere in our ability to properly measure the dijet mass of our signal.

The Jet Energy Scale is originally calibrated using a variety of methods. The Calorimeter energy scales are calculated for the ECAL by using $Z \rightarrow \ell\ell$ events, and comparing the reconstructed dilepton masses to the mass as measured in LEP

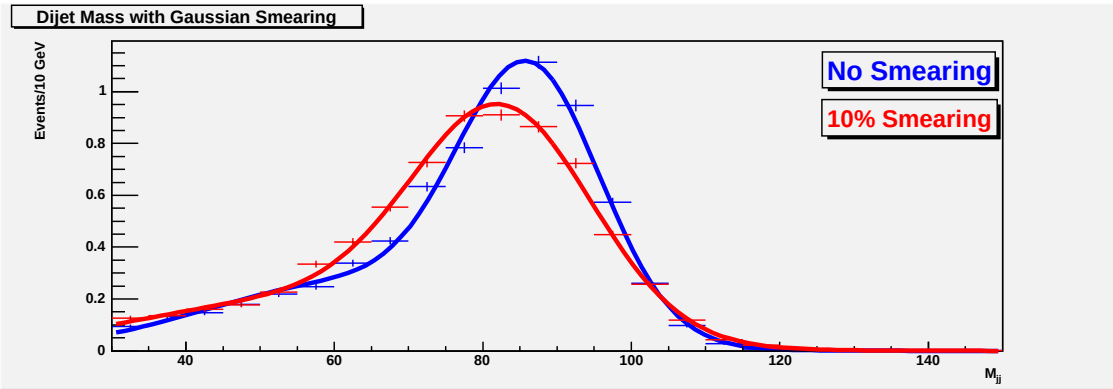

Figure 8.1: ZZ M_{jj} fits with and without 10% Gaussian smearing of jet energies

and by other electroweak precision measurements. The Jet Energy Scale at CDF is also measured by the use of the dijet p_T balance, as described in [14], under the principle that QCD dijet events should have balance around the center of the detector.

More recently, the JES has been measured by using the $t\bar{t} \rightarrow W^+W^-b\bar{b} \rightarrow \ell\nu jjb\bar{b}$ final state. In this case, the two corrected jets from one of the Ws are added together, and their total mass compared with the known mass of the W boson. This analysis gives a $\Delta_{JES} = 1.27 \pm 0.5$, where Δ_{JES} is defined as the jet energy scale [15].

8.2.3 Combining the Two

The Jet Resolution systematic appears to be dominant over the JES systematic in our analysis. Accordingly, out of a wish to be conservative in our estimates, we take the Jet Resolution systematic as our signal systematic, and ignore the JES systematic when we create our final limits. This provides us with a worst case possibility that is easier to compute then a possible smearing of the two.

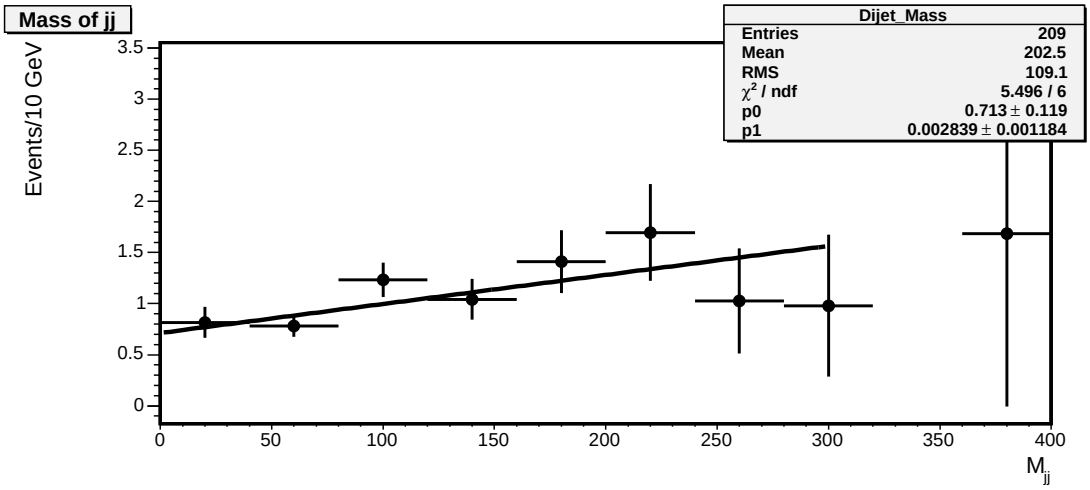

Figure 8.2: Data/MC in control region as a function of M_{jj}

8.3 Background Systematics

There is only one background shape systematic, an adjustment to the general dijet mass spectrum of the Z + Jets background created from the Control Region. We know *a priori* that the ability of PYTHIA to accurately recreate the jet distributions for events with high jet energy or jet multiplicity is somewhat lacking. Hence we expect that the shape of the dijet mass distribution from background in data will be different from the predictions of the PYTHIA MC. To correct for that effect, we add an M_{jj} dependent correction based on the ratio between the Data and the MC prediction in the Control Region.

The ratio is provided in Figure 8.2 as a function of M_{jj}. This shift is then applied to the background template that was created previously to allow a structure with more background in the tails. A comparison of the curve on the two bins is provided in Figures 8.3 and 8.4.

8.4 Yield Systematics

Systematics effecting the overall yield of signal events were calculated and applied together. There were two major sources of these systematics. One was the

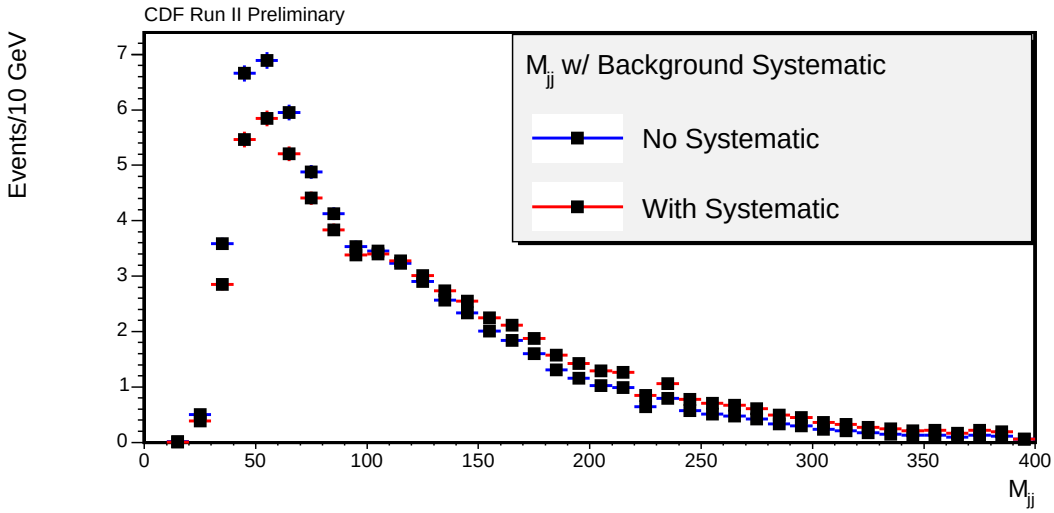

Figure 8.3: Effect of Back Systematic on M_{jj} in Med Bin

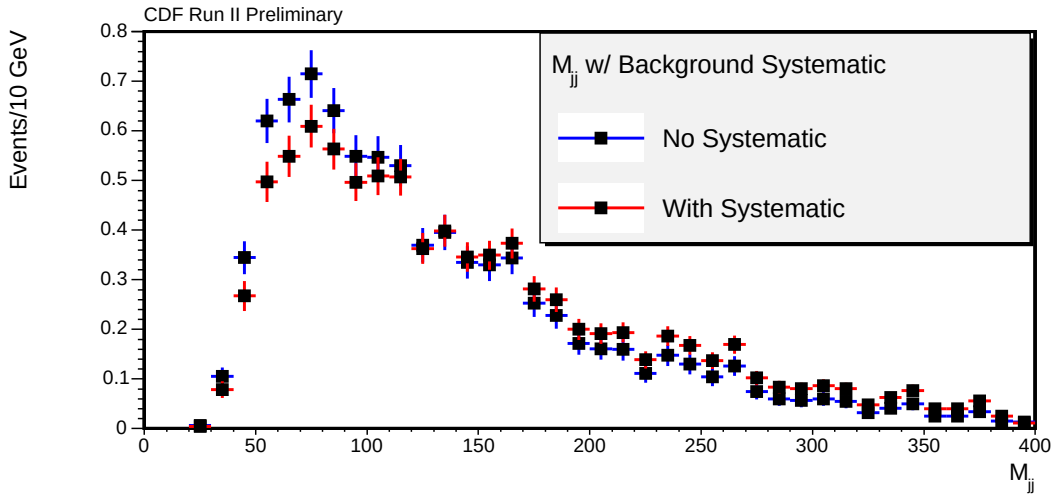

Figure 8.4: Effect of Back Systematic on M_{jj} in High Bin

Table 8.1: Acceptance Systematics from [2] and [28]

dilepton:	
pdf	2%
lepID	1.5%
trigger	0.3%
dilepton total	2.5%
dijet:	
JES	3%
jet resolution	0%
ISR	2%
FSR	3%
dijet total	4.7%
luminosity	6%
Grand Total	8.0%

UEF, error on which could produce fewer signal events from a generator sample then expected. The other are the acceptance systematics that result from detector effects reducing our ability to measure events.

For the ZZ analysis, an additional systematic had to be applied to deal with the different factorization scales involved in the Baur and PYTHIA MC.

8.4.1 Acceptance Systematics

Systematics on the acceptance due to resolution and other detector and physics effects are well-studied at CDF. These systematics arise from our inability to represent the detector perfectly in MC, thus introducing error when we calculate the number of events that will be accepted in the real dataset. The numbers that we used for the acceptance systematics are very similar to the numbers used in a wide variety of other analyses, and were used as part of the CDF standard. In particular, we used the lepton acceptance systematics used previously by the UCSD group in dilepton analyses[2], and the dijet systematics as done in a $WZ/WW \to \ell\nu jj$ analysis [7]. These systematics are presented in Table 8.1

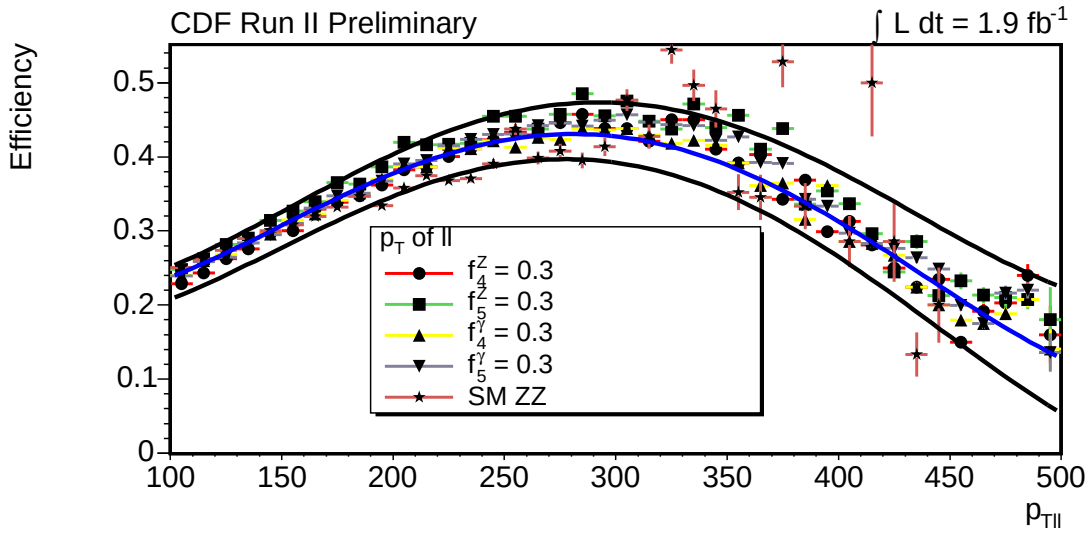

Figure 8.5: Efficiency as a function of Z-p_T for various ZZ aTGC and SM with $\pm 1\sigma$ error bars

8.4.2 Universal Efficiency Curve

The error on the Universal Efficiency Curve is calculated from the discrepency between the points that went into the curve's initial calculation. The variance between the points demonstrates the statistical and possibly the physical variation that can occur between the various aTGC points, and thus should be accounted for as a possible reduction in the yield of the signal.

We assign error curves to the UEF by eye in order to match them to the general shape of the data points. Error curves are provided for the ZZ (Figure 8.5) and WZ (Figure 8.6) analyses seperately. These modified UEFs are then used to calculate the yields, reducing the possible yield and resulting in a looser limit.

Factorization Scale Systematics

During the course of this analysis, it became apparent that the shape of the dilepton p_T distribution, at generator level, was dependent upon the factorization scale of the Monte Carlo. By default, the Baur MC uses a flat factorization scale (M_Z), while the Pythia MC uses one that is event dependent ($\hat{s}$). To verify this, we examined the MC distribution for dilepton p_T for both Baur and Pythia, using

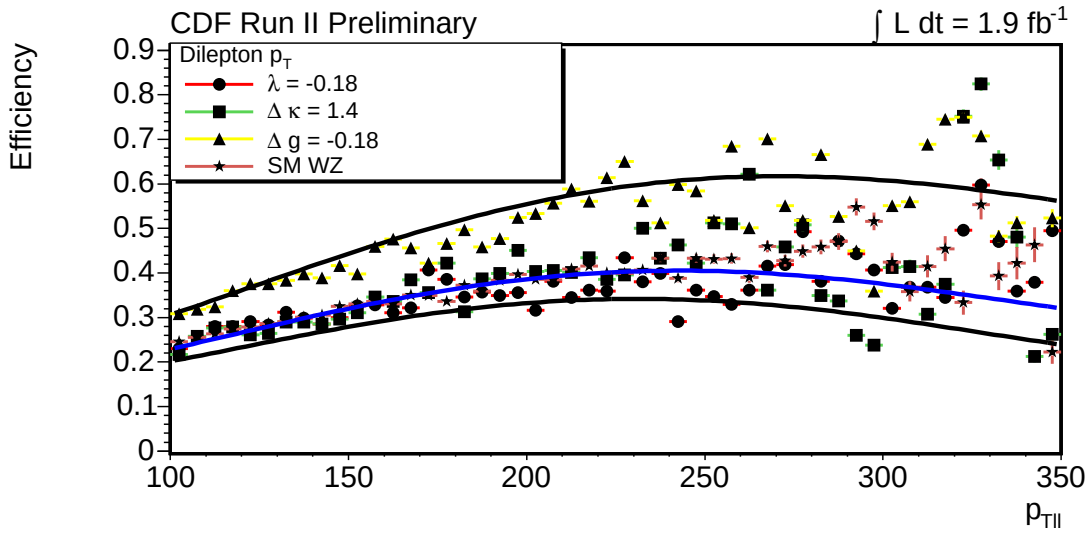

Figure 8.6: Efficiency as a function of Z-p_T for various WZ aTGC and SM with $\pm 1\sigma$ error bars in the regions with significant statistics

the Pythia generator to create SM ZZ samples without showering, both for an $\hat{s}$ based Q^2, and one that was set to M_Z. We then divided the Pythia distribution by the Baur distribution to create ratio plots, illustrated in Figure 8.7. Ideally, these should be one.

We decided to account for this shape deviation by applying a systematic between the Baur M_Z MC and the Pythia $\hat{s}$ MC, done by comparing the Baur SM ZZ Monte Carlo dilepton p_T distribution to that created by Pythia after Baur had received its ZZ boost, and Pythia had undergone showering. The resulting fit can be viewed in Figure 8.9

8.5 Systematic Effects

The final effects of systematics cannot be easily estimated; they can only be examined in their effects on the limits that we end up with. We quantify the effects of systematics by their effect on the final limits, as the systematic effects do not add neatly in quadriture due to their nature.

Table 8.2 demonstrates the shift in aTGC limit caused by adding systematic

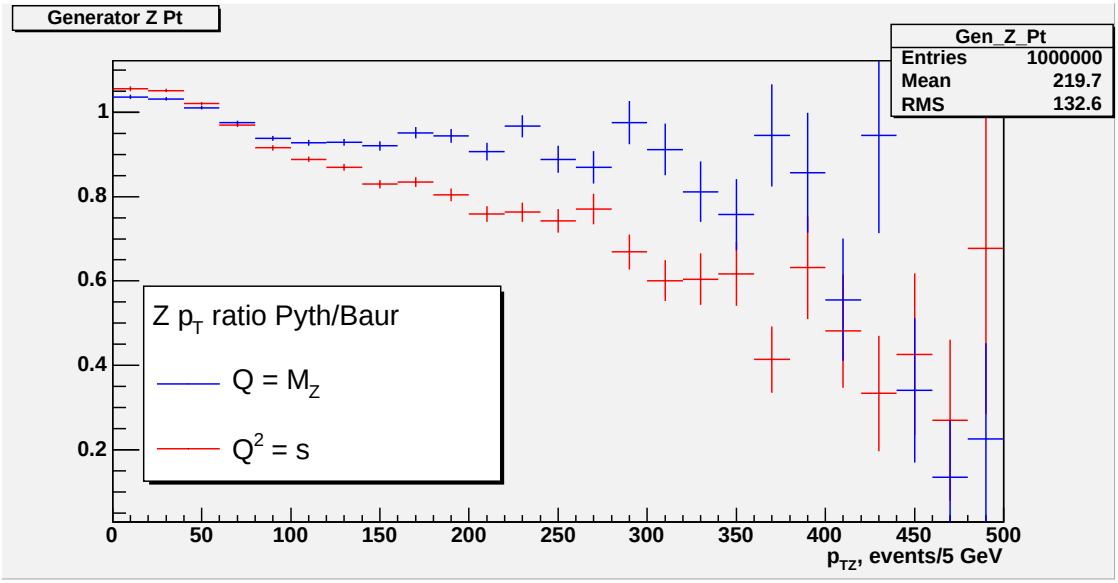

Figure 8.7: Pythia/Baur in dilepton p_T for different values of Q^2

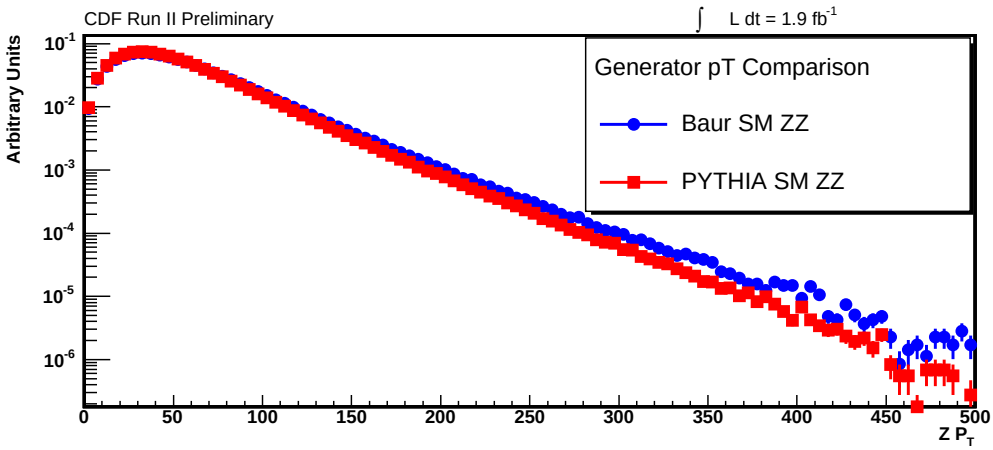

Figure 8.8: p_T of the Z system for Pythia and Baur after boost

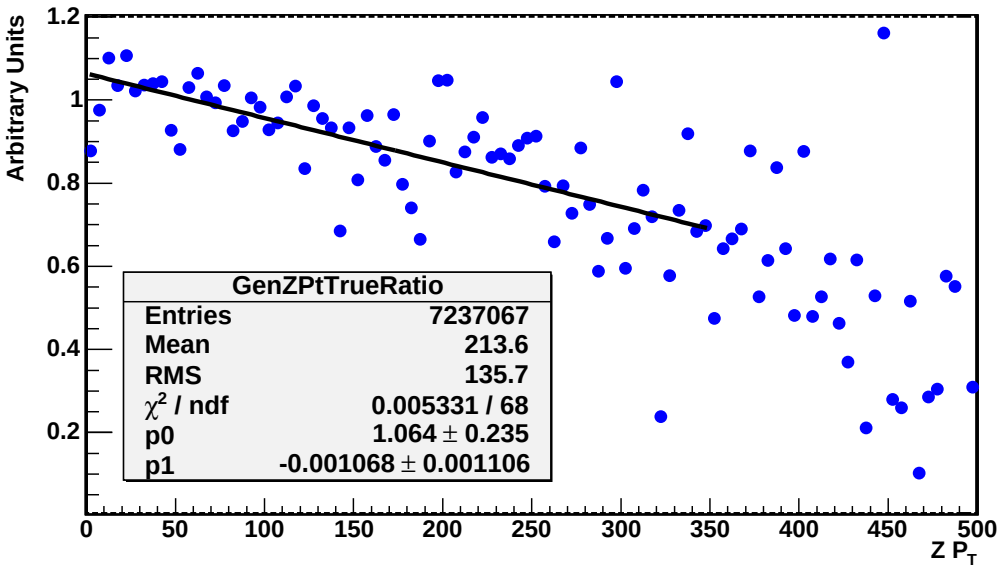

Figure 8.9: p_T of the Z system for Pythia and Baur before correction

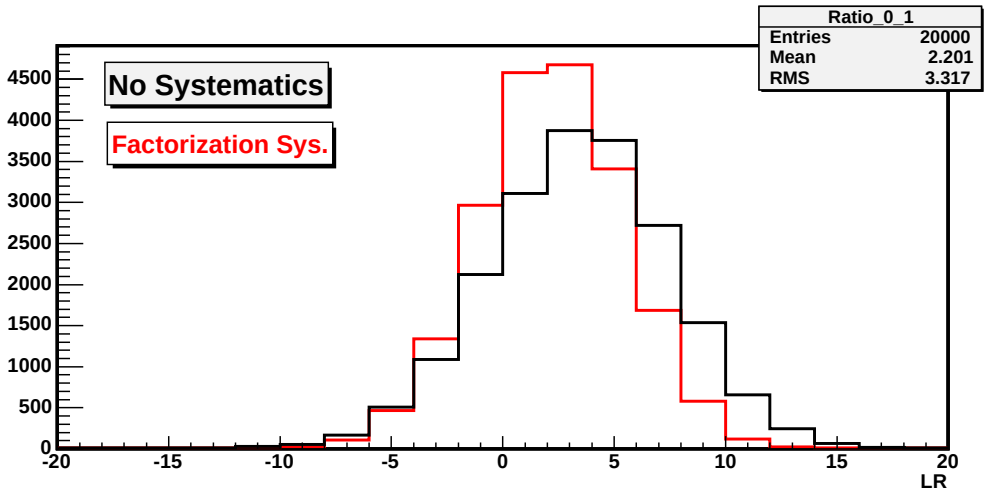

Figure 8.10: LR distribution with and without Factorization Effects

Table 8.2: ZZ Results for $\Lambda = 1.2$ TeV for each systematic

Systematic	f_4^Z	f_5^Z
No Systematic	(-0.08,0.08)	(-0.09,0.08)
Efficiency/Acceptance	(-0.09,0.09)	(-0.10,0.09)
Jet Resolution	(-0.08,0.09)	(-0.09,0.08)
JES	(-0.08,0.08)	(-0.09,0.08)
Background Smearing	(-0.10,0.10)	(-0.11,0.10)
Factorization Scale	(-0.10,0.10)	(-0.11,0.10)

effects to the standard analysis for values of the ZZ aTGC analysis.

Part of this chapter is being considered for potential publication by the CDF Collaboration.

Chapter 9

Results for ZZ/WZ Anomalous Triple Gauge Couplings

9.1 Control Region

The control region was examined before any of the data in the signal region was looked at to determine the possibility of major deviation from MC prediction. No evidence of a massive contradiction was found. The expected yields in the control region are compared to the actual yields in data in Table 9.1

The actual data distributions in the Control Region can be seen in Figures 9.1, 9.2, and 9.3. The best fit results are shown in Figure 9.4.

9.2 Yields

Yields in each bin are the same for both the ZZ and WZ analyses. A comparison is provided between the expectations from MC and the results from data for the Medium Bin in Table 9.2, and for the High Bin in Table 9.3. The ratio of data/MC expectation in each bin is provided in Table 9.4, and the toy MC was corrected based upon the ratio in the Control Region.

Table 9.1: Expected Yields in Control Region with Statistical Errors

channel	Zee	Zmm	WW	WZ	ZZ
e e	76.3 ± 0.5	0.0 ± 0.0	0.023 ± 0.003	1.62 ± 0.01	2.16 ± 0.017
μ μ	0.0 ± 0.0	54.9 ± 0.5	0.020 ± 0.003	1.248 ± 0.009	1.77 ± 0.015
e trk	19.3 ± 0.3	0.0 ± 0.0	0.018 ± 0.002	0.444 ± 0.005	0.608 ± 0.009
μ trk	0.0 ± 0.0	20.1 ± 0.3	0.011 ± 0.002	0.463 ± 0.006	0.624 ± 0.009
Total	95.6 ± 0.6	75.0 ± 0.5	0.073 ± 0.005	3.77 ± 0.02	5.15 ± 0.03

channel	Total	Data
e e	80.1	110
μ μ	57.9	55
e trk	20.4	23
μ trk	21.2	21
Total	$179.6 \pm 0.8^{stat} \pm 14.4^{sys}$	209

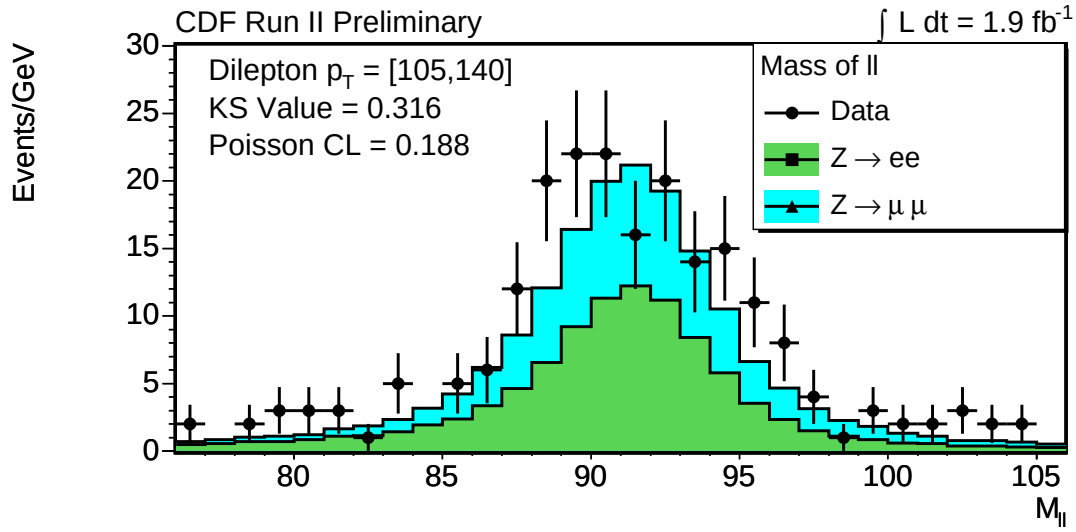

Figure 9.1: M_{ll} distribution in control region

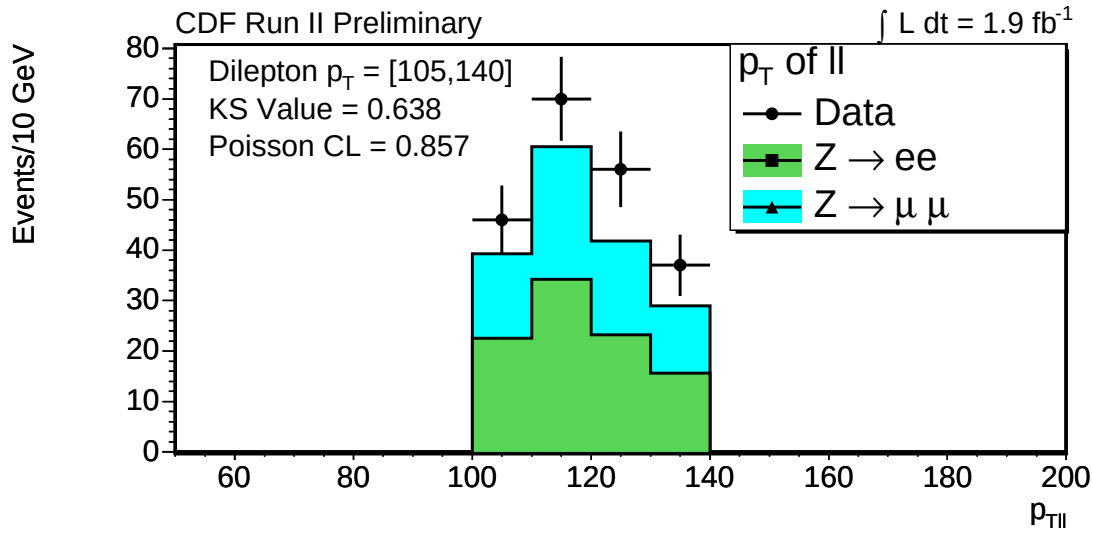

Figure 9.2: Pt_{ll} distribution in control region

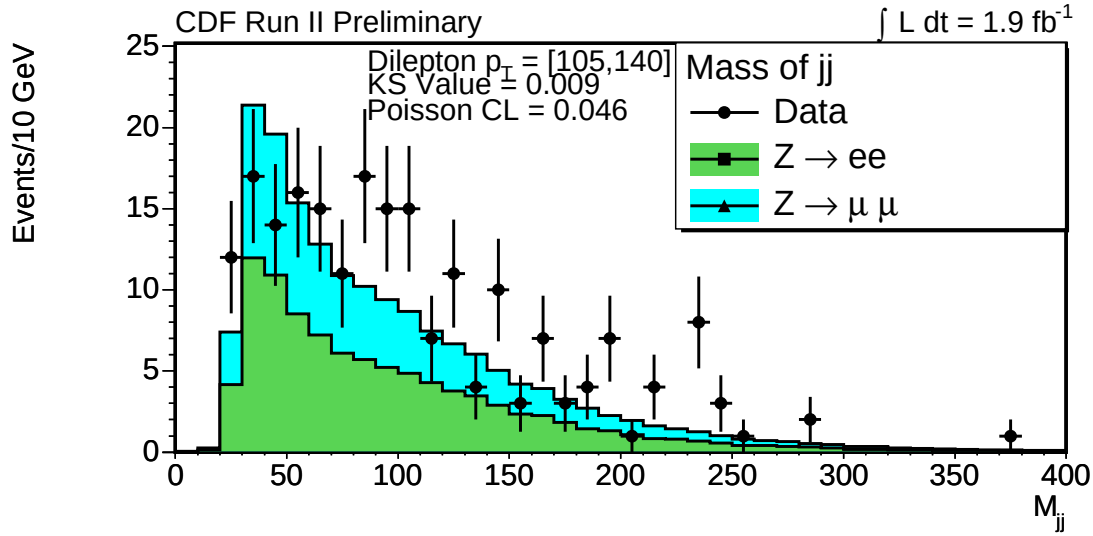

Figure 9.3: M_{jj} distribution in control region

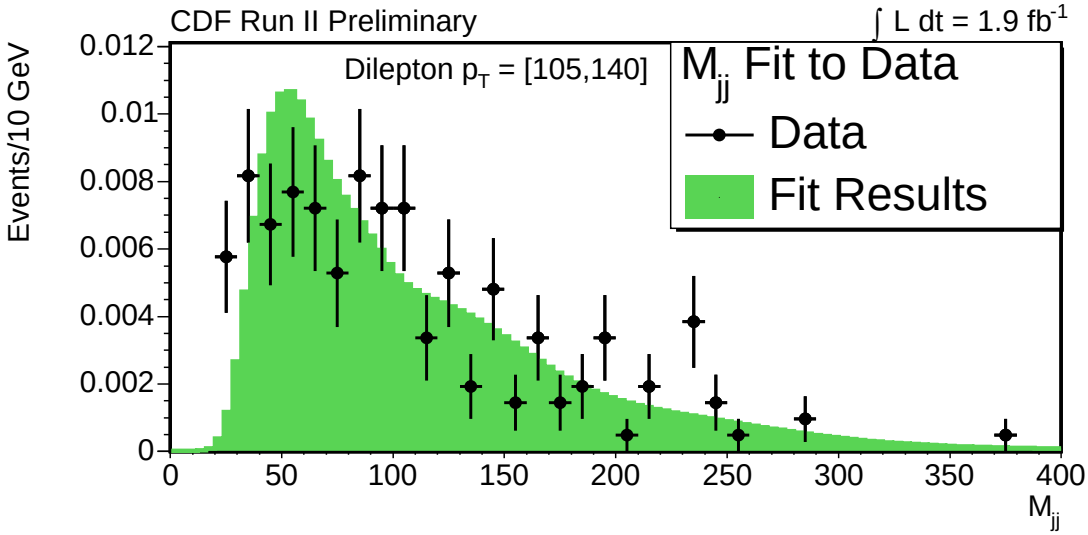

Figure 9.4: Fitted M_{jj} distribution in control region(MC inflated according to fit)

Table 9.2: Expected Yields in Med Region with Statistical Errors

channel	Zee	Zmm	WW	WZ	ZZ
e e	28.8 ± 0.3	0.0 ± 0.0	0.006 ± 0.001	0.833 ± 0.007	1.24 ± 0.01
μ μ	0.0 ± 0.0	22.0 ± 0.3	0.006 ± 0.001	0.679 ± 0.007	1.02 ± 0.01
e trk	7.9 ± 0.2	0.0 ± 0.0	0.003 ± 0.001	0.232 ± 0.004	0.352 ± 0.007
μ trk	0.0 ± 0.0	7.7 ± 0.2	0.004 ± 0.001	0.238 ± 0.004	0.350 ± 0.007
Total	36.7 ± 0.3	29.8 ± 0.3	0.018 ± 0.002	1.98 ± 0.01	2.96 ± 0.02

channel	Total	Data
e e	30.0	34
μ μ	23.8	36
e trk	8.5	17
μ trk	8.3	10
Total	$71.4 \pm 0.5^{stat} \pm 5.7^{accept}$	97

Table 9.3: Expected Yields in High Region with Statistical Errors

channel	Zee	Zmm	WW	WZ	ZZ
e e	3.6 ± 0.1	0.0 ± 0.0	0.0 ± 0.0	0.136 ± 0.003	0.259 ± 0.006
μ μ	0.0 ± 0.0	3.0 ± 0.1	0.0 ± 0.0	0.127 ± 0.003	0.238 ± 0.006
e trk	1.08 ± 0.06	0.0 ± 0.0	0.001 ± 0.000	0.044 ± 0.002	0.082 ± 0.003
μ trk	0.0 ± 0.0	1.04 ± 0.06	0.001 ± 0.000	0.040 ± 0.002	0.077 ± 0.003
Total	4.7 ± 0.1	4.0 ± 0.1	0.001 ± 0.001	0.347 ± 0.005	0.656 ± 0.009

channel	Total	Data
e e	4.0	5
μ μ	3.4	4
e trk	1.2	2
μ trk	1.2	1
Total	$9.74 \pm 0.178^{stat} \pm 0.78^{accept}$	12

Table 9.4: Ratio of Data to Pythia MC in each bin

Bin	Ratio Data/Pythia Expectations
Control	1.16
Med	1.36
High	1.23

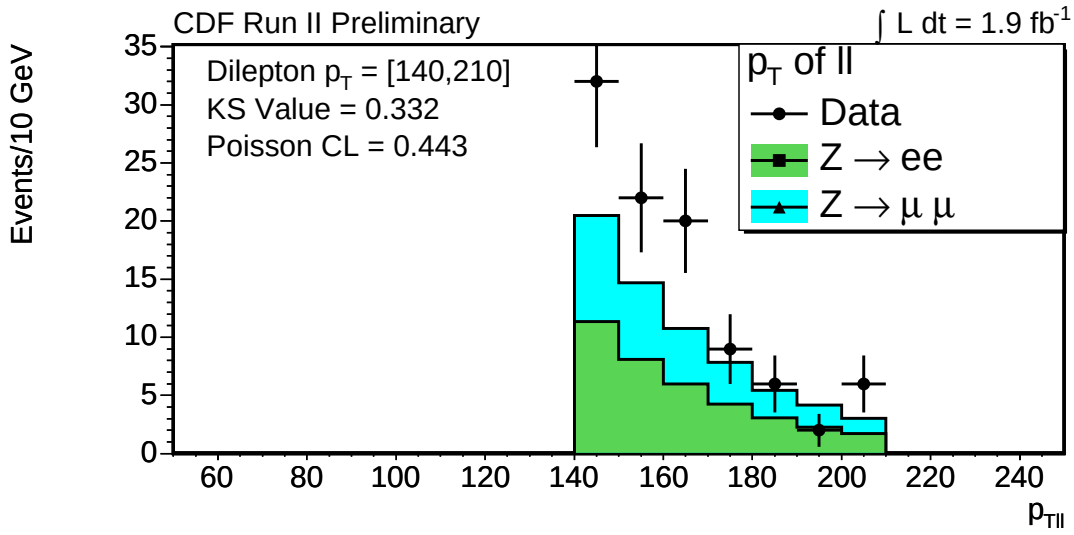

Figure 9.5: p_{Tll} in the Medium Region

Table 9.5: ZZ Results for $\Lambda = 1.2$ TeV

Coupling	Expected Limit w/o Systematics	Expected Limit w/ Systematics	Limit w/o Systematics	Limit w/ Systematics
f_4^Z	(-0.09,0.09)	(-0.11,0.11)	(-0.08, 0.08)	(-0.12,0.12)
f_5^Z	(-0.09,0.08)	(-0.12,0.11)	(-0.10, 0.09)	(-0.13,0.12)
f_4^γ	(-0.09,0.09)	(-0.11,0.11)	(-0.09,0.09)	(-0.10,0.10)
f_5^γ	(-0.10,0.09)	(-0.12,0.11)	(-0.10,0.09)	(-0.11,0.11)

9.3 Distributions

The data distriputions are displayed below in plot form for the two signal bins, the Medium Bin, and the High Bin.

9.4 Final Limits

Final limits for ZZZ and ZZγ aTGCs are provided in Table 9.5 for $\Lambda = 1.2$ TeV, and partial results for f^Z are provided for the no-systematics case for $\Lambda = 750$ GeV to compare with the expected limits provided by Baur in [12].

Limits are provided for the WZ aTGC limits in Table 9.7 for $\Lambda = 1.5$ TeV and

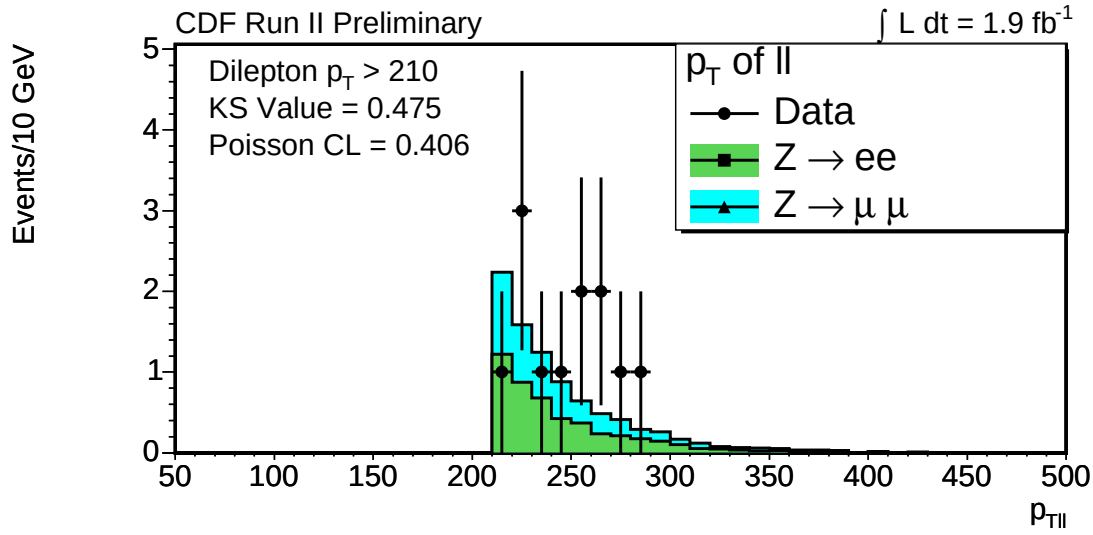

Figure 9.6: p_{Tll} in the High Region

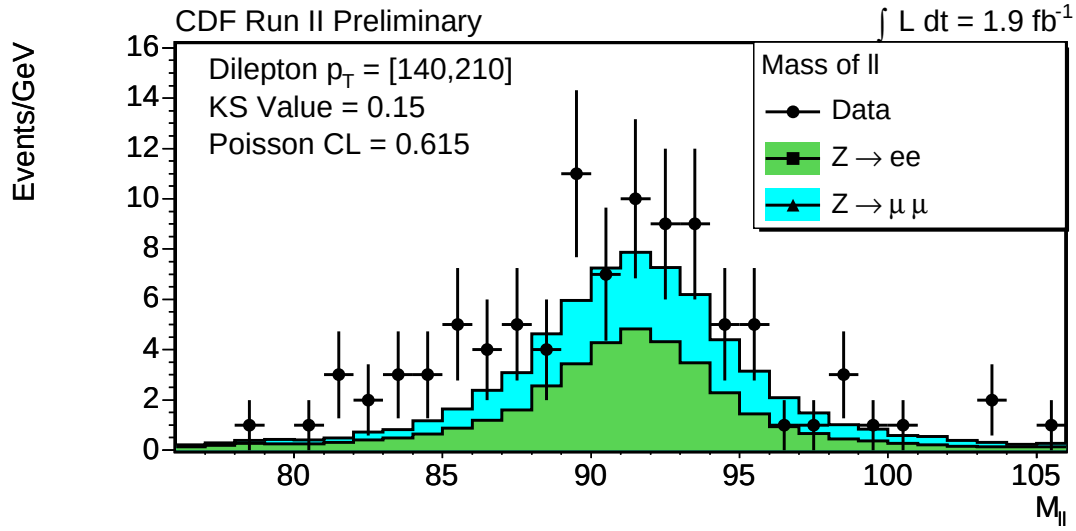

Figure 9.7: M_{ll} in the Medium Region

Table 9.6: Results for $\Lambda = 750$ GeV

$aTGC$	LEP2 limit	Expected(No Sys)	Actual(no Sys)
f_4^Z	(-0.30,0.30)	(-0.20,0.20)	(-0.18,-0.18)
f_5^Z	(-0.34,0.36)	(-0.22,0.2)	(-0.20,0.18)

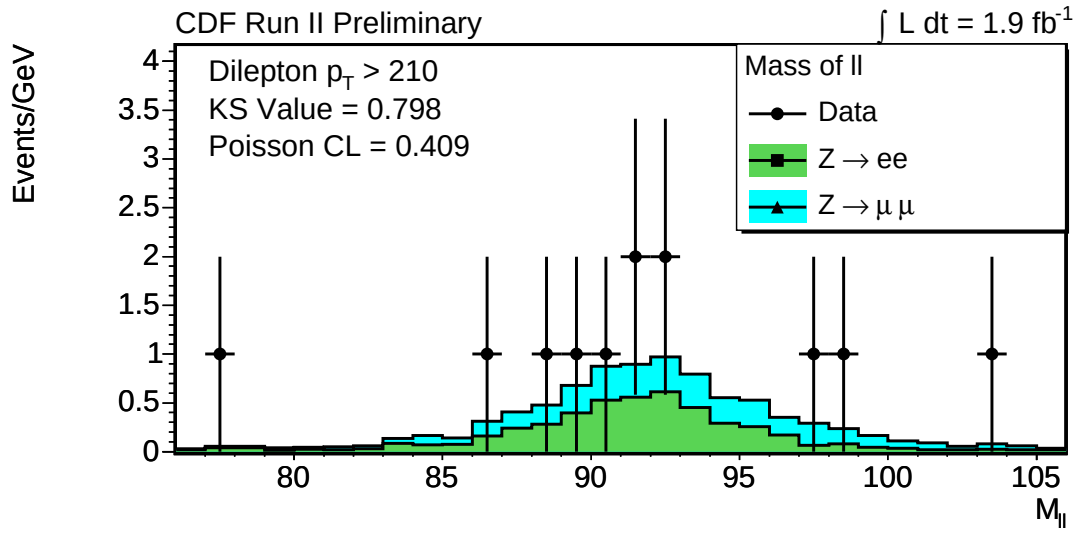

Figure 9.8: M_{ll} in the High Region

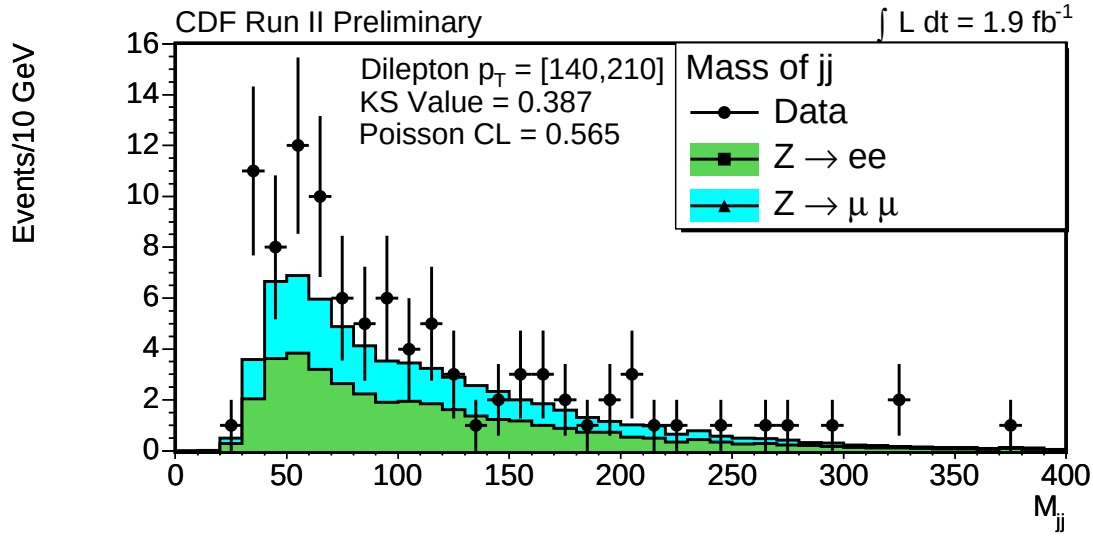

Figure 9.9: M_{jj} in the Medium Region

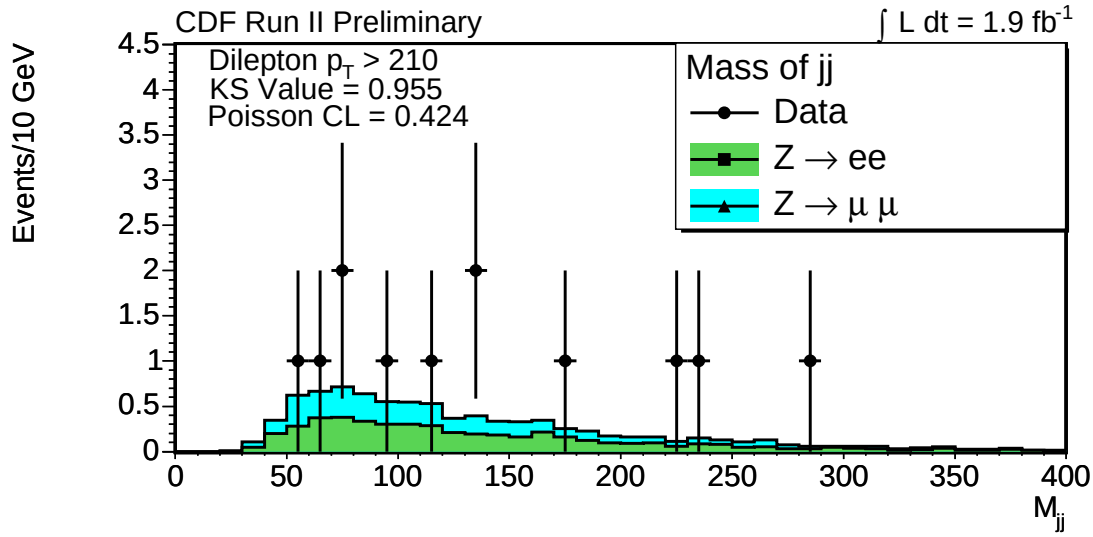

Figure 9.10: M_{jj} in the High Region

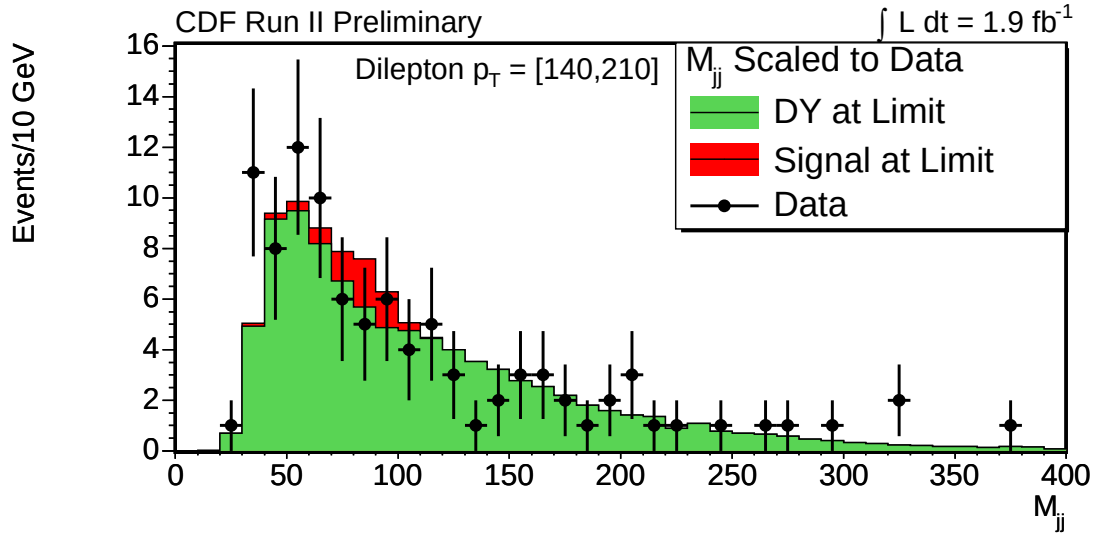

Figure 9.11: M_{jj} in the Medium Region with MC expectancy at ZZ limit, normalized to data

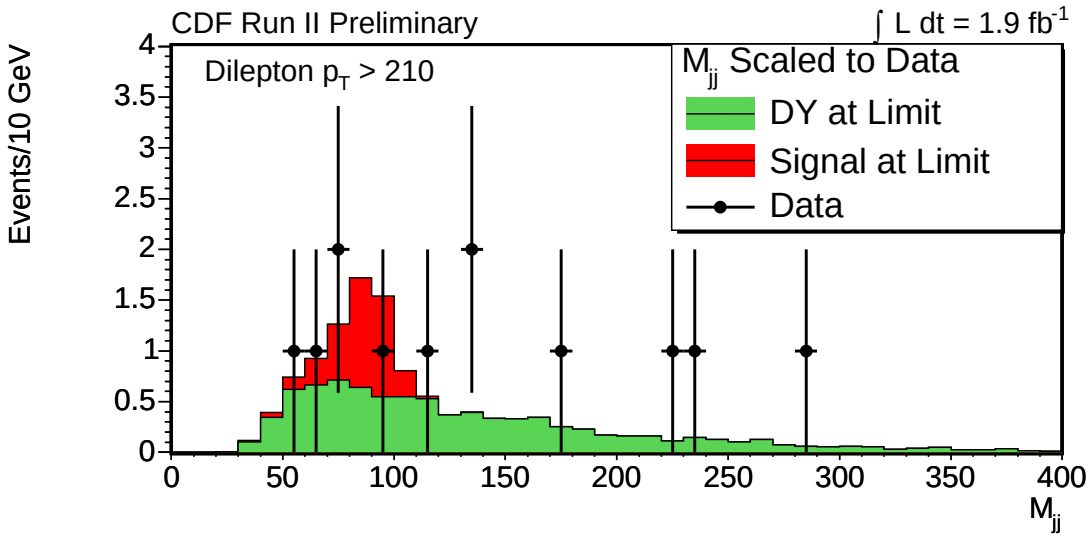

Figure 9.12: M_{jj} in the High Region with MC expectancy at ZZ limit, normalized to data

Table 9.7: WZ Results for $\Lambda = 1.5$ TeV

Coupling	Expected Limit w/o Systematics	Expected Limit w/ Systematics	Limit w/o Systematics	Limit w/ Systematics
Δg	(-0.15,0.25)	(-0.16,0.26)	(-0.15,0.26)	(-0.22,0.32)
$\Delta\kappa$	(-0.81,1.09)	(-0.88,1.16)	(-0.72,1.03)	(-1.09,1.40)
λ	(-0.13,0.14)	(-0.14,0.15)	(-0.13,0.14)	(-0.18,0.18)

in Table 9.8 for $\Lambda = 2.0$ TeV.

The best fit signal fractions are reported in Table 9.9 for ZZ, and 9.10 for WZ. Cross-section limits for the production of ZZ and WZ bosons are provided for each bin in dilepton p_T in Tables 9.11 and 9.12.

9.5 Conclusions

The Standard Model is still intact. It is difficult to provide any other analysis more thorough, and at the same time, more damning then that. I could wax eloquent about how limits on λ at 2.0 TeV are at 0.11, which is stricter then 0.12, but less strict then if they had been at 0.10, but the first sentence says it all. We

Table 9.8: WZ Results for $\Lambda = 2.0$ TeV

Coupling	Expected Limit w/o Systematics	Expected Limit w/ Systematics	Limit w/o Systematics	Limit w/ Systematics
Δg	(-0.14,0.24)	(-0.15,0.24)	(-0.13,0.23)	(-0.20,0.29)
$\Delta\kappa$	(-0.73,1.00)	(-0.81,1.07)	(-0.67,0.94)	(-1.01,1.27)
λ	(-0.12,0.12)	(-0.13,0.13)	(-0.12,0.13)	(-0.16,0.17)

Table 9.9: ZZ Signal Fraction from best fit for both bins

Bin	Signal Fraction	Error
Med	-0.000840591	0.0666208
High	-0.129442	0.197395

Table 9.10: WZ Signal Fraction from best fit for both bins

Bin	Signal Fraction	Error
Med	-0.074	0.085
High	0.015	0.255

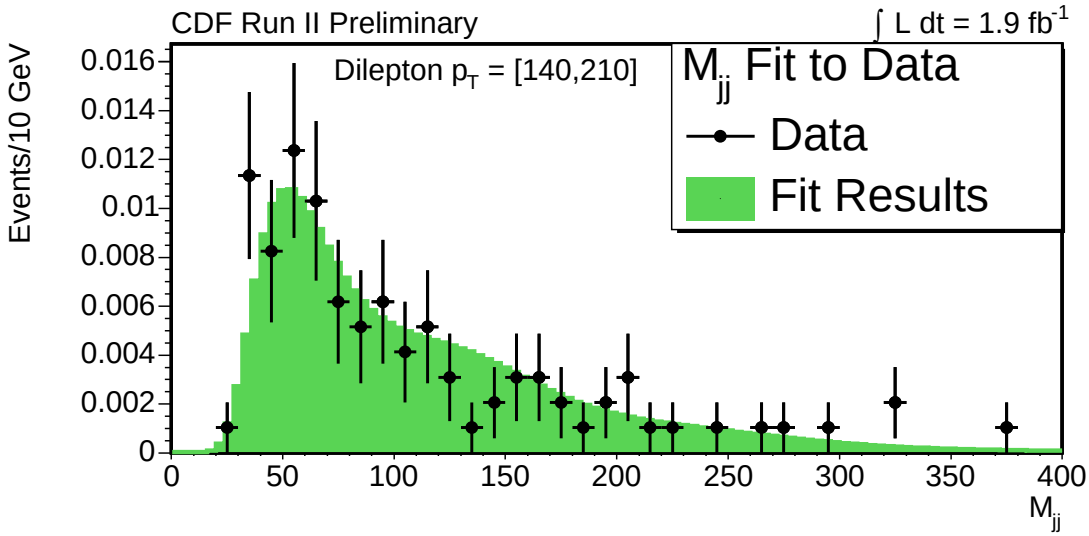

Figure 9.13: M_{jj} in the Med Region with the best ZZ fit to data

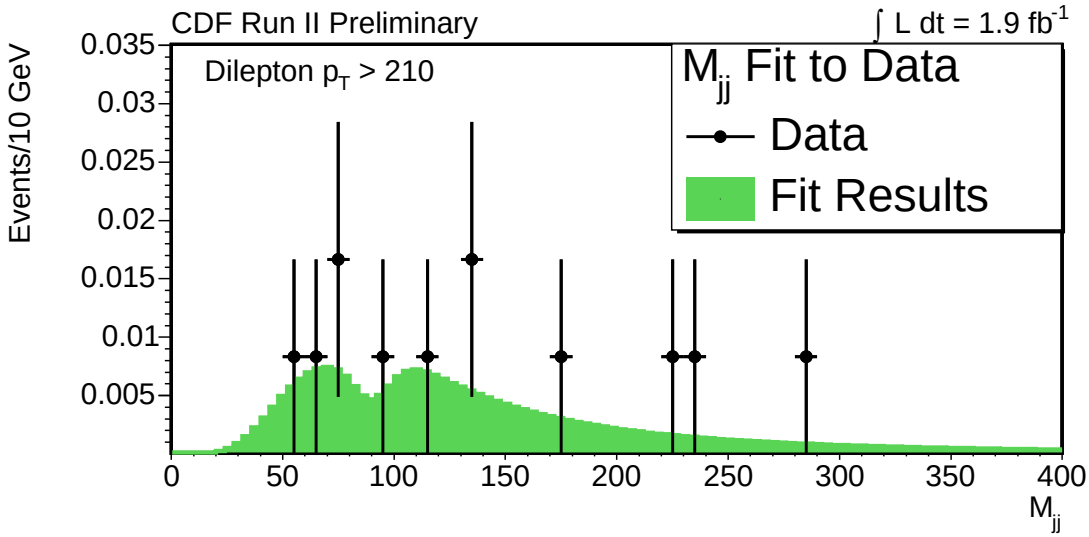

Figure 9.14: M_{jj} in the High Region with the best ZZ fit to data

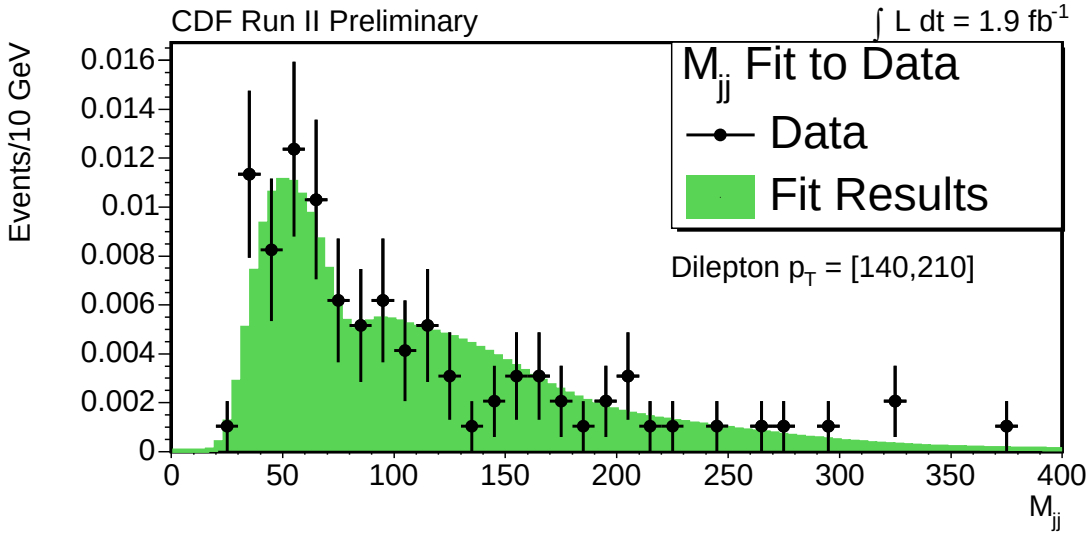

Figure 9.15: M_{jj} in the Med Region with the best WZ fit to data

Table 9.11: 95% CL on the Cross-Section of ZZ production per bin

Bin	95% CL Cross-Section (fb)
Med	280
High	77

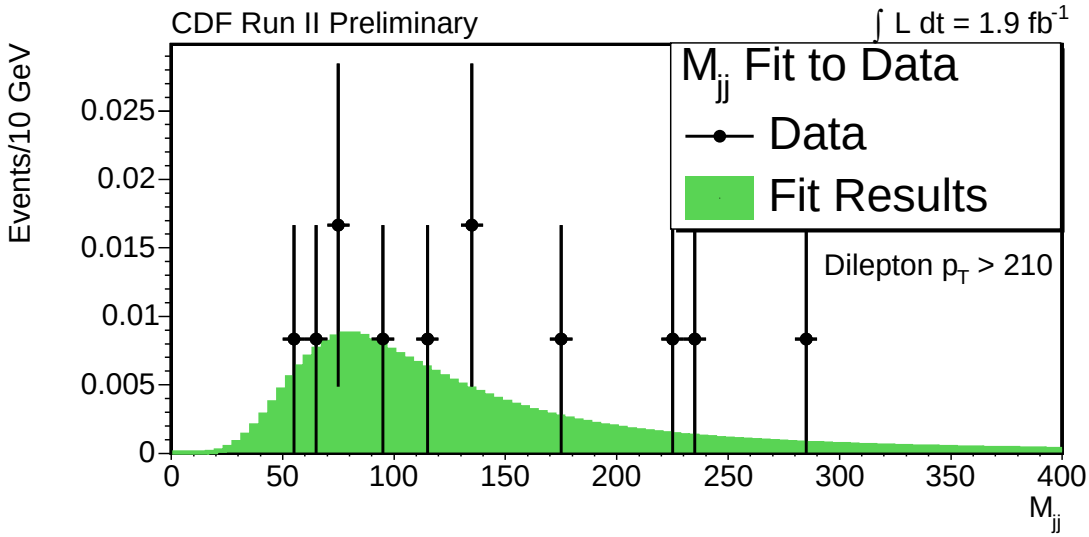

Figure 9.16: M_{jj} in the High Region with the best WZ fit to data

Table 9.12: 95% CL on the Cross-Section of WZ production per bin

Bin	95% CL Cross-Section (fb)
Med	234
High	135

have measured the world's most severe limits on ZZ aTGC, as well as a supporting analysis to WZ aTGC, and have found that in both cases the Standard Model has prevailed.

Part of this chapter is being considered for potential publication by the CDF Collaboration.

Chapter 10

Monte Carlo Study for Z' Search in WZ' Final State

10.1 Overview

The Z' is a standard search to make when considering non-Standard Model signatures. However, the production of a Z' in conjunction with a W is not a standard channel for any known search. This analysis is one of those few searches made not based on theoretical prediction, but on experimental observation.

During the initial $WZ \to \ell\ell\ell\nu$ measurement, in 1.1 fb^{-1} of data, an anomalous event appeared in the data, having a 526 GeV dielectron pair, a 48 GeV CMUP muon, and a 47 GeV $\not\!\!E_T$ signature. This would be consistent with the production of a 526 GeV Z' in association with a real W boson.

This event (run 206537, event 18174367) depends on our new lepton categories to spot one of the electrons. In this case the electron is a CrkTrk electron, disappearing into a crack in the calorimeter fiducial volume, but depositing approximately 100 GeV on one side of the crack and 10 GeV on the other. This is entirely consistent with a very high energy electron impacting on the calorimeter, just by chance in a region where we normally have no acceptance.

It is possible that this event is simply the result of a very off-shell Z along with an associated SM W particle, or possible the result of a very strange measurement

error. But it is also possible that this could be the first sign of the production of a non-SM Z' boson, or other object with a dilepton decay chain, being produced in conjunction with a W boson.

This Z' object has so far not been observed in CDF's dilepton searches for non-SM Z' objects in the $Z' \to ee$ [26], $Z' \to \mu\mu$ [3], and $Z' \to jj$ channels [22], so it may be possible that for some reason it is always produced in conjunction with the W boson. In that case, we need to undergo a search in the WZ final state for a Z with anomalously high mass. We intend to expand the current analysis framework, which has so far focused on more conventional searches for the WZ final state, to assist in this analysis. Our plan is to approach this problem in the same manner that we approached the WZ aTGC analysis, using both the $WZ \to \ell\ell\ell\nu$ and $WZ \to \ell\ell jj$ channels to search for our target.

10.2 Analysis Strategy

The key in this analysis is the high mass of the Z'. Unlike the previous analysis, where the background was dominated by fairly common SM sources, here our background is likely to be very small, as it requires both a Z that is very off-shell (with a mass on the order of 500 GeV), as well as either a pair of jets, or a fake lepton and a large amount of $\not\!\!E_T$.

Because of the very small backgrounds in both channels, creating an exact model of the expected background is nearly impossible, especially given the trouble we will have in comparing such MC production to actual data. Instead we will have to procede by making assumptions about the signal shape, and then using a test statistic similar to the aTGC analysis to probe for an anomalous particle within the right mass range.

Our procedure is to:

- Develop background and signal templates based on minimal MC.
- Develop a test statistic to compare the two, determining the signal significance as a function of the mass of the Z'

- Using the background model, develop a method for determining the probability of the background (null) hypothesis faking a given signal.
- Compare with data and look for evidence of Z' production in conjunction with a W

We have several tags that we use to separate our signal from SM backgrounds:

- $WZ' \to \ell\ell jj$:
  - The high Z' mass.
  - The presence of two jets.
  - A dijet mass consistent with the W mass.

We use these handles to develop two slightly different approaches to the WZ' analysis.

10.3 Backgrounds

10.3.1 $WZ' \to \ell\ell jj$ Backgrounds

As with the previous dilepton-dijet analyses, the primary background for $WZ' \to \ell\ell jj$ comes from Drell-Yan events, where there is a very off-shell Z as well as two associated jets. We model these backgrounds using MC generated as part of the standard CDF MC production. Using the tools developed by the Diboson working group, we estimate that the background from standard model events in a region where the dilepton mass above 400 GeV will be dominated by Drell-Yan. A brief overview of expected background events is presented in table 10.1.

The distributions of background in dilepton and dijet mass are extracted from Monte-Carlo. Background dijet mass is modeled by a function consisting of three Gaussians, as was done in the ZZ and WZ aTGC analyses. Background dilepton mass was modeled by a single falling exponential as the best fit to the decaying ends of the resolution smeared Breit-Wigner distribution. These distributions are included in figures 10.1 and 10.2.

Table 10.1: $WZ' \to \ell\ell jj$ Yields in the Signal Region

Source	Expected Events (1.0 fb^{-1})
$Z \to ee$	2.5
$Z \to \mu\mu$	3.0
$t\bar{t}$	0.30
ZZ	0.063
WW	0.058

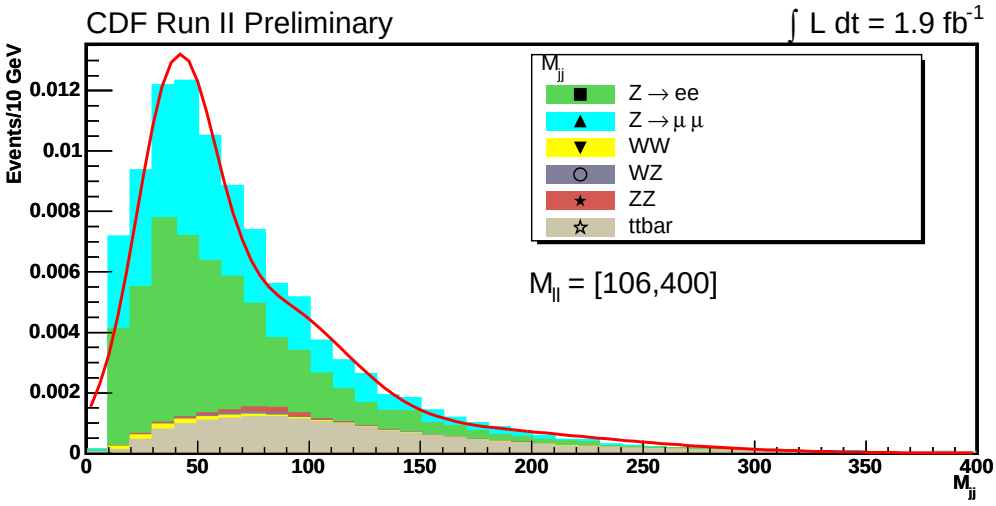

Figure 10.1: Background dijet mass distribution

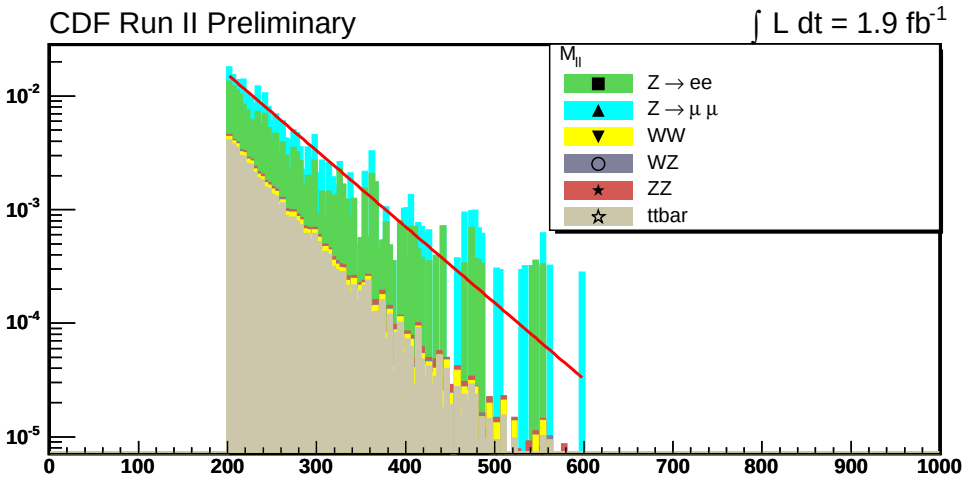

Figure 10.2: Background dilepton mass distribution

10.3.2 Signal Model

The signal is modeled with a special sample of Pythia WZ events in which the Z-mass was forced to be 500 GeV (i.e. very off-shell). This is only used for assesment of the acceptance to convert the yield into a cross-section/limit.

Different templates are created for di-muon and di-electron events to reflect differences in the resolution of the detector, using the above MC. You can see the template shapes in figures 10.3 and 10.4. The di-muon mass peak is fitted to function 10.1 and the di-electron mass peak to function 10.8, where M_0 is the central mass value being tested.

$$0.1095 \times e^{0.5(\frac{x-M_0}{39.79})^2} \tag{10.1}$$

$$t = \frac{x - M_0}{7.63095} \tag{10.2}$$

$$\alpha = 0.839162 \tag{10.3}$$

$$if t > -|\alpha|, v = e^{\frac{t^2}{2}} \tag{10.4}$$

$$elsea = (\frac{3.48568}{|\alpha|})^{3.48568} \tag{10.5}$$

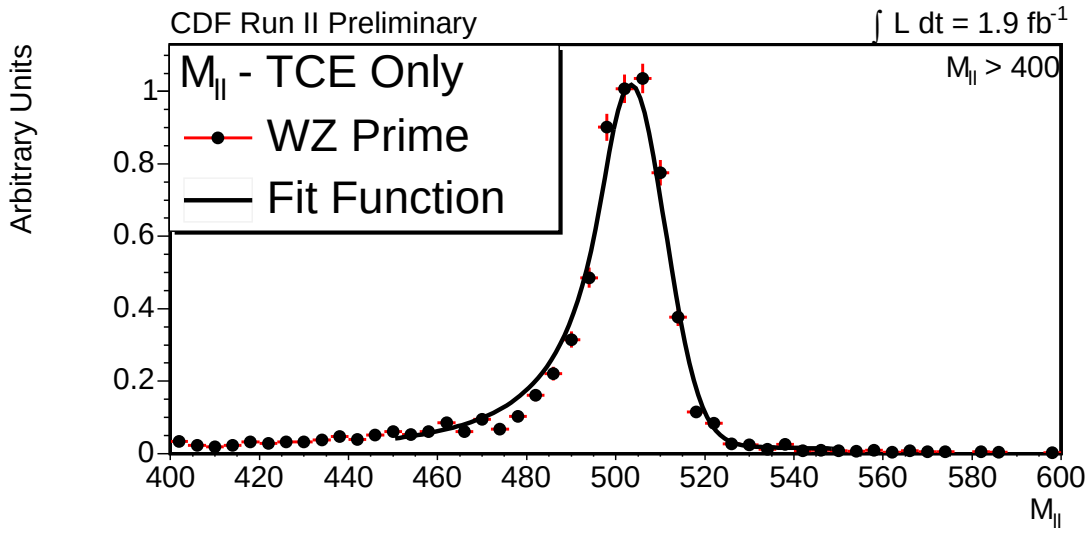

Figure 10.3: Electron dilepton mass distribution in signal

$$b = \frac{3.48568}{|\alpha|} - |\alpha| \tag{10.6}$$

$$v = \frac{a}{(b-t)^n} \tag{10.7}$$

$$y = v + 0.0204356 \times e^{0.5(\frac{x-M_0}{50.0525})^2} \tag{10.8}$$

10.4 Statistical Procedure

Our general strategy for this analysis is to use toy MC to predict the likely distribution of background events and signal events for varying mass values of possible Z' bosons, as well as for different possible cross-sections. In order to do this, we adopted a unified test statistic that could be used to measure the power of both parts of the analysis.

10.4.1 Test Statistic

In order to allow the addition of results from the two channels, we used the same test statistic for both halves of the analysis. To take advantage of techniques previously presented, we select a test statistic very similar to that used in the

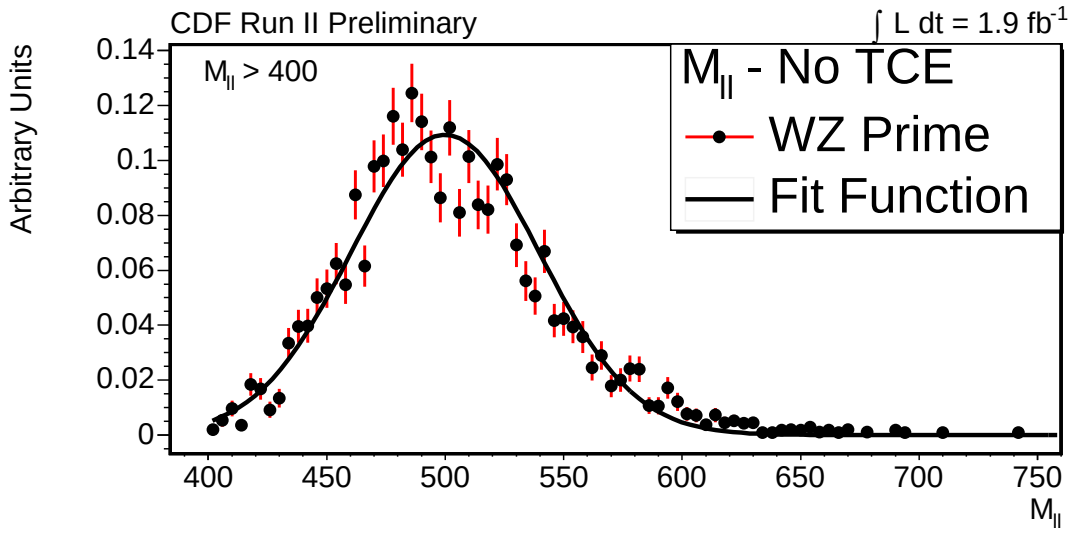

Figure 10.4: μ dilepton mass distribution in signal

aTGC analysis, although with a minor fitting element. The test statistic is defined as

$$S(sf) = \prod_N \frac{sf \times P_s + (1-sf) \times P_b}{P_b}$$

where:

$$P = P_{ll} \times P_{jj} \text{ for signal and background in } WZ' \to lljj$$
$$P = P_{ll} \text{ for signal and background in } WZ' \to lll\nu$$

if the number of events, N_{data} is greater then 0. The value is set to 0 if S = 0.

The Signal Fraction (sf) is then left as a variable. To determine the optimal sf value, and the optimal mix of signal and background to make the shape observed in data, we measure the test statistic at every value of sf:

$$sf = \frac{x}{N_{data}}$$

where x is incremented from 0 to N_{data}. The final value S chosen is the highest for all the given range of sf.

$$S_{final} = Max(S(\frac{x}{N_{data}}), x = 1, 2, ...N_{data})$$

and P_{ll} and P_{jj} are the probabilities for the dilepton and dijet mass distributions respectively, while N is the number of events.

10.4.2 Creating Background Toy MC

Background toy MC is based upon the templates extracted from MC as described above. For each experiment we create background events by randomly selecting a dilepton mass (for trilepton events) or a dilepton mass and a dijet mass (for the dilepton dijet analysis), and then computing the value of the test statistic for each dilepton mass in a set range.

The expected yields for background are taken from the standard CDF MC for those particular sources, and varied according to Poisson statistics. Each event is then generated randomly from the proper distribution. For each simulated event, the test statistic is calculated and stored for each bin in dilepton mass.

At the end of toy MC event generation, the vectors holding the quantity of test statistics are sorted, and the values corresponding to 3 and 5 σ probabilities are extracted. These are the test statistics for which only 0.01% and 5.733e-05% of events will have a higher test statistic value, denoted $B3$ and $B5$ respectively. Any dataset that returns a test statistic value higher then $B3$ constitutes a 3 σ violation of the Standard Model, and any dataset returning a test statistic higher then $B5$ is violating that Standard Model at a 5 σ level.

There exists, for every dilepton mass considered, a value of $B3$ and $B5$, denoted $B3_{ll}$ and $B5_{ll}$.

10.4.3 Creating Signal MC

Signal toy MC is based on the templates described previously, and is generated according to yields that would give one event in the first 1 fb^{-1}, as measured in the preliminary potential event. Fully simulated and reconstructed MC are used to determine the shape and features of the signal templates. Expected yields are then Poisson varied, and events are randomly selected from the templates. The

only difference between this and the background MC is that the signal dilepton mass template has a variable central mass.

For each toy experiment, we calculate the test statistic S for each value of dilepton mass, producing an array of values S_{ll}. For each value S_{ll}, you can discover whether or not you have a 3 sigma violation of the SM by comparing it to the value of $B3_{ll}$, and a 5 sigma by comparing it to the corresponding value of $B5_{ll}$.

In order to present a result, we need to not only pick an S for a given dataset, but also to pick a value of M_{ll} is corresponds to, as we wish to report both a discovery and a mass in the case of a Standard Model violation. This means we have to pick one of the ll values for S_{ll}. We do this by comparing the highest T value, where T is defined as:

$$T = Max(S_{ll} - B5_{ll}, forallll)$$

We then report the test statistic, the level of violation of the Standard Model that it entails, and the mass for which T was maximum.

At the end of a run of experiments, we can compare the test statistic values for each experiment to the background cutoff and create a probability for us to observe a 3 or 5 σ deviation from background with the signal model as specified.

10.4.4 Fit Results

Results were first calculated for the $WZ' \to \ell\ell jj$ as a means to test the ability of the tools. The plots that are presented here are an expression of the total probability for making a 3 or 5 σ measurement at the given value of dilepton mass. The histograms record the total number of times when the T value was above either the 3 or 5 σ level, divided by the total number of events in the sample. Each bin in the histogram thus represents the percentage chance of recording a violation at either the 3 or 5 σ level of the Standard Model at that dilepton mass. The integral of the histogram represents the total probability of recording either a 3 or 5 σ violation of the Standard Model, and making the subsequent discovery.

Part of this chapter is being considered for potential publication by the CDF Collaboration.

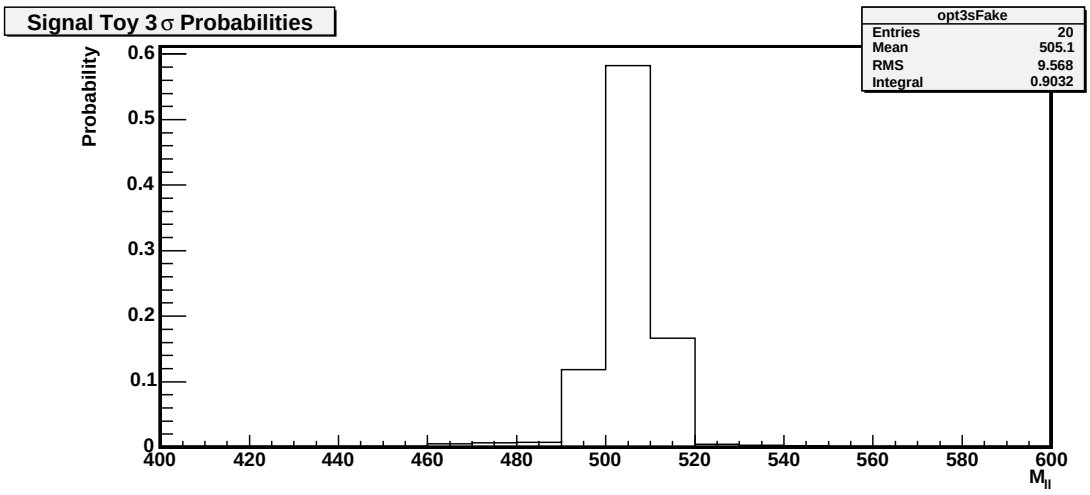

Figure 10.5: Probability of reconstructing a 500 GeV Z' signal in $WZ' \rightarrow \ell\ell jj$ with greater then a 3 σ difference from background

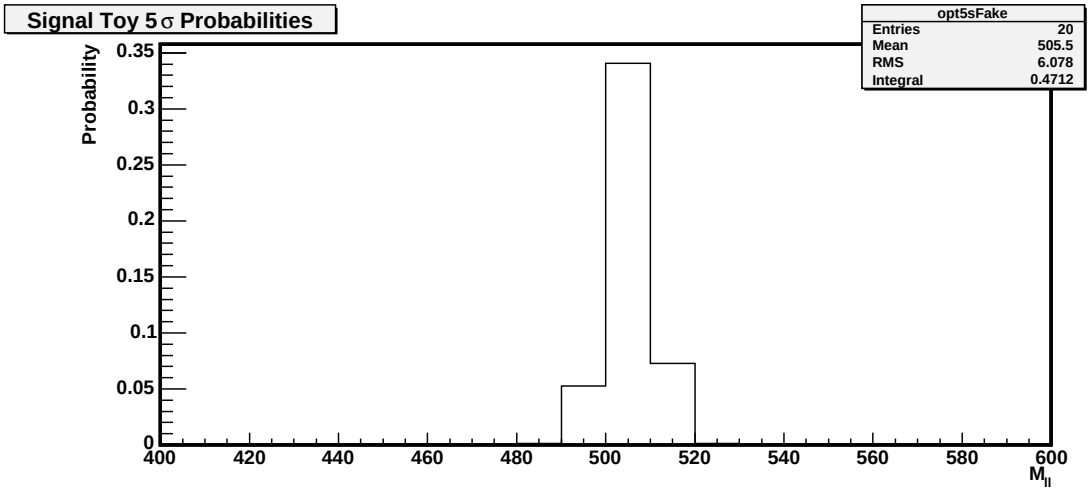

Figure 10.6: Probability of reconstructing a 500 GeV Z' signal in $WZ' \rightarrow \ell\ell jj$ with greater then a 5 σ difference from background

Bibliography

[1] The cdf ii detector technical design report. pages 1 – 15–6, 1996.

[2] *et al.* Aaltonen, T. First measurement of zz production in ppbar collisions at sqrt(s) = 1.96 tev. *Physical Review Letters*, 100:201801, 2008.

[3] *et al.* Aaltonen, T. A search for high-mass resonances decaying to dimuons at cdf. *Submitted to Physical Review Letters*, 2008.

[4] et. al. Abazov, V.M. *Phys. Rev.*, D76, 2007.

[5] et. al. Abazov, V.M. *Phys. Rev. Lett.*, 100, 2008.

[6] F. Abe, *et al. Physical Review*, D 45:1448, 1992.

[7] *et al.* Abulencia, A. Observation of wz production. *Physical Review Letters*, 98:161801, 2007.

[8] T. Affolder *et al. Nucl. Instrum. Methods A*, 526:249, 2004.

[9] et. al. Alwall, J. *Comput.Phys.Commun.*, 176:300–304, 2007.

[10] C. Amsler, *et al.* Review of particle physics. *Phys. Lett. B*, 667:1, 2008.

[11] L. Balka, *et al. Nucl. Instrum. Methods*, A267:301, 1988.

[12] U. Baur and D. Rainwater. *Phys. Rev.*, D62:113011, 2000.

[13] U. Baur and D. Rainwater. *Int. J. Mod. Phys*, A16S1A:315–317, 2001.

[14] et. al. Bhatti, A. *Nucl.Instrum.Meth.*, A566:375–412, 2006.

[15] A. Bridgeman and T. Liss. Reducing the jet energy scale uncertainty in the ttbar differential cross section analysis, 2008. CDF/PHYS/TOP/CDFR/9398.

[16] J. M. Campbell and R. K. Ellis. *Physical Review*, D 60:113006, 1999.

[17] Sebastian Carron, Doug Benjamin, Mircea Coca, and Mark Kruse. An inclusive dilepton analysis (aida) using 360 /pb of cdf run ii data, 2006. CDF/PUB/TOP/PUBLIC/8146.

[18] CDF Collaboration. Update to proposal p-909: Funding for an inner silicon layer and a time of flight detector for the cdf ii detector. 1999.

[19] The LEP Collaborations. A combination of preliminary electroweak measurements and constraints on the standard model. 2007.

[20] R. Fletcher. A new approach to variable metric algorithms. *The Computer Journal*, 13:317–322, 1970.

[21] *et al.* Frisch, H. Conceptual design of a deadtimeless trigger for the cdf upgrade, 1993. CDF/DOC/TRIGGER/CDFR/2038.

[22] Kenichi Hatakeyama, Anwar Bhatti, and Robert Harris. Search for new particles decaying into dijets in p-pbar collisions at sqrts=1.96 tev, 2008. CDF/PUB/EXOTIC/PUBLIC/9246.

[23] Matt Herndon. Cdf tracking experience, 2004.

[24] *et al.* Hsu, S.C. Measurement of triple gauge couplings in wz to trilepton plus met using 1.9fb-1, 2007. CDF/ANAL/ELECTROWEAK/CDFR/8759.

[25] F. James. Minuit - function minimization and error analysis. 1998.

[26] Byeong Rok Ko, Seog H. Oh, and Wang Chiho. High-mass dielectron resonance search in ppbar collisions at sqrt(s)=1.96 tev, 2008. CDF/PUB/EXOTIC/PUBLIC/9160.

[27] J. A. Nelder and R. Mead. A simplex method for function minimization. *The Computer Journal*, 7:308–313, 1965.

[28] A. Sfyrla. Search for ww and wz production in lepton, neutrino plus jets final states at cdf run ii, 2008. CDF/PUB/ELECTROWEAK/PUBLIC/9216.

[29] A. Sill *et al. Nucl. Instrum. Methods A*, 447:1, 2000.

[30] Torbjorn Sjostrand. Pythia 5.7 and jetset 7.4 physics and manual, 1995.

[31] Torbjorn Sjostrand, Stephen Mrenna, and Peter Skands. Pythia 6.4 physics and manual. *J. High Energy Phys.*, 47:4889–4904, 1993.